UNIVERSITY OF CALIFORNIA
RIVERSIDE

Poroelastic Effects on the Interpretation of Diagnostic Fracture Injection Tests

A Dissertation submitted in partial satisfaction
of the requirements for the degree of

Doctor of Philosophy

in

Mechanical Engineering

by

Jun Du

June 2024

Dissertation Committee:
Dr. Guanshui Xu, Chairperson
Dr. Kambiz Vafai
Dr. Hideaki Tsutsui

The Dissertation of Jun Du is approved:

_____

_____

_____

Committee Chairperson

University of California, Riverside

Acknowledgment

First, I would like to express my profound appreciation to my advisor, Professor Guanshui Xu, for his continuous guidance and support throughout my Ph.D. studies. He is always available whenever I have difficulties with my research. Without his insightful discussions and clarifications, this work would not have been possible. It was a great pleasure to have him as my advisor.

I would also like to thank Professor Kambiz Vafai and Professor Hideaki Tsutsui for reviewing my dissertation and serving as members of my dissertation committee.

Furthermore, I am grateful to my team members, Boshen Li and Tianxiang Huang, for their helpful discussions and contributions.

Finally, I want to thank my family for their endless love and support.

ABSTRACT OF THE DISSERTATION

Poroelastic Effects on the Interpretation of Diagnostic Fracture Injection Tests

by

Jun Du

Doctor of Philosophy, Graduate Program in Mechanical Engineering
University of California, Riverside, June 2024
Dr. Guanshui Xu, Chairperson

Diagnostic Fracture Injection Tests (DFIT) are techniques that have been widely used in hydraulic fracturing to estimate reservoir properties and parameters. A fully coupled poroelastic model is developed to simulate hydraulic fracture initiation, propagation, and closure using the finite element method. The pressure decline data after shut-in is analyzed to estimate the leak-off coefficient, in-situ stress, permeability, and pore pressure. Results are compared to previous DFIT techniques developed based on linear elastic fracture mechanics and Carter's leak-off model.

During the before-closure analysis, the pressure decline data is analyzed to estimate the leak-off coefficient and in-situ stress through a special dimensionless time function called G-function. With poroelastic effects taken into account, the leak-off coefficient can be

twice as large as the one obtained from previous DFIT techniques. Also, higher in-situ stress estimates are obtained in the fully coupled model. The after-closure analysis involves the identification of linear flow and radial flow regimes. The linear flow analysis can significantly overestimate reservoir permeability, while the radial flow analysis can obtain a reliable permeability estimate. Both the linear and radial flow analyses can provide accurate estimates of pore pressure.

This study demonstrates that poroelastic effects cannot be ignored in some cases. The previous DFIT techniques developed based on linear elastic fracture mechanics and Carter's leak-off model may result in inaccurate estimation of properties such as leak-off coefficient and permeability, further affecting the optimization of hydraulic fracturing treatment design.

Contents

List of Figures

List of Tables

Chapter 1

Introduction

1.1 Hydraulic fracturing

Hydraulic fracturing is a stimulation technology that has been commonly used in the oil industry to improve the well productivity from formations with lower permeability. This technology has been exploited by the oil and gas industry to enhance hydrocarbon production since the 1950s. By pumping a mixture of fluid and sand into a reservoir of low permeability, it is possible to generate a network of fractures that connect the wellbore with the large volume of the reservoir. The proppant is used to prop the fractures after the fracturing fluid is leaked into the reservoir. The propped fractures serve as effective fluid channels and therefore can considerably enhance hydrocarbon production.

Due to the difficulty of direct monitoring real fracture geometries, fracture modeling and simulation play an important role in hydraulic fracturing treatment design. At the earlier stage of development, three basic classical models, PKN model (Perkins and Kern, 1961), KGD model (Geertsma and de Klerk, 1969), and the penny-shaped or radial model

(Savitski and Detournay, 2002), were proposed for the analysis of the hydraulic fracturing process. These models assume that the reservoir is linear elastic solid, and the fluid flow between fracture surfaces follows Reynold's equation. As shown in Figure 1.1, these models vary by simplifying certain fracture configurations.

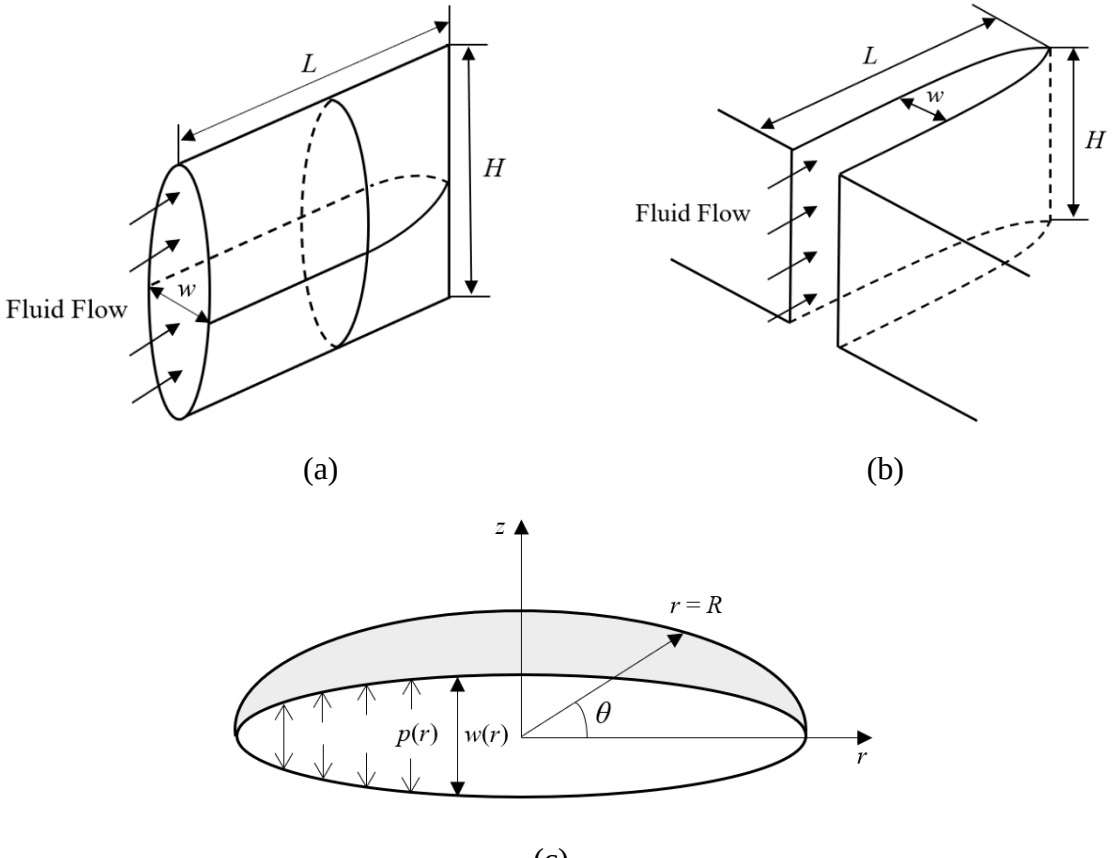

Figure 1.1: Fracture geometries (Li, 2023): (a) PKN model; (b) KGD model; (c) Penny-shaped model

The KGD model assumes that the fracture height is constant and the fracture is at plane strain condition in the horizontal plane. Besides the constant height assumption, the PKN model also assumes that the fracture is at plane strain condition in the vertical plane and the fracture toughness is negligible. The KGD model is suitable for fractures whose height

is much larger than its length, while the PKN model is suitable for fractures whose length is much larger than its height. The KGD model and the PKN model were the first two models that took both volume balance and solid mechanics into consideration (Economides, 2000). The penny-shaped model assumes that the fluid is injected from a point source. The shape of the fracture is expected to be circular when the minimum in-situ stress is distributed uniformly.

Although a variety of models have been proposed to investigate hydraulic fracturing, most of them were established by using Carter's one-dimensional model to represent leak-off. The fluid flow from the fracture into the formation is over simplified. The fluid loss into the reservoir will cause an expansion of the reservoir and an increase in fluid pressure, which further induces the effective change in the rock matrix. The back stresses resulting from the dilated reservoir will tend to oppose fracture opening (Salimzadeh, 2016). Therefore, a fully coupled model taking poroelastic effects into consideration is required to predict fracture geometries and fluid pressure more realistically.

1.2 Diagnostic fracture injection tests

One technique that can be improved by the fully coupled model is Diagnostic Fracture Injection Tests (DFIT), which have been widely used to estimate reservoir properties and parameters, such as leak-off coefficient, in-situ stress, permeability, and pore pressure. The DFIT procedure involves pumping a small volume of fluid into a reservoir at a constant rate for a short time to create a fracture then the well is shut-in, and the pressure falloff is recorded and analyzed. However, existing DFIT techniques are developed based on linear

elastic fracture mechanics (LEFM) and Carter's oversimplified leak-off model, which can result in an incorrect estimation of reservoir parameters.

Pressure interpretation prior to fracture closure is known as before-closure analysis (BCA), which was pioneered by Nolte's work (1979 and 1986) with the development of G-function. Assuming that the fracture surface growth follows the power law, Nolte noted that pressure decreases linearly with the dimensionless G-function before the fracture closes. Analytical techniques were also provided to estimate the fluid loss coefficient, fluid efficiency, and time for the fracture to close.

Barree and Mukherjee (1996) and Barree et al. (2009) proposed a method to identify closure pressure qualitatively using G-function and its derivatives. The closure is identified by the deviation of the semi-log derivative of pressure (Gdp/dG) versus the G-function from the straight line. This method is referred to as the tangent line method and has become the standard practice for DFIT analysis.

Mayerhofer (1993 and 1995) introduced an alternative model to interpret the leak-off process instead of using Cater's leak-off model. In this method, pressure response is considered from the fracture into the formation. By representing the pressure falloff data in a specialized plot, which is referred to as the Mayerhofer plot, the filter cake resistance and reservoir permeability can be estimated from the intercept and slope of the straight line in the Mayerhofer plot.

McClure et al. (2016) presented the compliance method to estimate fracture closure pressure, which is picked up at the point where the system stiffness starts to increase. The

compliance method results in an earlier and higher closure pressure estimate than the tangent line method.

Wang and Sharma (2017) proposed the variable compliance method to estimate minimum in-situ stress by averaging the G-time of the tangent line method and compliance method. The variable compliance method leads to a more accurate estimation of minimum in-situ stress without the consideration of poroelastic effects.

Zanganeh (2017) reinterpreted the facture closure dynamics using the cohesive zone model for fracture initiation, propagation, and closure. A leak-off model that is pressure-dependent and related to formation properties is used for simulation. The closure pressure is picked up at the start of the tip closure, which is consistent with the compliance method proposed by McClure.

Pressure interpretation after fracture closure is known as after-closure analysis (ACA), which involves the identification of linear flow and radial flow. The boundary condition along the fracture changes from constant pressure to zero flux after the fracture closure. Nolte et al. (1997) presented the formula for pressure difference during the linear flow period based on the heat transfer analysis (Carslaw and Jaegar, 1959). Reservoir parameters such as fracture length and closure time can be estimated during the linear flow analysis. The radial flow analysis was developed by Gu et al. (1993), which is known as the “impulse fracture test”. Permeability and initial pore pressure can be obtained if a radial flow exists.

1.3 Dissertation outline

The primary objective of this research is to investigate the poroelastic effects on the interpretation of DFIT for both the KGD model and the penny-shaped model.

Chapter 1 provides an introduction to hydraulic fracturing and a literature review of current DFIT techniques. Chapter 2 presents the governing equations to model hydraulic fracturing, the fracture propagation criterion, and the relevant theory about BCA and ACA. Chapter 3 presents the finite element formulation for each governing equation and the validation of the current model against several analytical solutions. Chapter 4 starts with a leak-off comparison of different models. Then, the poroelastic effects on both BCA and ACA for the KGD model are studied using six sets of parameters. Chapter 5 provides the poroelastic effects on BCA for the penny-shaped model and the conclusion of this research.

Chapter 2

Mathematical model of hydraulic fracturing

2.1 Problem statement

Fracture models have been well developed over the past few decades based on the following three relations: linear elastic fracture mechanics (LEFM), fluid flow in the fracture, and continuity equation. Instead of using Carter's leak-off model to represent fluid flowing from the fracture into the formation, the formation can be modeled as porous medium based on the theory of poroelasticity, which was developed initially by Terzaghi for a one-dimensional problem. The term *poroelasticity* was first proposed by Geertsma in his 1966 paper (Wang, 2000). Biot extended the theory to the three dimensions later.

Figure 2.1 shows the schematic illustration of a fluid-driven fracture in the porous medium, which includes multiple physical processes: (i) fluid flow within the fracture, (ii) fluid flow in the porous medium, (iii) deformation of the porous medium, (iv) fluid leaking into the porous medium via the fracture surface, and (v) hydraulic fracture initiation, propagation, and closure.

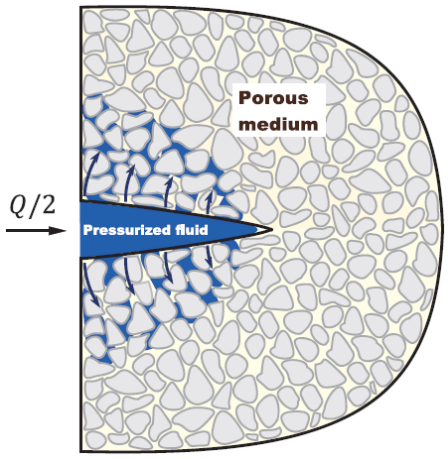

Figure 2.1: Schematic illustration of a fluid-driven fracture in the porous medium (Monhammadnejad, 2016)

Figure 2.2 shows the sketch of a hydraulic fracture in the porous medium with domain Ω and boundary Γ. The fracture is considered a discontinuity with two surfaces through which the fluid flow inside the fracture is leaked into the formation. The differential displacement between the two surfaces is the fracture width. The deformation of the porous medium is coupled with the fracture flow through the fluid pressure applied to the fracture surfaces.

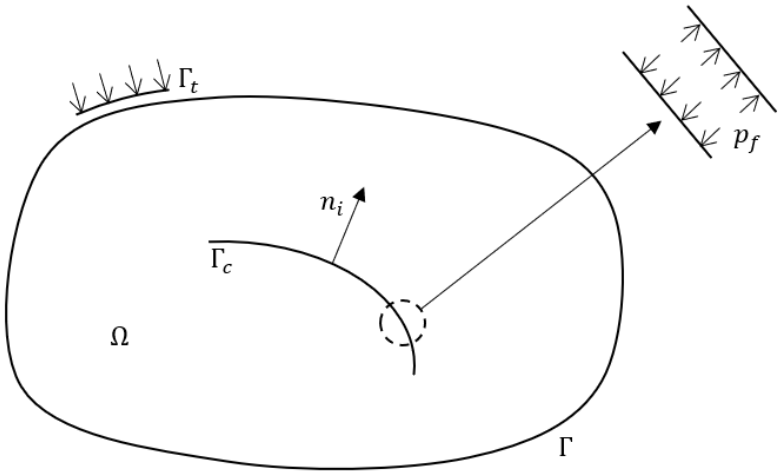

Figure 2.2: Sketch of a fracture with domain Ω and boundary Γ

2.2 Deformation of porous medium

The porous medium is assumed to be fully saturated with a compressible fluid. Under the quasi-static conditions, the equilibrium equation of a representative elementary volume takes the form

$$\frac{\partial \sigma_{ij}}{\partial x_j} + b_i = 0 \tag{2.1}$$

where b_i is the body force and σ_{ij} is the total stress which can be written as (Biot, 1941)

$$\sigma_{ij} = \sigma'_{ij} - \alpha p \delta_{ij} \tag{2.2}$$

where σ'_{ij} is the effective stress, p is the fluid pressure in the porous medium, δ_{ij} is the Kronecker delta, which is defined as $\delta_{ij} = 1$ for $i = j$ and $\delta_{ij} = 0$ for $i \neq j$, α is the Biot coefficient, which is given by

$$\alpha = 1 - \frac{K}{K_s} \tag{2.3}$$

where K is the drained bulk modulus and K_s is the solid bulk modulus. The Biot coefficient indicates the degree of coupling between deformation and fluid flow in the porous medium. The relationship between total stress and strain can be expressed as

$$\sigma_{ij} = \left(K - \frac{2G}{3}\right)\epsilon \delta_{ij} + 2G\epsilon_{ij} - \alpha p \delta_{ij} \tag{2.4}$$

where G is the shear modulus, ϵ is the volumetric strain which is equal to ϵ_{kk}, ϵ_{ij} is the strain, which can be expressed as

$$\epsilon_{ij} = \frac{1}{2}\left(\frac{\partial u_i}{\partial x_j} + \frac{\partial u_j}{\partial x_i}\right) \tag{2.5}$$

where u_i is the displacement. Substituting equation (2.4) and (2.5) into equation (2.1), the equilibrium equation in terms of displacements and pressure becomes

$$\left(K+\frac{G}{3}\right)\frac{\partial^2 u_j}{\partial x_i \partial x_j}+G\frac{\partial^2 u_i}{\partial x_j \partial x_j}-\alpha\frac{\partial p}{\partial x_i}=0 \tag{2.6}$$

2.3 Fluid flow in the porous medium

By combining the mass balance equation and Darcy's law, the fluid flow in the porous medium can be expressed as (Verruijt, 2016)

$$\alpha\frac{\partial}{\partial t}\left(\frac{\partial u_j}{\partial x_j}\right)+S\frac{\partial p}{\partial t}=\frac{k}{\mu}\left(\frac{\partial^2 p}{\partial x_j \partial x_j}\right) \tag{2.7}$$

where k is the permeability, μ is the viscosity, S is the specific storage coefficient, which is given by

$$S=\frac{\phi}{K_f}+\frac{\alpha-\phi}{K_s} \tag{2.8}$$

where K_f is the fluid bulk modulus, and ϕ is the porosity. Equation (2.7) is denoted as the storage equation and is often written as (Wang, 2000)

$$\frac{\partial \zeta}{\partial t}=\frac{k}{\mu}\left(\frac{\partial^2 p}{\partial x_j \partial x_j}\right) \tag{2.9}$$

where $\partial\zeta/\partial t$ is the change in fluid content. For the stiff materials, the first term in equation (2.7) can be ignored since the second term may dominate the first one. In this condition, equation (2.7) can reduce to

$$S\frac{\partial p}{\partial t}=\frac{k}{\mu}\left(\frac{\partial^2 p}{\partial x_j \partial x_j}\right) \tag{2.10}$$

This decoupled form plays a vital role in reservoir engineering (Verruijt, 2016; Dake, 1978).

2.4 Fluid flow in the fracture

Figure 2.3 shows the sketch of a three-dimensional hydraulic fracture. The fracture width w in the x_3 direction is measured in millimeters and is significantly less than the fracture length or fracture radius, which can be tens to hundreds of meters in the x_1 and x_2 direction. The lubrication theory derived from the Navier-Stokes equation can govern the fluid flow in such a geometry in which the dimension in one direction is much smaller than the dimension in the other two directions. The lubrication theory was developed based on the assumption of negligible body force, Newtonian laminar flow, no-slip condition, and constant pressure and velocity in the x_3 direction.

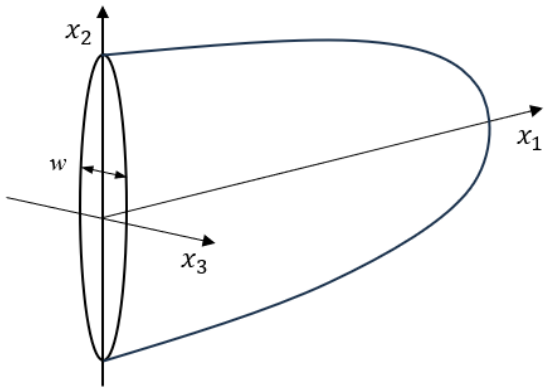

Figure 2.3: Sketch of a 3D hydraulic fracture

Using the cubic law derived from the lubrication theory, the volumetric flow rate inside the fracture can be expressed as (Batchelor, 1967)

$$q_\beta = -\frac{w^3}{12\mu}\frac{\partial p_f}{\partial x_\beta} \tag{2.11}$$

where the subscript β denotes the fracture propagation direction and can be 1 and 2, the fracture width w is given by $(u_i^+ - u_i^-)\, n_i$. In the latter expression, n_i is the unit vector normal to the fracture surface. Then the mass balance equation for the fracture flow can be written as

$$\frac{\partial}{\partial x_\beta}\left(\frac{w^3}{12\mu}\frac{\partial p_f}{\partial x_\beta}\right) = \frac{\partial w}{\partial t} + q_L \tag{2.12}$$

where q_L represents the leak-off flow from the fracture into the formation. By using Darcy's law, q_L takes the form

$$q_L = \frac{k}{\mu}\frac{\partial p}{\partial x_i} n_i \tag{2.13}$$

Equation (2.12) governs the fluid flow within the fracture. For the KGD model, the subscript β in equation (2.12) can be omitted for simplicity. The boundary conditions for the fluid flow are

$$q(0,t) = Q_0/2 \tag{2.14a}$$

$$q(x = l_t, t) = 0 \tag{2.14b}$$

$$w(x = l_t, t) = 0 \tag{2.14c}$$

where l_t is fracture half-length at time t. Both the flow rate and the width at the fracture tip are zero.

In contrast to Darcy's law, Carter's leak-off model can be derived from the solution of a one-dimensional diffusion equation with the assumption of constant pressure drop between

the fracture surface and boundary. According to Carter's leak-off model, q_L is given by (Howard and Fast, 1957)

$$q_L = \frac{2C_L}{\sqrt{t - \tau(x)}} \tag{2.15}$$

where C_L is Carter's leak-off coefficient, τ is the time at which the fluid reaches the location x. The coefficient 2 accounts for the leak-off over the two fracture surfaces.

2.5 Fracture propagation

The stress intensity factors (SIFs) can be calculated to indicate the stress concentration around the fracture tip. The approaches used to calculate SIFs can be divided into two categories: energy methods and direct methods (Nejati, 2015). In energy methods such as J-integral (Rice, 1968), the energy release rate is calculated first and then converted to SIFs using the relationship between them. On the other hand, in the direct methods, stresses or displacements near the crack are calculated to obtain the SIFs. Figure 2.4 shows the coordinate axis with the origin at the crack tip, r is the distance from the crack tip, and θ is the polar angle.

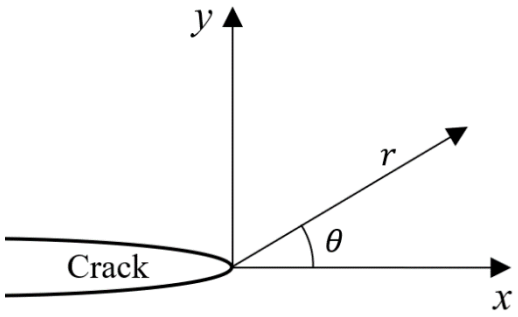

Figure 2.4: Coordinate axis with the origin at the crack tip

The stress field near the tip can be expressed as (Anderson, 2005)

$$\sigma_{ij} = \left(\frac{d}{\sqrt{r}}\right) f_{ij}(\theta) + \sum_{m=0}^{\infty} A_m r^{m/2} g_{ij}^{(m)}(\theta) \tag{2.16}$$

where d is the constant, f_{ij} is a dimensionless function of θ in the leading term, A_m is the amplitude, and $g_{ij}^{(m)}$ is a dimensionless function of θ for the mth term. While the distance r approaches zero, the leading term approaches infinity.

As shown in Figure 2.5, opening (mode I), in-plane shear (mode II), and out-of-plane shear (mode III) are the three types of loading that can be applied to a crack.

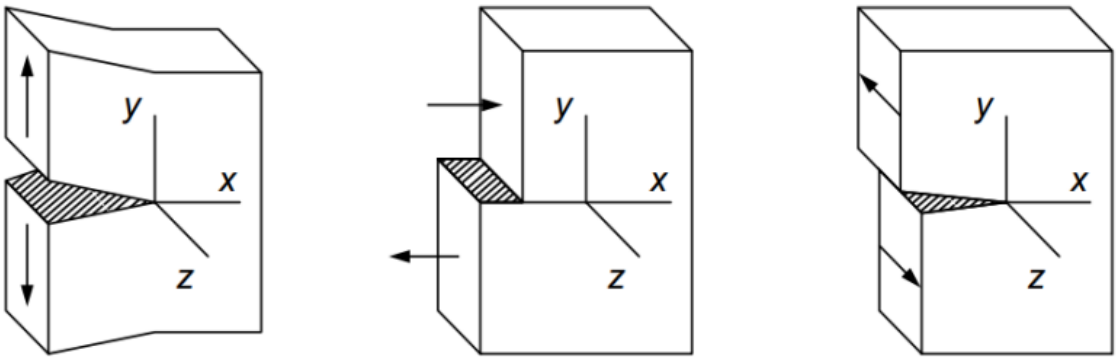

(a) (b) (c)

Figure 2.5: Three types of loading that can be applied to a crack (Sun, 2012): (a) Mode I; (b) Mode II; (c) Mode III

Fracture propagation is mode I dominated and the stress fields adjacent to the crack tip for mode I are given by

$$\sigma_{xx} = \frac{K_I}{\sqrt{2\pi r}} \cos\left(\frac{\theta}{2}\right)\left[1 - \sin\left(\frac{\theta}{2}\right)\sin\left(\frac{3\theta}{2}\right)\right] \tag{2.17a}$$

$$\sigma_{yy} = \frac{K_I}{\sqrt{2\pi r}} \cos\left(\frac{\theta}{2}\right)\left[1 + \sin\left(\frac{\theta}{2}\right)\sin\left(\frac{3\theta}{2}\right)\right] \tag{2.17b}$$

$$\tau_{xy} = \frac{K_I}{\sqrt{2\pi r}} \cos\left(\frac{\theta}{2}\right)\sin\left(\frac{\theta}{2}\right)\cos\left(\frac{3\theta}{2}\right) \tag{2.17c}$$

where K_I is mode I stress intensity factor. The corresponding displacement fields for mode I are given by

$$u_x = \frac{K_I}{2G}\sqrt{\frac{r}{2\pi}} \cos\left(\frac{\theta}{2}\right)\left[\kappa - 1 + 2\sin^2\left(\frac{\theta}{2}\right)\right] \tag{2.18a}$$

$$u_y = \frac{K_I}{2G}\sqrt{\frac{r}{2\pi}} \sin\left(\frac{\theta}{2}\right)\left[\kappa + 1 - 2\cos^2\left(\frac{\theta}{2}\right)\right] \tag{2.18b}$$

where, κ is the Kolosov constant, which is equal to $3 - 4v$ for the plane strain condition. When $\theta = \pi$,

$$K_I = \lim_{r\to 0}\left[\sqrt{\frac{2\pi}{r}}\frac{Gu_y}{2(1-v)}\right] \tag{2.19}$$

The fracture propagation criterion is

$$K_I = K_{IC} \tag{2.20}$$

where K_{IC} is the material toughness of the solid matrix.

2.6 Before-closure analysis (BCA)

During the before-closure analysis, the leak-off coefficient and in-situ stress can be inferred through a special dimensionless time function called G-function developed by Nolte. With

the assumption of Carter's leak-off model, power law fracture evolution, constant fracture pressure on the boundary, and constant fracture surface after shut-in, the pressure decline after shut-in can be expressed as (Economides, 2000)

$$p_f(\Delta t_D) = ISIP - \frac{\pi r_p C_L S_f \sqrt{t_e}}{2} G(\Delta t_D) \tag{2.21}$$

where Δt_D is dimensionless time, which is defined as

$$\Delta t_D = \frac{t - t_e}{t_e} \tag{2.22}$$

where t is the generic time, t_e is the time at shut-in. $ISIP$ is instantaneous shut-in pressure, r_p is the ratio of fracture of area that is subject to leak-off to the total surface area, which is assumed to be one for simplicity, and S_f is fracture stiffness. S_f and C_L can be calculated by using Table 2.1 and Table 2.2 (Valko and Economides, 1999), respectively. The derivation of equation (2.21) is presented in Appendix A.

In Table 2.1 and Table 2.2, h_f, x_f, and R_f are fracture height, fracture half-length, and facture radius, respectively, m_N is the slope of the straight line, E' is the plane strain modulus, which is defined as

$$E' = \frac{E}{1 - v^2} \tag{2.23}$$

where E is the Young's modulus and v is the Poisson's ratio.

Table 2.1: Proportionality constant S_f for different fracture geometries

PKN	KGD	Radial
$\frac{2E'}{\pi h_f}$	$\frac{E'}{\pi x_f}$	$\frac{3\pi E'}{16R_f}$

Table 2.2: Leak-off coefficient C_L for different fracture geometries

PKN	KGD	Radial
$\frac{\pi h_f}{4r_p\sqrt{t_e}E'}(-m_N)$	$\frac{\pi x_f}{2r_p\sqrt{t_e}E'}(-m_N)$	$\frac{8R_f}{3\pi r_p\sqrt{t_e}E'}(-m_N)$

The G-function is defined as

$$G(\Delta t_D) = \frac{4}{\pi}[g(\Delta t_D) - g(0)] \tag{2.24}$$

where g-function is given by

$$g(\Delta t_D) = \begin{cases} (1+\Delta t_D)\sin^{-1}(1+\Delta t_D)^{-1/2} + \Delta t_D^{1/2} & \text{for low fluid efficiency} \\ \frac{4}{3}\left[(1+\Delta t_D)^{3/2} - \Delta t_D^{3/2}\right] & \text{for high fluid efficiency} \end{cases} \tag{2.25}$$

The fluid efficiency is defined as

$$\eta = \frac{V_f}{V_i} \tag{2.26}$$

where V_i is the total injected volume, V_f is the fracture volume at the end of the injection. Without the consideration of spurt, the fluid efficiency can also be estimated using the following formula

$$\eta \approx \frac{G_c}{2+G_c} \tag{2.27}$$

where G_c is the value of $G(\Delta t_D)$ at closure. The analytical solution for Carter's leak-off coefficient can be expressed as (Howard and Fast, 1957)

$$C_L = (p_f - p_i)\sqrt{\frac{k\phi c_t}{\pi\mu}} \tag{2.28}$$

where p_i is the initial reservoir pressure, c_t is the total compressibility, which is defined as

$$c_t = c_s + c_f \tag{2.29}$$

where c_s is the solid compressibility, which is equal to $1/K_s$ and c_f is the fluid compressibility, which is equal to $1/K_f$. Yarushina (2013) presented another expression of total compressibility, which takes the form below

$$c_t = \frac{\phi c_\phi}{1-\phi} + \frac{\phi^2 c_s}{1-\phi} + \phi c_f = \phi\tilde{c} \tag{2.30}$$

where c_ϕ is the pore space compressibility, which is often considered identical to c_s in the literature. The $\tilde{c}$ in equation (2.30) is equivalent to c_t in equation (2.29) when porosity is relatively small.

2.7 After-closure analysis (ACA)

The after-closure analysis involves the identification of linear and radial flow regimes. As shown in Figure 2.6a, the parallel flow in the formation indicates the existence of the linear flow. In Figure 2.6b, the flow converging to the line located at the center of the wellbore indicates the existence of the radial flow. During the DFIT analysis, the linear flow and the radial flow can be identified based on the slope of the pressure derivative curve.

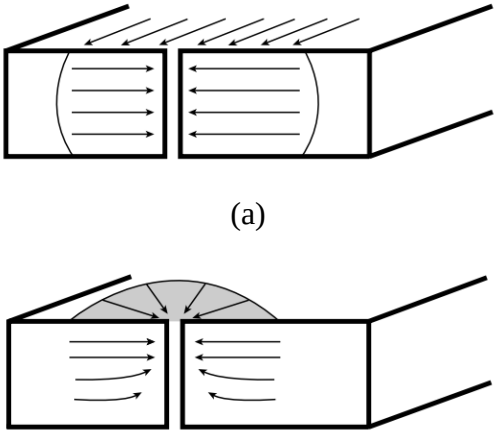

(a)

(b)

Figure 2.6: Linear flow and radial flow (Economides, 2000): (a) Linear flow to fracture; (b) Complete radial flow

2.7.1 Linear flow period

After the fracture closure, the boundary condition changes from a constant pressure condition to a zero flux condition, which is referred to as the mixed boundary condition or changed boundary condition (Nolte et al., 1997). Carslaw and Jaegar (1959) provided a closed form solution for this kind of mixed boundary condition in the heat transfer analysis. The pressure difference during the linear flow period can be expressed as (Talley et al., 1999)

$$p(t) - p_i = m_L F_L(t, t_c) \tag{2.31}$$

where m_L is the slope, which is written as

$$m_L = C_L \sqrt{\frac{\pi\mu}{k\phi c_t}} \tag{2.32}$$

The linear flow time function is defined as

$$F_L(t, t_c) = \frac{2}{\pi} \sin^{-1} \sqrt{\frac{t_c}{t}}, \quad t \geq t_c \tag{2.33}$$

where t_c is the time to fracture closure. When t is significantly larger than t_c, F_L can be approximated as

$$F_L(t, t_c) = \frac{2}{\pi} \sqrt{\frac{t_c}{t}}, \quad t \gg t_c \tag{2.34}$$

Therefore, pressure versus linear flow time is equivalent to pressure versus reciprocal square root of time, and pressure versus square of linear flow time is equivalent to pressure versus reciprocal time under these conditions (McClure, 2019).

2.7.2 Radial flow period

There is no relation similar to equation (2.31) that has been proposed for a fracture with a mixed boundary condition during the radial flow period. Gu et al. (1993) presented an after-closure analysis based on the instantaneous line source solution to the diffusivity equation. The pressure difference during the radial flow period can be expressed as (Talley et al., 1999)

$$p(t) - p_i = m_R F_R(t, t_c) \tag{2.35}$$

The radial flow time function is defined as

$$F_R(t, t_c) = \frac{1}{4} \ln\left(1 + \frac{\chi t_c}{t - t_c}\right) \tag{2.36}$$

where χ is defined as

$$\chi = \frac{16}{\pi^2} \approx 1.6 \tag{2.37}$$

For well-developed radial flow, χ is equal to unity. The permeability can be estimated by using the following equation

$$\frac{kh}{\mu} = 251{,}000\frac{Q}{m_R t_c} \tag{2.38}$$

where permeability k is in md, net pay thickness h is in feet, viscosity μ is in cp, t_c is in minutes, the injected volume is Q in bbls, and the slope m_R is in psi. For the penny-shaped fracture, h is twice the size of fracture radius. The term kh/μ is the reservoir transmissibility.

Chapter 3

Finite element formulation of hydraulic fracturing model

3.1 Finite element formulation

The finite element method has been used extensively to model hydraulic fracturing because of its ability to deal with irregular domains and heterogeneous material properties (Bao, 2014; Salimzadeh, 2016). Other numerical methods such as the phase field method (Chukwudozie, 2016) and extended finite element method (Salimzadeh, 2015) have also been proposed to simulate hydraulic fracture in saturated porous media.

The standard Galerkin method and the finite difference techniques are applied for spatial and time discretization in this study, respectively. The finite element formulation for the two-dimensional model is presented in this section. The finite element formulation for the three-dimensional model can be obtained using the same approach (See Appendix B).

3.1.1 The equilibrium equation

By multiplying the equilibrium equation (2.1) with the weight function w and integrating over the domain, the weak form of the equilibrium equation can be written as

$$\int_{\Omega} w \frac{\partial \sigma_{ij}}{\partial x_j} d\Omega = 0 \tag{3.1}$$

The body force was ignored in equation (3.1). Integrating by parts of equation (3.1) results in

$$-\int_{\Omega} \frac{\partial w}{\partial x_j} \sigma_{ij}\, d\Omega + \int_{\Omega} \frac{\partial (w \sigma_{ij})}{\partial x_j} d\Omega = 0 \tag{3.2}$$

Using the Gauss divergence theorem, equation (3.2) becomes

$$\int_{\Omega} \frac{\partial w}{\partial x_j} \sigma_{ij}\, d\Omega = \int_{\Gamma} w \sigma_{ij} n_j d\Gamma \tag{3.3}$$

Substituting the formula of total stress into equation (3.3) results in

$$\int_{\Omega} \frac{\partial w}{\partial x_j} \left(\sigma'_{ij} - \alpha p \delta_{ij}\right) d\Omega = \int_{\Gamma_t} w \sigma_{ij} n_j d\Gamma + \int_{\Gamma_c} w p n_i d\Gamma \tag{3.4}$$

For the first term on the right side of equation (3.4), $\sigma_{ij} n_j$ represents the traction applied at the outer boundary, which is denoted as T_i. The second term on the right side of equation (3.4) represents the fluid pressure within the fracture applied at the fracture surfaces. By writing the effective stress in terms of the fourth order elasticity tensor c_{ijkl} and displacement, equation (3.4) becomes

$$\int_{\Omega} \frac{\partial w}{\partial x_j} c_{ijkl} \frac{\partial u_k}{\partial x_l} d\Omega - \int_{\Omega} \alpha \frac{\partial w}{\partial x_i} p\, d\Omega - \int_{\Gamma_t} w \sigma_{ij} n_j d\Gamma - \int_{\Gamma_c} w p n_i d\Gamma = 0 \tag{3.5}$$

The fourth order elasticity tensor c_{ijkl} can also be expressed as

$$c_{ijkl} = \frac{2Gv}{1-2v}\delta_{ij}\delta_{kl} + G\left(\delta_{ik}\delta_{jl} + \delta_{il}\delta_{jk}\right) \tag{3.6}$$

Substituting equation (3.6) into equation (3.5) results in

$$\int_\Omega \frac{\partial w}{\partial x_j}\frac{2Gv}{1-2v}\delta_{ij}\delta_{kl}\frac{\partial u_k}{\partial x_l}d\Omega + \int_\Omega \frac{\partial w}{\partial x_j}G\left(\delta_{ik}\delta_{jl} + \delta_{il}\delta_{jk}\right)\frac{\partial u_k}{\partial x_l}d\Omega$$

$$-\int_\Omega \alpha\frac{\partial w}{\partial x_i}p\,d\Omega - \int_{\Gamma_c} w p n_i d\Gamma = \int_{\Gamma_t} w\sigma_{ij}n_j d\Gamma \tag{3.7}$$

The first term of equation (3.7) can be written as

$$\int_\Omega \frac{\partial w}{\partial x_j}\frac{2Gv}{1-2v}\delta_{ij}\delta_{kl}\frac{\partial u_k}{\partial x_l}d\Omega = \int_\Omega \frac{2Gv}{1-2v}\frac{\partial w}{\partial x_i}\frac{\partial u_j}{\partial x_j}d\Omega \tag{3.8}$$

The second term of equation (3.7) can be written as

$$\int_\Omega \frac{\partial w}{\partial x_j}G\left(\delta_{ik}\delta_{jl} + \delta_{il}\delta_{jk}\right)\frac{\partial u_k}{\partial x_l}d\Omega$$

$$= \int_\Omega \frac{\partial w}{\partial x_j}G\delta_{ik}\delta_{jl}\frac{\partial u_k}{\partial x_l}d\Omega + \int_\Omega \frac{\partial w}{\partial x_j}G\delta_{il}\delta_{jk}\frac{\partial u_k}{\partial x_l}d\Omega$$

$$= \int_\Omega G\frac{\partial w}{\partial x_j}\frac{\partial u_i}{\partial x_j}d\Omega + G\int_\Omega \frac{\partial w}{\partial x_j}\frac{\partial u_j}{\partial x_i}d\Omega \tag{3.9}$$

Hence, equation (3.7) becomes

$$\int_\Omega \frac{2Gv}{1-2v}\frac{\partial w}{\partial x_i}\frac{\partial u_j}{\partial x_j}d\Omega + \int_\Omega G\frac{\partial w}{\partial x_j}\frac{\partial u_i}{\partial x_j}d\Omega + G\int_\Omega \frac{\partial w}{\partial x_j}\frac{\partial u_j}{\partial x_i}d\Omega$$

$$-\int_\Omega \alpha\frac{\partial w}{\partial x_i}p\,d\Omega - \int_{\Gamma_c} w p n_i d\Gamma = \int_{\Gamma_t} w\sigma_{ij}n_j d\Gamma \tag{3.10}$$

Displacements, pressure, and weight function can be approximated over a finite element by the expressions

$$u_i \approx u_i^e = u_{ib}^e N_b^e,\ u_j \approx u_j^e = u_{jb}^e N_b^e,\ p \approx p^e = p_b^e N_b^e,\ w \approx N_a^e \tag{3.11}$$

where u_{ib}^e, u_{jb}^e, and p_b^e are the values of u_i^e, u_j^e, and p^e at the bth node of the element, respectively, N_a^e and N_b^e are shape functions. The summation sign is omitted because of the repeated indices. Substituting equation (3.11) into equation (3.10) can obtain

$$\int_\Omega \frac{2Gv}{1-2v}\frac{\partial N_a^e}{\partial x_i}\frac{\partial N_b^e}{\partial x_j}d\Omega u_{jb}^e + \int_\Omega G\frac{\partial N_a^e}{\partial x_j}\frac{\partial N_b^e}{\partial x_j}d\Omega u_{ib}^e + \int_\Omega G\frac{\partial N_a^e}{\partial x_j}\frac{\partial N_b^e}{\partial x_i}d\Omega u_{jb}^e$$

$$-\int_\Omega \alpha\frac{\partial N_a^e}{\partial x_i}N_b^e\, d\Omega p_b^e - \int_{\Gamma_c} N_a^e N_b^e n_i d\Gamma p_b^e = \int_{\Gamma_t} N_a^e \sigma_{ij} n_j d\Gamma \tag{3.12}$$

where the subscript e stands for a typical finite element. From equation (3.12), the finite element model of the equilibrium equation in the x direction takes the form

$$(K_{11})_{ab}^e u_{1b}^e + (K_{12})_{ab}^e u_{2b}^e - (C_{m1})_{ab}^e p_b^e - \left(C_{f1}\right)_{ab}^e p_b^e = (T_1)_{ab}^e \tag{3.13}$$

The coefficient matrices in equation (3.13) are given by

$$(K_{11})_{ab}^e = \int_\Omega \left[\frac{2G(1-v)}{1-2v}\frac{\partial N_a^e}{\partial x_1}\frac{\partial N_b^e}{\partial x_1} + G\frac{\partial N_a^e}{\partial x_2}\frac{\partial N_b^e}{\partial x_2}\right]d\Omega \tag{3.14a}$$

$$(K_{12})_{ab}^e = \int_\Omega \left[\frac{2Gv}{1-2v}\frac{\partial N_a^e}{\partial x_1}\frac{\partial N_b^e}{\partial x_2} + G\frac{\partial N_a^e}{\partial x_2}\frac{\partial N_b^e}{\partial x_1}\right]d\Omega \tag{3.14b}$$

$$(C_{m1})_{ab}^e = \int_\Omega \alpha\frac{\partial N_a^e}{\partial x_1}N_b^e\, d\Omega \tag{3.14c}$$

$$\left(C_{f1}\right)_{ab}^e = \int_{\Gamma_c} N_a^e N_b^e n_1 d\Gamma \tag{3.14d}$$

$$(T_1)_{ab}^e = \int_{\Gamma_t} N_a^e t_1 d\Gamma \tag{3.14e}$$

Similarly, the finite element model of the equilibrium equation in the y direction takes the form

$$(K_{21})^e_{ab}u^e_{1b} + (K_{22})^e_{ab}u^e_{2b} - (C_{m2})^e_{ab}p^e_b - \left(C_{f2}\right)^e_{ab}p^e_b = (T_2)^e_{ab} \tag{3.15}$$

where

$$(K_{21})^e_{ab} = \int_\Omega \left[\frac{2Gv}{1-2v}\frac{\partial N^e_a}{\partial x_2}\frac{\partial N^e_b}{\partial x_1} + G\frac{\partial N^e_a}{\partial x_1}\frac{\partial N^e_b}{\partial x_2}\right] d\Omega \tag{3.16a}$$

$$(K_{22})^e_{ab} = \int_\Omega \left[G\frac{\partial N^e_a}{\partial x_1}\frac{\partial N^e_b}{\partial x_1} + \frac{2G(1-v)}{1-2v}\frac{\partial N^e_a}{\partial x_2}\frac{\partial N^e_b}{\partial x_2}\right] d\Omega \tag{3.16b}$$

$$(C_{m2})^e_{ab} = \int_\Omega \alpha\frac{\partial N^e_a}{\partial x_2}N^e_b\, d\Omega \tag{3.16c}$$

$$\left(C_{f2}\right)^e_{ab} = \int_{\Gamma_c} N^e_a N^e_b n_2 d\Gamma \tag{3.16d}$$

$$(T_2)^e_{ab} = \int_{\Gamma_t} N^e_a t_2 d\Gamma \tag{3.16e}$$

The coefficient matrices $(K_{11})^e_{ab}$, $(K_{12})^e_{ab}$, $(K_{21})^e_{ab}$, and $(K_{22})^e_{ab}$ can also be expressed in terms of K and G using the following relations

$$\frac{2G(1-v)}{1-2v} = K + \frac{4}{3}G \tag{3.17a}$$

$$\frac{2Gv}{1-2v} = K - \frac{2}{3}G \tag{3.17b}$$

3.1.2 The storage equation

Multiplying equation (2.7) by the weighing function, w, and integrating over the domain results in

$$\alpha \int_{\Omega} \omega \frac{\partial}{\partial t}\left(\frac{\partial u_i}{\partial x_i}\right) d\Omega + S \int_{\Omega} \omega \frac{\partial p}{\partial t} d\Omega - \frac{k}{\mu} \int_{\Omega} \omega \left(\frac{\partial^2 p}{\partial x_i \partial x_i}\right) d\Omega = 0 \Rightarrow$$

$$\alpha \int_{\Omega} \omega \frac{\partial}{\partial t}\left(\frac{\partial u_i}{\partial x_i}\right) d\Omega + S \int_{\Omega} \omega \frac{\partial p}{\partial t} d\Omega + \frac{k}{\mu} \int_{\Omega} \frac{\partial \omega}{\partial x_i} \frac{\partial p}{\partial x_i} d\Omega$$

$$-\frac{k}{\mu} \int_{\Gamma} \omega \frac{\partial p}{\partial x_i} n_i d\Gamma = 0 \tag{3.18}$$

Substituting $u_i \approx u_{ib}^e N_b^e$, $p \approx p_b^e N_b^e$, and $\omega \approx N_a^e$ into equation (3.18)

$$\alpha \int_{\Omega} N_a^e \frac{\partial}{\partial t}\left(\frac{\partial N_b^e}{\partial x_i}\right) d\Omega u_{ib}^e + S \int_{\Omega} N_a^e \frac{\partial N_b^e}{\partial t} d\Omega p_b^e + \frac{k}{\mu} \int_{\Omega} \frac{\partial N_a^e}{\partial x_i} \frac{\partial N_b^e}{\partial x_i} d\Omega p_b^e$$

$$-\frac{k}{\mu} \int_{\Gamma} N_a^e \frac{\partial N_b^e}{\partial x_i} n_i d\Gamma p_b^e = 0 \tag{3.19}$$

From equation (3.19), the finite element model of the storage equation takes the form

$$(C_{m1}^T)_{ab}^e \frac{\partial}{\partial t}(u_{1b}^e) + (C_{m2}^T)_{ab}^e \frac{\partial}{\partial t}(u_{2b}^e) + (M_m)_{ab}^e \frac{\partial}{\partial t}(p_b^e) + (H_m)_{ab}^e p_b^e - (L)_{ab}^e p_b^e = 0 \tag{3.20}$$

where

$$(C_{m1}^T)_{ab}^e = \alpha \int_{\Omega} N_a^e \frac{\partial N_b^e}{\partial x_1} d\Omega \tag{3.21a}$$

$$(C_{m2}^T)_{ab}^e = \alpha \int_{\Omega} N_a^e \frac{\partial N_b^e}{\partial x_2} d\Omega \tag{3.21b}$$

$$(M_m)_{ab}^e = S \int_{\Omega} N_a^e N_b^e \, d\Omega \tag{3.21c}$$

$$(H_m)_{ab}^e = \frac{k}{\mu} \int_{\Omega} \left[\frac{\partial N_a^e}{\partial x_1} \frac{\partial N_b^e}{\partial x_1} + \frac{\partial N_a^e}{\partial x_2} \frac{\partial N_b^e}{\partial x_2}\right] d\Omega \tag{3.21d}$$

$$(L)_{ab}^e = \frac{k}{\mu} \int_{\Gamma} \left[N_a^e \frac{\partial N_b^e}{\partial x_1} n_1 + N_a^e \frac{\partial N_b^e}{\partial x_2} n_2\right] d\Gamma \tag{3.21e}$$

where the superscript T represents transpose.

3.1.3 The fracture flow equation

Multiplying equation (2.12) by the weighing function, w, and integrating over the domain results in

$$\int_{\Omega} w \frac{\partial}{\partial x_\beta}\left(\frac{w^3}{12\mu}\frac{\partial p_f}{\partial x_\beta}\right) d\Omega = \int_{\Omega} w \frac{\partial w}{\partial t}\, d\Omega + \int_{\Omega} w q_L\, d\Omega \Longrightarrow$$

$$-\frac{w^3}{12\mu}\int_{\Omega}\frac{\partial w}{\partial x_\beta}\frac{\partial p}{\partial x_\beta} d\Omega + \frac{w^3}{12\mu}\int_{\Gamma} w \frac{\partial p}{\partial x_\beta} n_\beta d\Gamma - \int_{\Omega} w \frac{\partial w}{\partial t}\, d\Omega + \int_{\Omega} w \frac{k}{\mu}\frac{\partial p}{\partial x_i} n_i\, d\Omega = 0 \tag{3.22}$$

For the two-dimensional model, the subscript β in equation (2.3) can be omitted for simplicity. Substituting $w = (u_i^+ - u_i^-)\, n_i$, $u_i \approx u_{ib}^e N_b^e$, $p \approx p_b^e N_b^e$, and $w \approx N_a^e$ into equation (3.22)

$$\int_{\Gamma} N_a^e \frac{\partial N_b^e n_1}{\partial t} d\Gamma u_{1b}^e + \int_{\Gamma} N_a^e \frac{\partial N_b^e n_2}{\partial t} d\Gamma u_{2b}^e + \frac{w^3}{12\mu}\int_{\Gamma}\frac{\partial N_a^e}{\partial x}\frac{\partial N_b^e}{\partial x} d\Gamma p_b^e$$

$$-\frac{k}{\mu}\int_{\Gamma}\left[N_a^e \frac{\partial N_b^e}{\partial x_1} n_1 + N_a^e \frac{\partial N_b^e}{\partial x_2} n_2\right] d\Gamma p_b^e = Q^e \tag{3.23}$$

For the two-dimensional model, the finite element model of fracture flow equation can be written as

$$\left(C_{f1}^T\right)_{ab}^e \frac{\partial}{\partial t}(u_{1b}^e) + \left(C_{f2}^T\right)_{ab}^e \frac{\partial}{\partial t}(u_{2b}^e) + \left(H_f\right)_{ab}^e p_b^e - (L)_{ab}^e p_b^e = Q^e \tag{3.24}$$

where

$$\left(C_{f1}^{T}\right)_{ab}^{e} = \int_{\Gamma} N_a^e N_b^e n_1 \, d\Gamma \tag{3.25a}$$

$$\left(C_{f2}^{T}\right)_{ab}^{e} = \int_{\Gamma} N_a^e N_b^e n_2 \, d\Gamma \tag{3.25b}$$

$$\left(H_f\right)_{ab}^{e} = \frac{w^3}{12\mu} \int_{\Gamma} \frac{\partial N_a^e}{\partial x} \frac{\partial N_b^e}{\partial x} d\Gamma \tag{3.25c}$$

$$(L)_{ab}^{e} = \frac{k}{\mu} \int_{\Gamma} \left[N_a^e \frac{\partial N_b^e}{\partial x_1} n_1 + N_a^e \frac{\partial N_b^e}{\partial x_2} n_2 \right] d\Gamma \tag{3.25d}$$

Equation (3.13), (3.15), (3.20), and (3.24) can be written in the matrix form, both the superscript and the subscript are omitted for simplicity.

$$\begin{bmatrix} [0] & [0] & [0] \\ [0] & [0] & [0] \\ C_{m1}^{T} + C_{f1}^{T} & C_{m2}^{T} + C_{f2}^{T} & M_m \end{bmatrix} \frac{\partial}{\partial t} \begin{bmatrix} u_1 \\ u_2 \\ p \end{bmatrix} + \begin{bmatrix} K_{11} & K_{12} & -C_{m1} - C_{f1} \\ K_{21} & K_{22} & -C_{m2} - C_{f2} \\ [0] & [0] & H_m + H_f - L \end{bmatrix} \begin{bmatrix} u_1 \\ u_2 \\ p \end{bmatrix} = \begin{bmatrix} T_1 \\ T_2 \\ Q \end{bmatrix} \tag{3.26}$$

Figure 3.1 shows the spatial discretization of porous medium and fracture for the KGD model. The porous medium is discretized using black triangular elements and the fracture is discretized using red linear elements. The linear elements are matched with the sides of triangular elements that are connected to the fracture. They share the same nodes that are represented by the blue points in the figure. Therefore, by extending the coefficient matrices for the fracture flow equation with zeros so that all coefficient matrices have the same dimensions, the coefficient matrices for the fracture flow equation can be added to the corresponding coefficient matrices for the storage equation. In the fully coupled model, the fracture flow equation is combined with the storage equation to serve as a constraint.

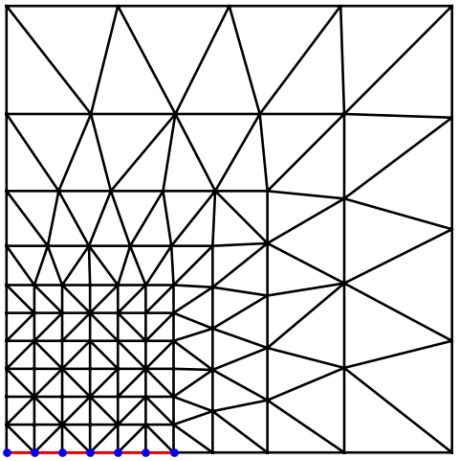

Figure 3.1: Spatial discretization of porous medium and fracture for the KGD model

Similarly, for the penny-shaped model, the porous medium is discretized using eight-node brick elements, and the fracture surface is discretized using rectangular elements. The rectangular elements are matched with the faces of brick elements that are connected to the fracture surface.

For both the two-dimensional and three-dimensional models, the local coordinate system is used for the purpose of numerical integration. The element in a local coordinate system is called master element. The integration limits of the integrals transform to the limits of the local coordinates, which is from -1 to 1. In addition, for the three-dimensional model, the integration over master rectangular element and master brick element can be numerically evaluated through the Gauss-Legendre quadrature formulas.

3.1.4 Time discretization

Equation (3.26) contains the first-time derivative of displacement and pressure. The weighted average of time derivatives at two consecutive time steps is used for time discretization, which takes the form (Reddy, 2019)

$$(1-\psi)\dot{\lambda}_s + \psi\dot{\lambda}_{s+1} = \frac{\lambda_{s+1}-\lambda_s}{\Delta t_{s+1}}, \quad 0 \le \psi \le 1 \tag{3.27}$$

where λ_s is the value of $\lambda(t)$ at time $t = t_s = \sum_{i=1}^{s} \Delta t_i$, $\Delta t_s = t_s - t_{s-1}$is the sth time step. When $\psi = 0$, equation (3.27) can reduce to

$$\dot{\lambda}_s = \frac{\lambda_{s+1}-\lambda_s}{\Delta t_{s+1}} \tag{3.28}$$

Equation (3.28) is known as the forward difference approximation since the value of the function in the following step is used. When $\psi = 1$, equation (3.27) can reduce to

$$\dot{\lambda}_{s+1} = \frac{\lambda_{s+1}-\lambda_s}{\Delta t_{s+1}} \rightarrow \dot{\lambda}_s = \frac{\lambda_s - \lambda_{s-1}}{\Delta t_s} \tag{3.29}$$

Therefore, equation (3.29) is known as the backward difference approximation. The backward difference approximation is chosen in this study because of its high stability, then the time derivative of displacement and pressure can be expressed as

$$\frac{du_i}{dt} = \frac{u_i^s - u_i^{s-1}}{\Delta t_s}, \quad \frac{dp}{dt} = \frac{p^s - p^{s-1}}{\Delta t_s} \tag{3.30}$$

The global matrix can be obtained by substituting equation (3.30) into equation (3.26)

$$\begin{bmatrix} K_{11} & K_{12} & -C_{m1} - C_{f1} \\ K_{21} & K_{22} & -C_{m2} - C_{f2} \\ C_{m1}^T + C_{f1}^T & C_{m2}^T + C_{f2}^T & M_m + (H_m + H_f - L)\Delta t \end{bmatrix} \begin{bmatrix} u_1^s \\ u_2^s \\ p^s \end{bmatrix}$$

$$= \begin{bmatrix} [0] & [0] & [0] \\ [0] & [0] & [0] \\ C_{m1}^T + C_{f1}^T & C_{m2}^T + C_{f2}^T & M_m \end{bmatrix} \begin{bmatrix} u_1^{s-1} \\ u_2^{s-1} \\ p^{s-1} \end{bmatrix} + \begin{bmatrix} T_1 \\ T_2 \\ Q\Delta t_s \end{bmatrix} \quad (3.31)$$

In the global matrix above, K is the mechanical stiffness matrix, C_m is the poroelastic coupling matrix, and C_f is the hydro-mechanical coupling matrix.

3.2 Validation of the model

3.2.1 Line fracture

The first benchmark is the deformation of a line crack under the action of internal pressure. As shown in Figure 3.2, a thin crack with a length of $2l$ is located at the center of an infinite two-dimensional medium and a uniform pressure p_0 is applied to the crack.

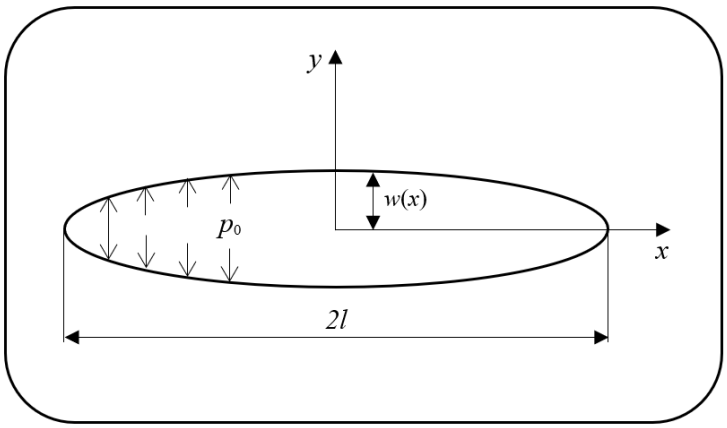

Figure 3.2: Line crack under uniform pressure

The displacement along the crack in the y direction is given by [Sneddon, 1946]

$$w(x) = \frac{2(1-v^2)p_0}{E}\sqrt{l^2 - x^2} \tag{3.32}$$

Figure 3.3 shows the opening profile of a line crack under a uniform pressure of 1 MPa, the Young's modulus and the Poisson's ratio are set to 37.5 GPa and 0.25, respectively.

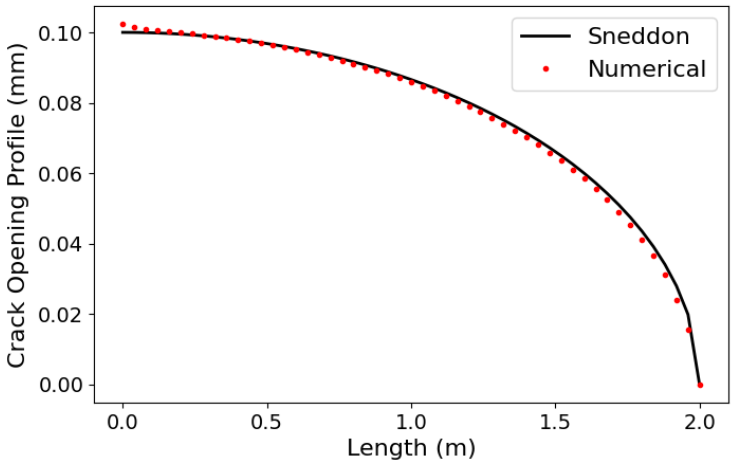

Figure 3.3: Line crack opening profile

3.2.2 Mandel's problem

Mandel's problem is a canonical example of linear poroelasticity, which is often used to validate the computational model. Mandel's problem is illustrated in Figure 3.4, which shows a poroelastic medium that is located between two rigid and impermeable plates. A uniformly distributed force is instantly applied to these plates at time zero and then held constant. Free drainage is allowed in two lateral directions.

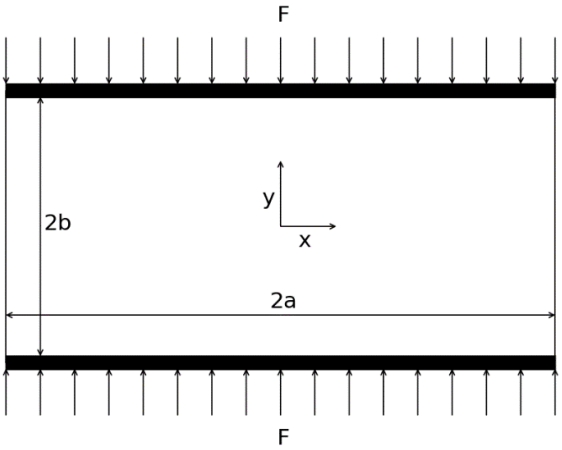

Figure 3.4: The setup of Mandel's problem

Because of the symmetry, one-quarter of the domain is selected as the computational domain and is spatially discretized using 5,000 uniform triangular elements. The analytical solutions of horizontal displacement, vertical displacement, and pore pressure are as follows (Cheng and Detournay, 1988)

$$u = \left[\frac{Fv}{2Ga} - \frac{Fv_u}{Ga}\sum_{i=1}^{\infty}\frac{\sin\alpha_i\cos\alpha_i}{\alpha_i - \sin\alpha_i\cos\alpha_i}\exp\left(-\frac{\alpha_i^2 c}{a^2}t\right)\right]x$$

$$+\frac{F}{G}\sum_{i=1}^{\infty}\frac{\cos\alpha_i}{\alpha_i - \sin\alpha_i\cos\alpha_i}\sin\frac{\alpha_i x}{a}\exp\left(-\frac{\alpha_i^2 c}{a^2}t\right) \tag{3.33a}$$

$$v = \left[-\frac{F(1-v)}{2Ga} + \frac{F(1-v_u)}{Ga}\sum_{i=1}^{\infty}\frac{\sin\alpha_i\cos\alpha_i}{\alpha_i - \sin\alpha_i\cos\alpha_i}\exp\left(-\frac{\alpha_i^2 c}{a^2}t\right)\right]y \tag{3.33b}$$

$$p = \frac{2FB(1+v_u)}{3a}\sum_{i=1}^{\infty}\frac{\sin\alpha_i}{\alpha_i - \sin\alpha_i\cos\alpha_i}\left(\cos\frac{\alpha_i x}{a} - \cos\alpha_i\right)\exp\left(-\frac{\alpha_i^2 c}{a^2}t\right) \tag{3.33c}$$

where α_i are the solutions to the equation

$$\tan\alpha_i = \frac{1-v}{v_u - v}\alpha_i \tag{3.34}$$

and where B is Skempton's parameter, v is the drained Poisson's ratio, v_u is the undrained Poisson's ratio and c is the hydraulic diffusivity, which is defined as

$$c = \frac{2(k/\mu)B^2G(1-v)(1+v_u)^2}{9(1-v_u)(v_u-v)} \tag{3.35}$$

The Biot coefficient and the specific storage coefficient can be obtained using the equations below

$$\alpha = \frac{3(v_u-v)}{B(1-2v)(1+v_u)} \tag{3.36a}$$

$$S = \frac{\alpha^2(1-2v_u)(1-2v)}{2G(v_u-v)} \tag{3.36b}$$

The relevant parameters for Mandel's problem are listed in Table 3.1:

Table 3.1: Input parameters for Mandel's problem

Parameter	Definition	Magnitude	Units
G	Shear Modulus	20	GPa
v	Drained Poisson's ratio	0.2	-
v_u	Undrained Poisson's ratio	0.4	-
B	Skempton's coefficient	0.8	-
k	Permeability	1×10^{-19}	m^2
μ	Viscosity	0.001	Pa·s
a	Length	0.1	m
b	Width	0.1	m
F	Force	3×10^6	N/m

Figure 3.5 shows the numerical and analytical solutions of horizontal displacement, vertical displacement, and pore pressure at t = 1 s, 125 s, 500 s, and 1000 s. The analytical solutions are presented with dotted lines, and the numerical solutions are presented with solid lines.

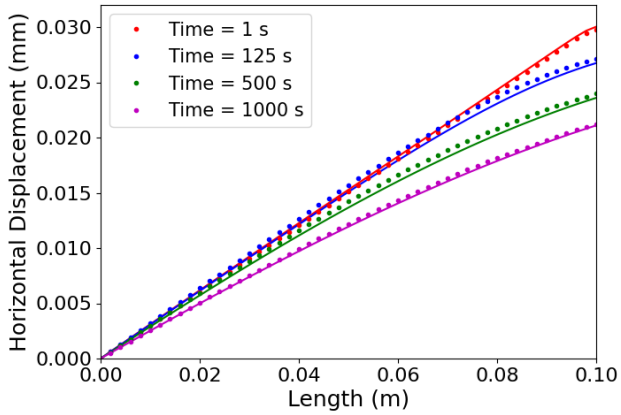

(a)

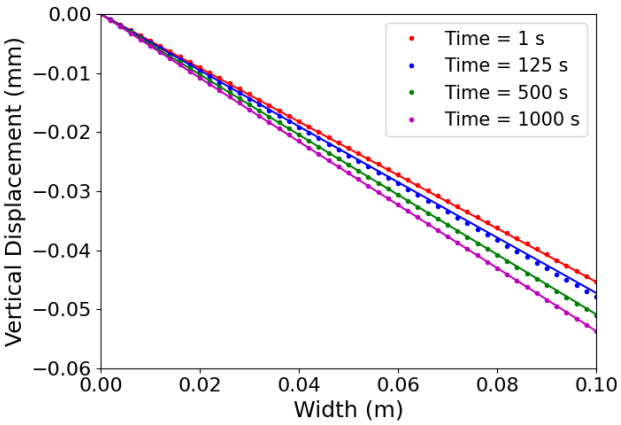

(b)

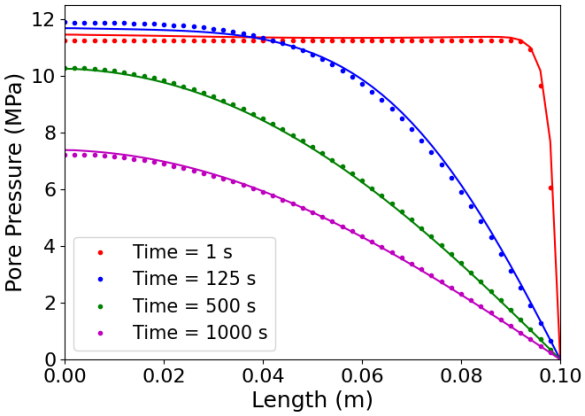

(c)

Figure 3.5: Horizontal displacement (a), vertical displacement (b), and pore pressure (c) at different times for Mandel's problem

It should be noted that the pore pressure goes up in the center of the domain at earlier stages before it starts to fall. This phenomenon is known as the Mandel-Cryer Effect, which has been proved by the laboratory experiment (Verruijt, 2016). Figure 3.6 shows the surface plots of horizontal displacement, vertical displacement, and pore pressure at time t = 500 s.

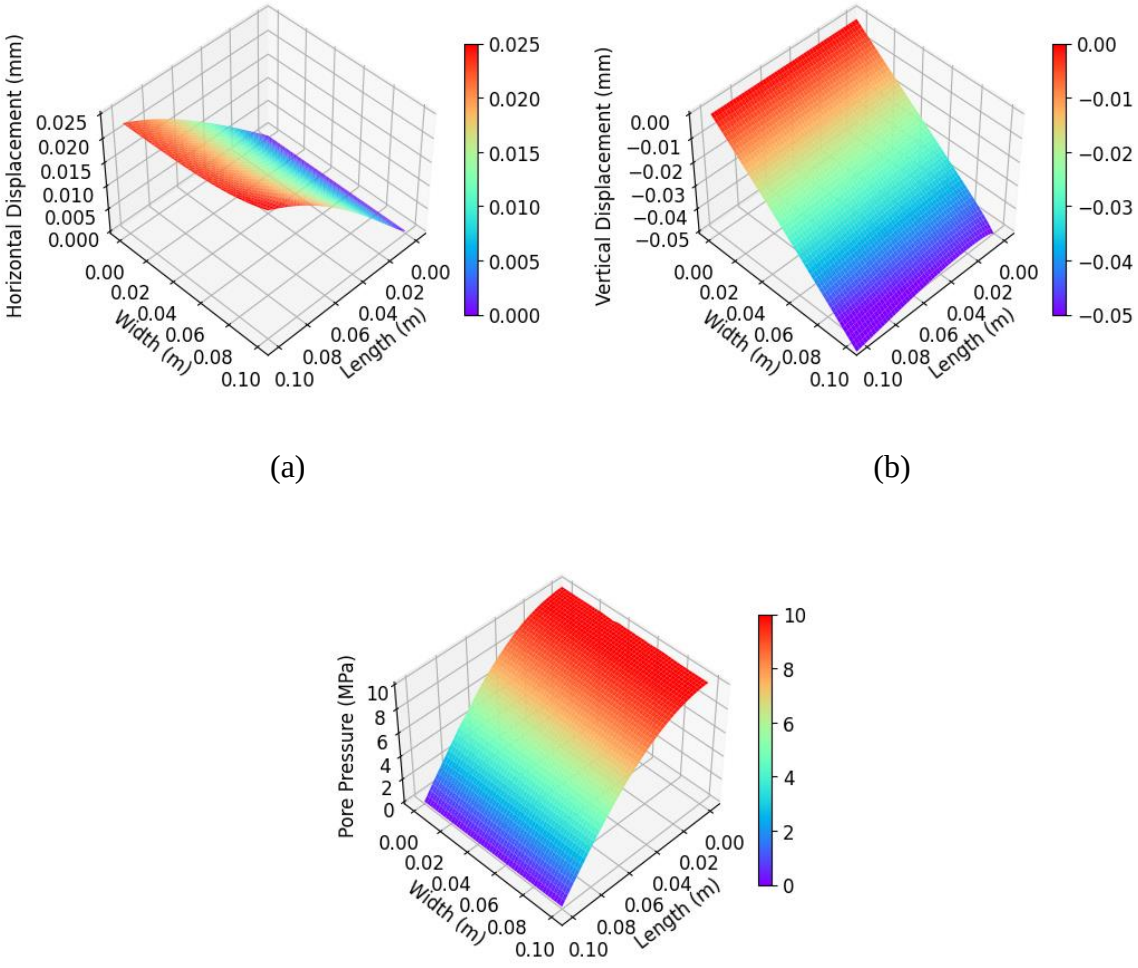

(a) (b)

(c)

Figure 3.6: Surface plots of horizontal displacement (a), vertical displacement (b), and pore pressure (c) at time t = 500 s for Mandel's problem

3.2.3 KGD model

According to the two competing energy dissipation mechanisms and the two competing fluid storage mechanisms, the fracture propagation process can be divided into four regimes under limiting conditions (Bunger, 2005). As shown in Figure 3.7, the bottom edge is the storage-dominated regime, which is associated with the fluid storage within the fracture. The top edge is the leak-off dominated regime which is associated with the leak-off of fluid into the formation. The left edge is the viscosity-dominated regime which corresponds to the flow of viscous fluid. The right edge is the toughness-dominated regime, which corresponds to the creation of a surface area in the solid material.

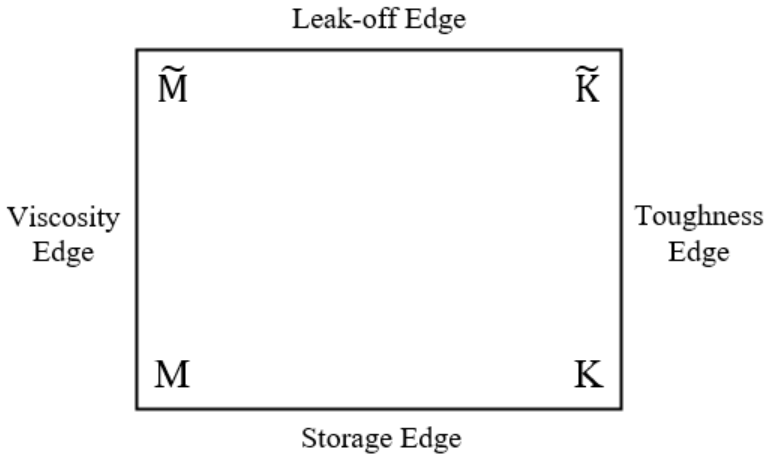

Figure 3.7: Propagation regimes of hydraulic fractures (after Bunger, 2005)

Using the scaling technique, analytical solutions of fracture opening w, net pressure p, and fracture length l for the KGD model can be expressed as (Detournay, 2004)

$$w(x,t) = \varepsilon(t)L(t)\Omega[\xi, \mathcal{P}(t)] \tag{3.37a}$$

$$p(x,t) = \varepsilon(t)E'\Pi[\xi, \mathcal{P}(t)] \tag{3.37b}$$

$$l(t) = \gamma[\mathcal{P}(t)]L(t) \tag{3.37c}$$

where ξ is the scaled coordinate and is equal to x/l, Ω, Π, and γ are dimensionless quantities that represent opening, net pressure, and length, respectively, L denotes a length scale of the same order of fracture length l, $\mathcal{P}(t)$ is the dimensionless evolution parameter and $\gamma[\mathcal{P}(t)]$ is the dimensionless fracture length that depends on t.

In the toughness-dominated regime, $\varepsilon(t)$ and $L(t)$ take the form

$$\varepsilon_k = \left(\frac{K'^4}{E'^4 Q_0 t}\right)^{1/3}, \quad L_k = \left(\frac{E' Q_0 t}{K'}\right)^{2/3} \tag{3.38}$$

where K' is defined as

$$K' = 4\left(\frac{2}{\pi}\right)^{1/2} K_{IC} \tag{3.39}$$

The zero viscosity solution for the KGD model is

$$\bar{\Omega}_{k0} = \frac{\pi^{1/3}}{2}(1-\xi^2)^{1/2}, \quad \Pi_{k0} = \frac{\pi^{1/3}}{8}, \quad \gamma_{k0} = \frac{2}{\pi^{2/3}} \tag{3.40}$$

where $\bar{\Omega}_{k0}$ is equal to Ω_{k0}/γ_{k0}.

In the viscosity-dominated regime, $\varepsilon(t)$ and $L(t)$ take the form

$$\varepsilon_m = \left(\frac{\mu'}{E' t}\right)^{1/3}, \quad L_m = \left(\frac{E' Q_0^3 t^4}{\mu'}\right)^{1/6} \tag{3.41}$$

where μ' is defined as

$$\mu' = 12\mu \tag{3.42}$$

The fracture propagation regime can be distinguished by the dimensionless toughness $\varkappa$, which is defined as

$$\varkappa = \frac{K'}{(E'^3 \mu' Q_0)^{1/4}} \tag{3.43}$$

For the KGD model, the fracture propagation regime is considered as toughness-dominated when $\varkappa$ is larger than 4 and viscosity-dominated when $\varkappa$ is smaller than 1. The first order approximation of zero toughness solution is (Garagash, 2005)

$$\overline{\Omega}_{m0} = a_{01}(1-\xi^2)^{2/3} + a_{02}(1-\xi^2)^{5/3} + a_{03}\left[2\sqrt{1-\xi^2} + \xi^2 \ln\left|\frac{1-\sqrt{1-\xi^2}}{1+\sqrt{1+\xi^2}}\right|\right] \tag{3.44a}$$

$$\Pi_{m0} = b_{01}\,{}_2F_1\left(-\frac{1}{6}, 1; \frac{1}{2}; \xi^2\right) + b_{02}\,{}_2F_1\left(-\frac{7}{6}, 1; \frac{1}{2}; \xi^2\right) + b_{03}(2-\pi|\xi|) \tag{3.44b}$$

where $\overline{\Omega}_{m0}$ is equal to Ω_{m0}/γ_{m0}, $a_{01} \simeq 1.73205$, $a_{02} \simeq -0.15601$, $a_{03} \simeq 0.13264$, $b_{01} \simeq 0.475449$, $b_{02} \simeq -0.061178$, $b_{03} \simeq 0.066322$, and ${}_2F_1$ is the hypergeometric function.

The parameters used to validate the KGD model are listed in Table 3.2.

Table 3.2: Parameters used to validate the KGD model

Parameter	Definition	Toughness-dominated	Viscosity-dominated
G (GPa)	Shear modulus	15	15
K (GPa)	Drained bulk modulus	25	25
μ (Pa·s)	Viscosity	0.001	0.2
t (s)	Injection time	100	100
K_{IC} (MPa·m$^{0.5}$)	Fracture toughness	8	0.2
q (m^3/s)	Injection rate	5×10^{-4}	5×10^{-4}

Figure 3.8 shows the finite element mesh for the KGD model. A domain with a size of 200×200 m is chosen to model the problem. Because of the symmetry of the problem, one-quarter of the domain with a size of 100×100 m is selected as the computational domain and is spatially discretized using 6,472 triangles. The fracture represented by the red line is discretized using linear elements.

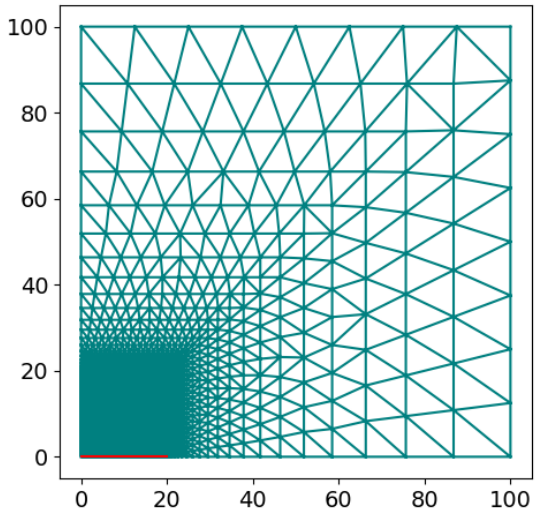

Figure 3.8: Finite element mesh for the KGD model

Figure 3.9 and Figure 3.10 show the fracture opening, wellbore pressure, and fracture length versus injection time for a toughness-dominated case and a viscosity-dominated case, respectively. The dimensionless toughness $\varkappa$ is 5.77 for the toughness-dominated case and is 0.038 for the viscosity-dominated case. With the same injection rate and time, the viscosity-dominated case yields higher fracture width and lower fracture length.

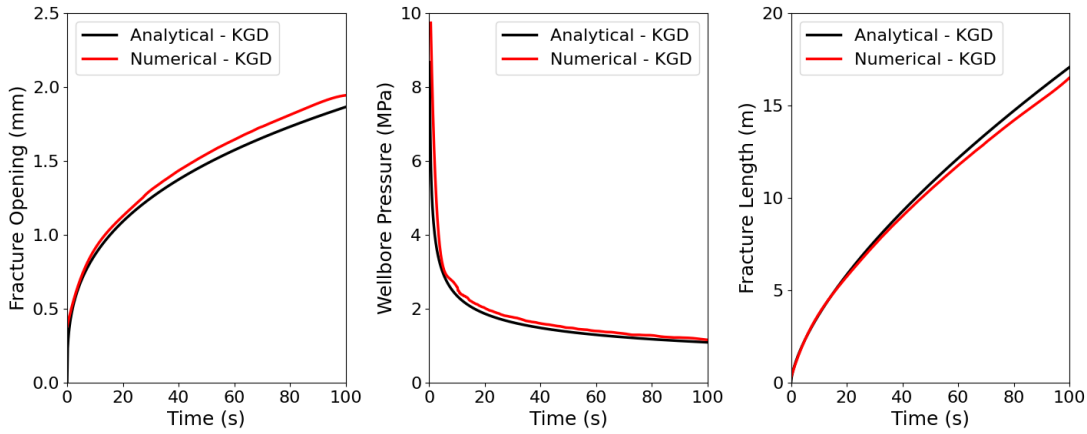

Figure 3.9: Fracture opening, wellbore pressure, and fracture length versus injection time for toughness-dominated case

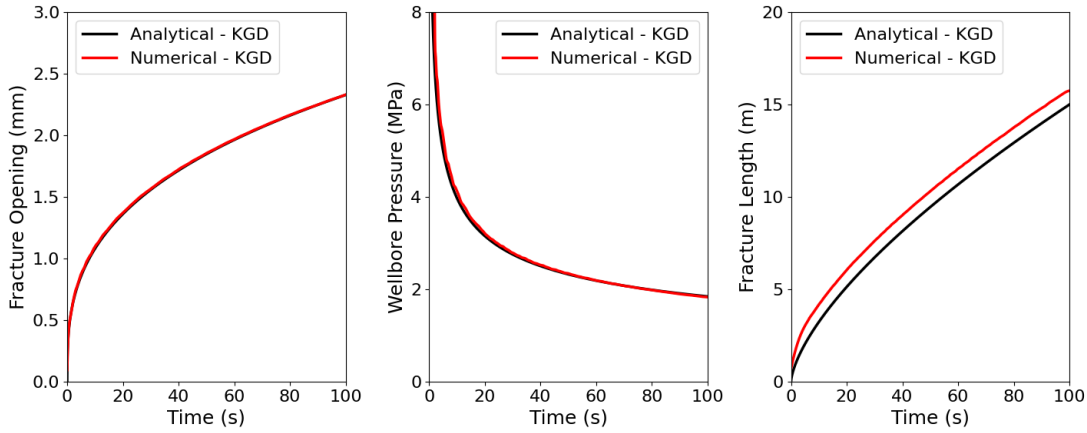

Figure 3.10: Fracture opening, wellbore pressure, and fracture length versus injection time for viscosity-dominated case

Bunger (2005) presented the analytical solution for a toughness-dominated regime with leak-off, which can be expressed as

$$w = \varepsilon L \Omega(\xi, \bar{\tau}), \quad p = \varepsilon E' \Pi(\xi, \bar{\tau}), \quad l = \gamma(\bar{\tau}) L \tag{3.45}$$

where

$$t = t_* \bar{\tau}, \quad x = l(t)\xi \tag{3.46}$$

where the timescale t_* is given by

$$t_* = \frac{K'^4 Q_0^2}{E'^4 C'^6} \tag{3.47}$$

where

$$C' = 2C_L \tag{3.48}$$

For a toughness-dominated regime with leak-off, the small parameter and the lengthscale can be expressed as

$$\varepsilon = \frac{C'^2}{Q_0}, \quad L = \left(\frac{K' Q_0}{E' C'^2}\right)^2 \tag{3.49}$$

For small value of $\bar{\tau}$, the fracture opening and pressure can be written as

$$\Omega = 2^{-1/2} \gamma^{1/2} (1 - \xi^2)^{1/2}, \quad \Pi = 2^{-5/2} \gamma^{-1/2} \tag{3.50}$$

where

$$\gamma(\bar{\tau}) = \bar{\tau}^{\beta} \sum_{i=0}^{n} \gamma_{ki} \bar{\tau}^{i\alpha}, \quad \tau \ll 1 \tag{3.51}$$

where $\beta = 2/3$ and $\alpha = 1/6$ for the KGD model. The first five coefficients of γ_{ki} for the small time asymptotic solutions (equation 3.51) are $\gamma_{k0} = 0.9324$, $\gamma_{k1} = -1.714$, $\gamma_{k2} = 2.196$, $\gamma_{k3} = -1.863$, and $\gamma_{k4} = 0.7093$.

Figure 3.11 shows the comparison between total injected volume and fracture volume. The leak-off coefficient C_L is set to 7×10^{-5} m/$\sqrt{\text{s}}$ in this simulation, other parameters are same as those listed in Table 3.2 for the toughness-dominated case. A fluid efficiency of 33.3% can be obtained using equation (2.26). Figure 3.12 shows the fracture opening, wellbore pressure, and fracture length versus injection time for a toughness-dominated case with leak-off.

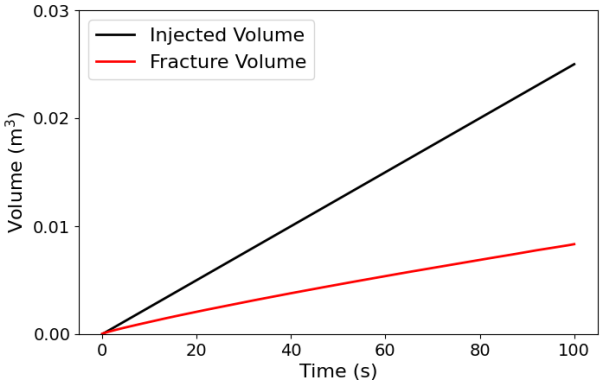

Figure 3.11: Fracture volume versus injected volume

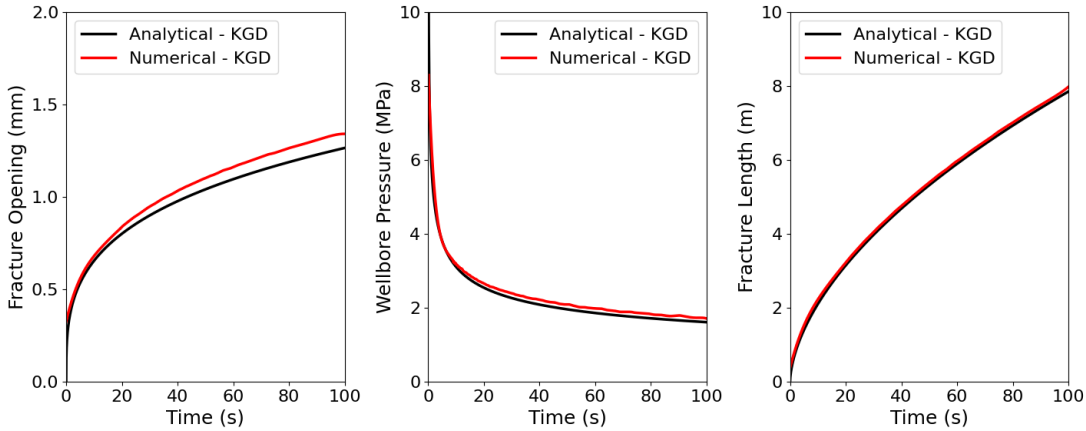

Figure 3.12: Fracture opening, wellbore pressure, and fracture length versus injection time for toughness-dominated case with leak-off

3.2.4 Penny-shaped model

Similarly, analytical solutions of fracture opening w, net pressure p, and fracture radius R for the penny-shaped model can be expressed as (Savitski and Detournay, 2002)

$$w(r,t) = \varepsilon(t)L(t)\Omega[\rho, \mathcal{P}(t)] \tag{3.52a}$$

$$p(r,t) = \varepsilon(t)E'\Pi[\rho, \mathcal{P}(t)] \tag{3.52b}$$

$$R(t) = \gamma[\mathcal{P}(t)]L(t) \tag{3.52c}$$

In the toughness-dominated regime, $\varepsilon(t)$ and $L(t)$ are written as

$$\varepsilon_k = \left(\frac{K'^6}{E'^6 Q_0 t}\right)^{1/5}, \quad L_k = \left(\frac{Q_0^2 E'^2 t^2}{K'^2}\right)^{1/5} \tag{3.53}$$

The zero viscosity solution for the penny-shaped model is

$$\Omega_{k0} = \left(\frac{3}{8\pi}\right)^{1/5} (1-\rho^2)^{1/2}, \quad \Pi_{k0} = \frac{\pi}{8}\left(\frac{\pi}{12}\right)^{1/5}, \quad \gamma_{k0} = \left(\frac{3}{\pi 2^{1/2}}\right)^{2/5} \tag{3.54}$$

The fracture propagation regime is distinguished by dimensionless toughness $\varkappa$, which is defined as

$$\varkappa = K'\left(\frac{t^2}{\mu'^5 Q_0^3 E'^{13}}\right)^{1/18} \tag{3.55}$$

Unlike the KGD model, the dimensionless toughness in the penny-shaped model also depends on time. The value of $\varkappa$ will change from the viscosity-dominated regime to the toughness-dominated regime. The fracture propagation regime is considered as toughness-dominated when $\varkappa$ is larger than 3.5 and viscosity-dominated when $\varkappa$ is less than 1.

Figure 3.13 shows the finite element mesh for the penny-shaped model, one eighth of the domain is selected and spatially discretized using 6,048 eight-node brick elements.

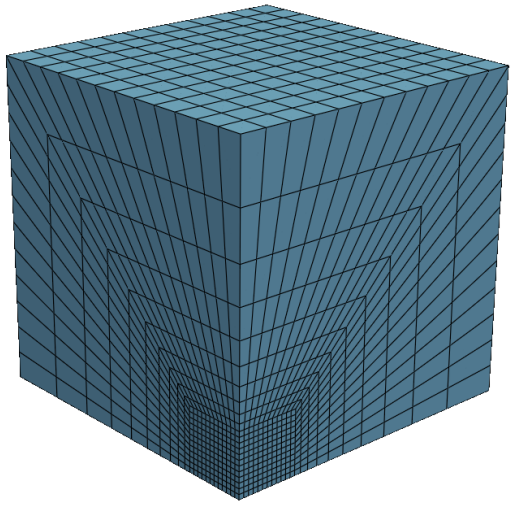

Figure 3.13: Finite element mesh for the penny-shaped model

Figure 3.14 shows the fracture opening, wellbore pressure, and fracture radius versus injection time for toughness-dominated case. The fluid is injected into the facture with a constant rate of 1×10^{-2} m^3/s, other parameters are as same as those listed in Table 3.2.

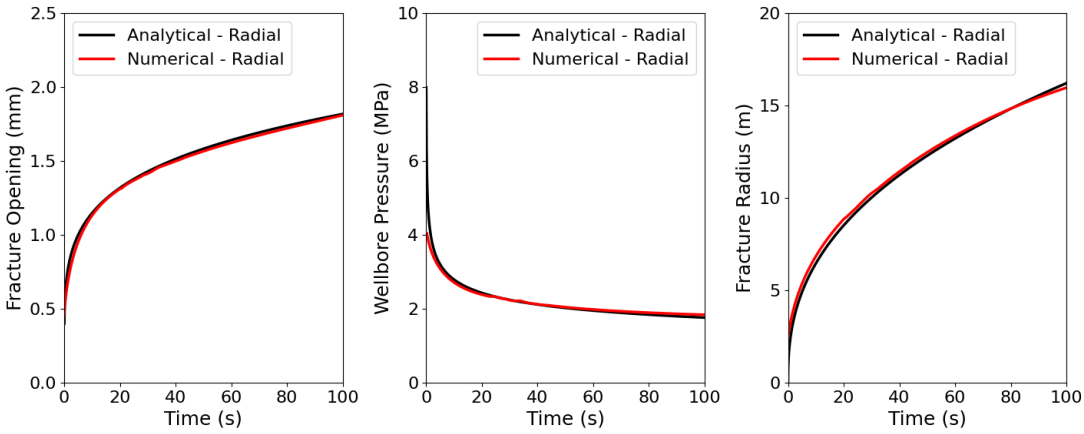

Figure 3.14: Fracture opening, wellbore pressure, and fracture radius versus injection time for toughness-dominated case

The general consistency between the analytical and numerical solutions for both KGD model and penny-shaped model demonstrates that current model can deal with the hydromechanical coupling process in fracture propagation.

Chapter 4

Poroelastic effects on DFIT analysis in the KGD model

4.1 Leak-off comparison

Most current DFIT techniques were developed based on Carter's leak-off model. Poroelastic effects are usually not considered due to the reservoir's low permeability. Leak-off calculated with and without the consideration of poroelastic effects is studied in this section.

Figure 4.1 shows the schematic diagram of one-dimensional leak-off. A constant pressure of 35 MPa is applied to the left boundary and lasts for 100 hours. The solid bulk modulus and the fluid bulk modulus are 45.4 GPa and 2.25 GPa, respectively. Shear modulus, drained bulk modulus, and viscosity are listed in Table 3.2. With permeability ranging from $4 \times 10^{-19}\,\mathrm{m}^2$ to $4 \times 10^{-17}\,\mathrm{m}^2$ and porosity ranging from 0.01 to 0.1, four hundred combinations of permeability and porosity are chosen for simulation by holding other parameters constant. Biot coefficient is also set to zero and denoted by the "Decoupled Model" to compare with the fully coupled model.

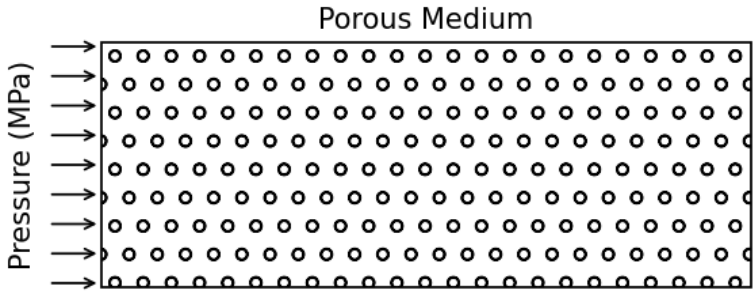

Figure 4.1: Schematic diagram of one-dimensional leak-off

Figure 4.2a shows the fluid loss per unit length calculated using the analytical solution of Carter's leak-off model for different combinations of permeability and porosity. By employing Darcy's law, the fluid loss in the coupled model is shown in Figure 4.2b. Figure 4.2c shows the relative difference between Carter's model and the coupled model. The coupled model yields a higher leak-off in general. When porosity is smaller than 0.03, the difference for most corresponding combinations falls within the range of 35% to 105%. Similarly, Figure 4.2d and Figure 4.2e show the leak-off in the decoupled model and the difference between Carter's model and the decoupled model, respectively. The decoupled model leads to a slightly lower leak-off for most combinations, which falls within the range of negative 4% to 12%.

Figure 4.3 shows the leak-off comparison of different models at t = 1000 hours. As shown in Figure 4.3c, compared with Carter's model, leak-off is underestimated when porosity is smaller than 0.03, which is consistent with the conclusions obtained from Figure 4.2.

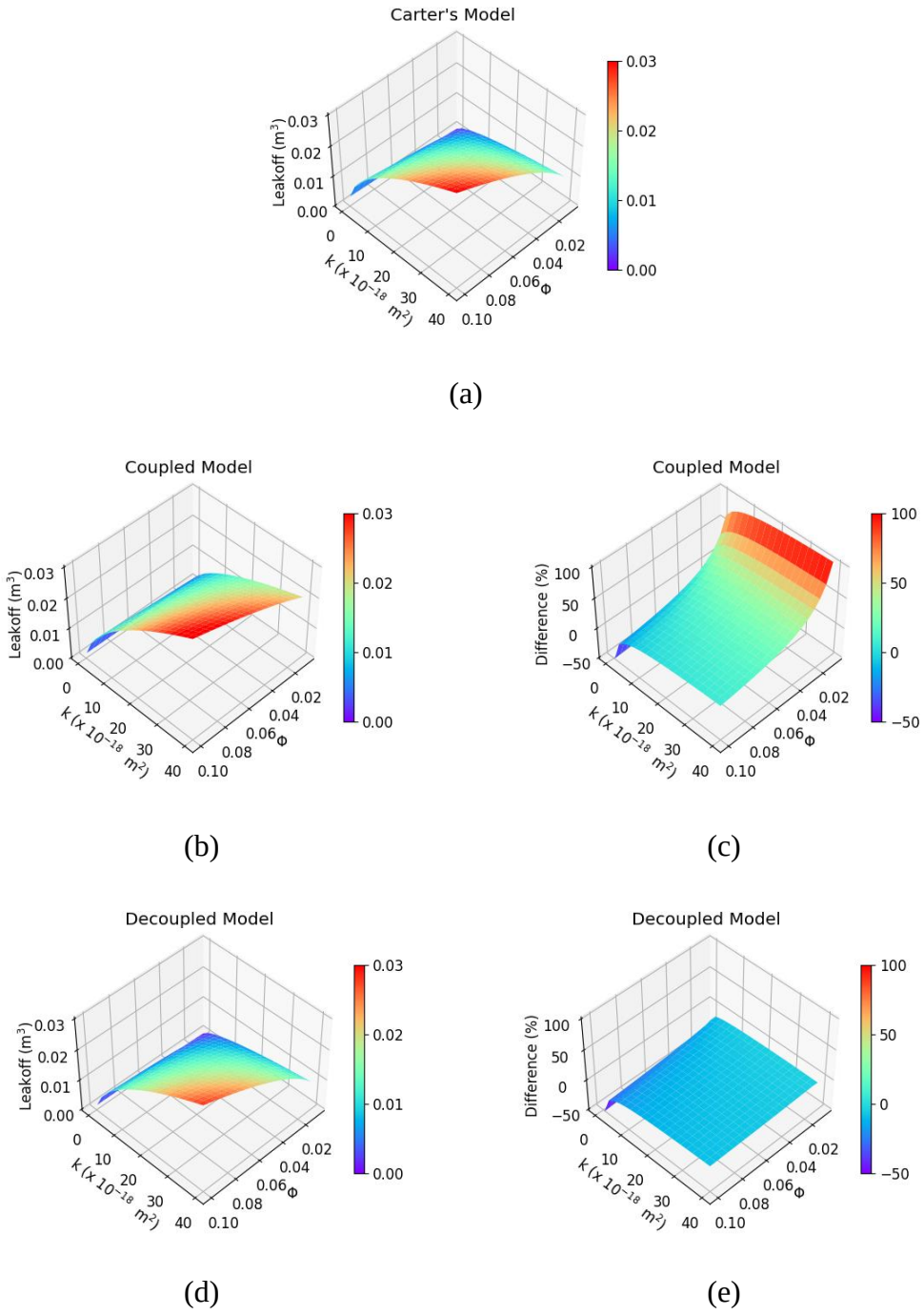

Figure 4.2: Leak-off comparison at t = 100 hours: (a) Leak-off calculated using Carter's model; (b) Leak-off calculated using the coupled model; (c) Difference between Carter's model and coupled model; (d) Leak-off calculated using the decoupled model; (e) Difference between Carter's model and decoupled model

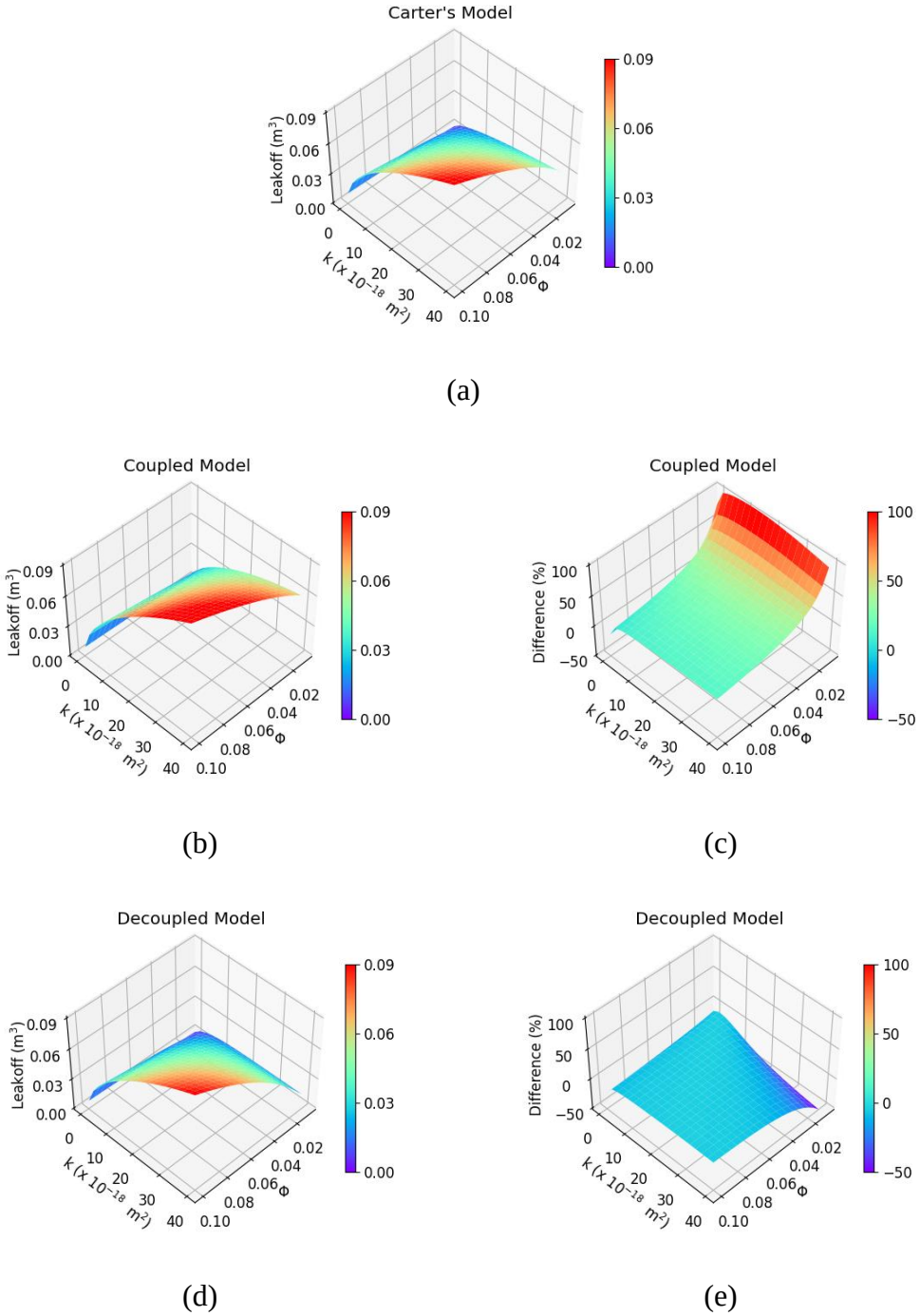

Figure 4.3: Leak-off comparison at t = 1000 hours: (a) Leak-off calculated using Carter's model; (b) Leak-off calculated using the coupled model; (c) Difference between Carter's model and coupled model; (d) Leak-off calculated using the decoupled model; (e) Difference between Carter's model and decoupled model

4.2 Poroelastic effects on BCA in the KGD model

In this section, the poroelastic effects on BCA are studied through 6 cases defined in Table 4.1. Case C1 is considered as the base model, and the poroelastic constants in C1 are selected from Cheng (2016). The well is injected for 100 seconds at a rate of $5 \times 10^{-4}\ \mathrm{m}^3/\mathrm{s}$. For each case, the Biot coefficient is also set to zero to eliminate the poroelastic effects for comparison, which is denoted by "Decoupled". In addition, the permeability in the *x* direction is set to zero in the decoupled model since Carter's model assumes that leak-off occurs only in the direction that is normal to the fracture surface.

Table 4.1: Simulation settings for different cases

Parameter	C1	C2	C3	C4	C5	C6
G (GPa)	15	15	15	15	15	15
K (GPa)	25	25	25	25	20	25
K_s (GPa)	45.4	45.4	45.4	45.4	70	45.4
K_f (GPa)	2.25	2.25	2.25	2.25	2.25	2.25
ϕ	0.01	0.1	0.01	0.1	0.01	0.01
k (m^2)	4×10^{-19}	4×10^{-19}	4×10^{-17}	4×10^{-17}	4×10^{-19}	4×10^{-19}
μ (Pa·s)	0.001	0.001	0.001	0.001	0.001	0.001
K_{IC} ($\mathrm{MPa \cdot m^{0.5}}$)	8	8	8	8	8	8
$\sigma_{\text{in-situ}}$(MPa)	35	35	35	35	35	35
p_i (MPa)	20	20	20	20	20	30

4.2.1 BCA for case 1

Figure 4.4 shows the wellbore pressure response in the fracture injection and falloff test for the base model. The initial pore pressure is 20 MPa and the in-situ stress is 35 MPa.

The fracture closure occurs at about 1.74 days, followed by the linear flow at 1.80 days. The linear flow ends at 10.71 days, and the radial flow starts at a late time of 146.44 days.

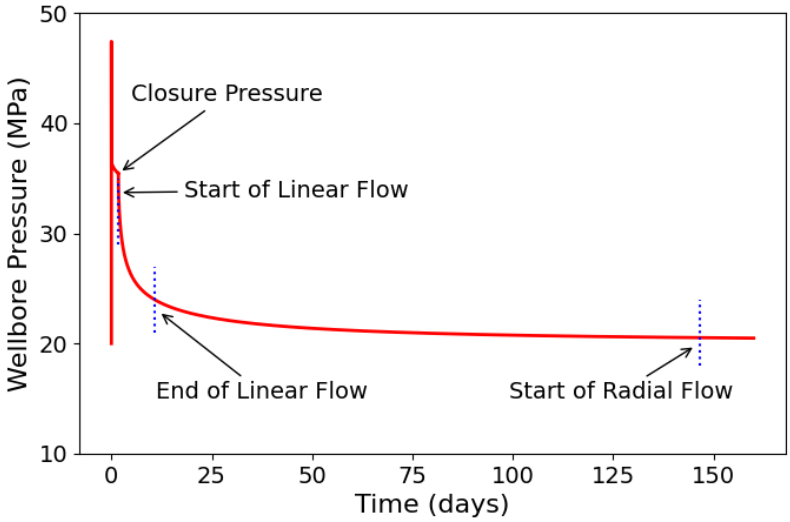

Figure 4.4: Wellbore pressure response in the base model

Figure 4.5 shows the results of G-function plots for the fully coupled model and decoupled model in case C1. The slope of the line in the left plot is -0.0112 MPa/G with an intercept of 36.50 MPa. The leak-off coefficient is estimated to be 7.06×10^{-7} m/$\sqrt{\text{s}}$ using the equation in Table 2.2 while Carter's analytical solution (equation 2.28) yields a leak-off coefficient of 4.00×10^{-7} m/$\sqrt{\text{s}}$. Similarly, for the decoupled model, the slope of the line in the right plot is -0.0066 MPa/G with an intercept of 36.19 MPa. A leak-off coefficient of 4.27×10^{-7} m/$\sqrt{\text{s}}$ is obtained, and the analytical value of the leak-off coefficient is 4.02×10^{-7} m/$\sqrt{\text{s}}$.

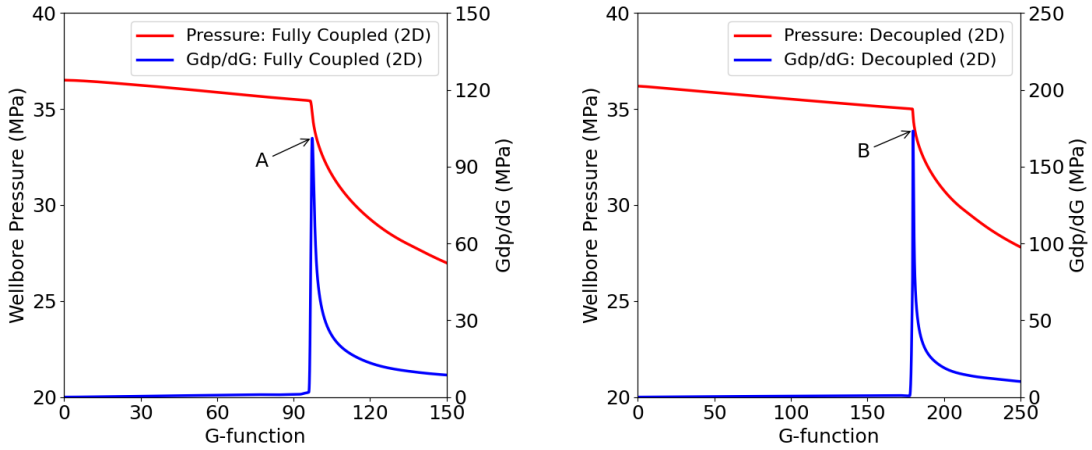

Figure 4.5: G-function plots for fully coupled model and decoupled model in C1

In the left plot, the tangent line method indicates that the fracture closes at a G-time of 97.2 (Point A) and a pressure of 34.87 MPa. In the right plot, the tangent line method shows that the fracture closes at a G-time of 179.8 (Point B) and a pressure of 34.80 MPa. The spike in the derivative indicates that the fracture is fully closed. Also, in the fully coupled model, the interaction between the formation and the fluid leaking into the formation is taken into consideration. Therefore, a higher shut-in pressure and closure pressure are obtained in the fully coupled model because of the poroelastic effects.

Figure 4.6 shows the G-function plot for the decoupled model in simulation C1 with a permeability of 4×10^{-19} m^2 in the *x* direction. In Figure 4.6, the tangent line method indicates that the fracture closes at a G-time of 161.4, which means that setting the permeability to 4×10^{-19} m^2 in the *x* direction will accelerate the fracture closure. A leak-off coefficient of 4.75×10^{-7} m$/\sqrt{\text{s}}$ can be inferred in this situation, which is larger than the one (4.27×10^{-7} m$/\sqrt{\text{s}}$) obtained from the right plot in Figure 4.5. The difference

between the two leak-off coefficients is due to the assumption of one-dimensional diffusion.

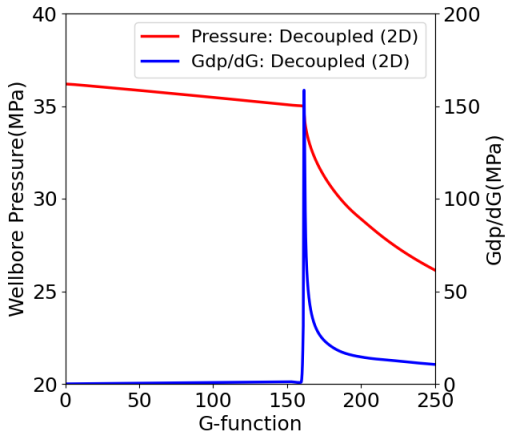

Figure 4.6: G-function plot for decoupled model in case C1 with a permeability of 4×10^{-19} m^2 in the *x* direction

Figure 4.7 shows the fracture openings and pressure profiles along the fracture after shut-in for the coupled model in simulation C1. In the left plot, the fracture length is about 15.56 m at shut-in, which corresponds to a G-time of 0. The fracture opening decreases with the increase of G-time and facture closure starts at the tip and moves gradually toward the wellbore. The fracture length is about 11.56 m at the G-time of 90.

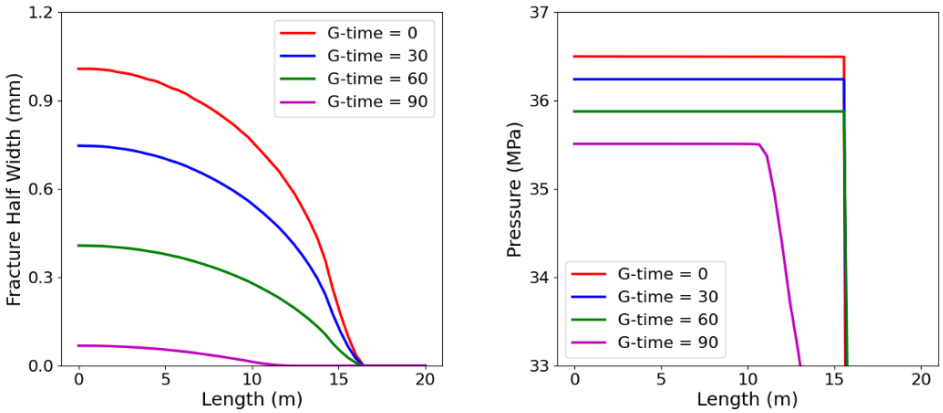

Figure 4.7: Fracture openings and pressure profiles after shut-in in case C1

Figure 4.8 shows the pressure distribution after shut-in at the G-time of 30, 60, 90, and 120, respectively. The fracturing fluid is leaked into the reservoir through the fracture surface. Therefore, the fluid pressure near the fracture surface decreases with the increase of time. Figure 4.8c shows the pressure contour at the G-time of 90 at which the fracture is partially closed. Figure 4.8d shows the pressure contour at the G-time of 120 at which the fracture is fully closed. The pressure at the wellbore is 29.30 MPa currently, which is less than the in-situ stress. Figure 4.8d indicates that the pressure will continue to decrease after the fracture is fully closed.

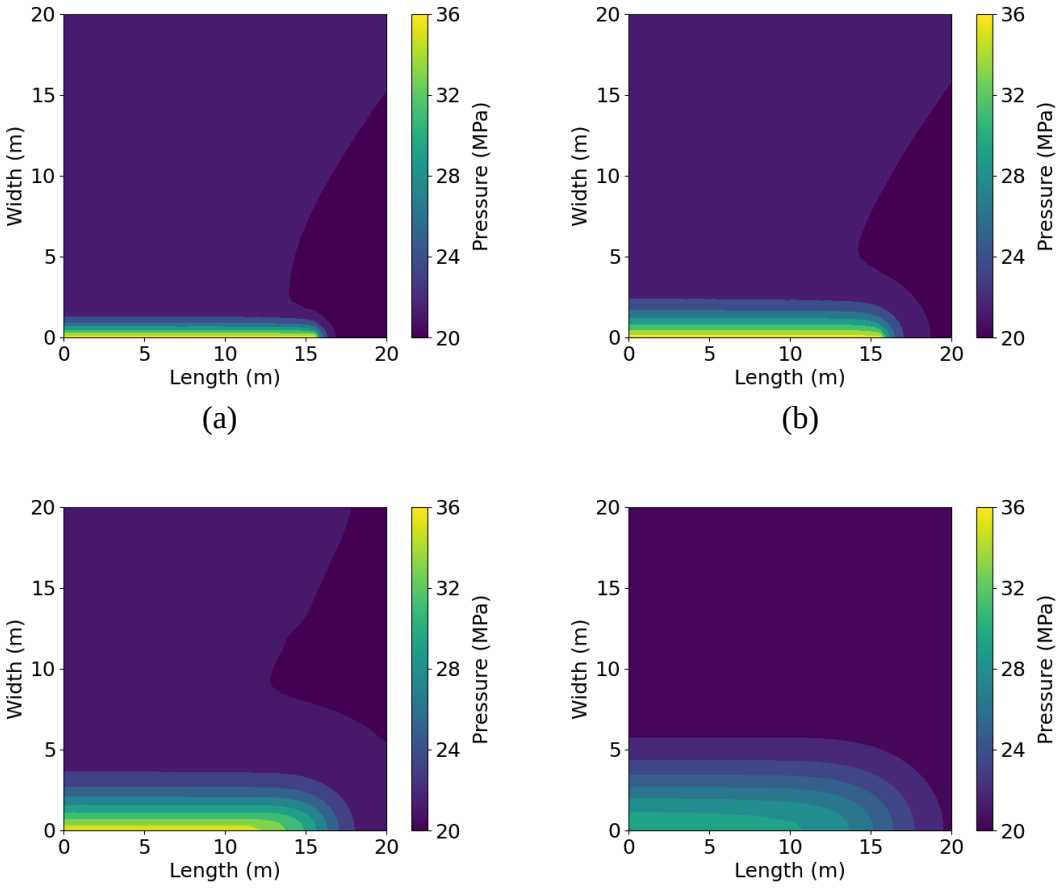

Figure 4.8: Pressure distribution near the fracture in case C1: (a) G-time = 30; (b) G-time = 60; (c) G-time = 90; (d) G-time = 120

4.2.2 BCA for case 2

In simulation C2, the porosity increases from 0.01 to 0.1 so that the specific storage coefficient increases from 1.41×10^{-11} to 5.21×10^{-11}. Compared with simulation C1, the second term $S\partial p/\partial t$ plays a more important role in the storage equation since all other constants are the same as those in C1. The leak-off coefficients for the coupled model and decoupled model are $1.14 \times 10^{-6}\ \mathrm{m}/\sqrt{\mathrm{s}}$ and $1.13 \times 10^{-6}\ \mathrm{m}/\sqrt{\mathrm{s}}$, respectively. The corresponding analytical values of the leak-off coefficient are $1.26 \times 10^{-6}\ \mathrm{m}/\sqrt{\mathrm{s}}$ for both the coupled model and the decoupled model. Simulation C2 indicates that the poroelastic effects are ignorable when the second term $S\partial p/\partial t$ in the storage equation is large compared to the first term.

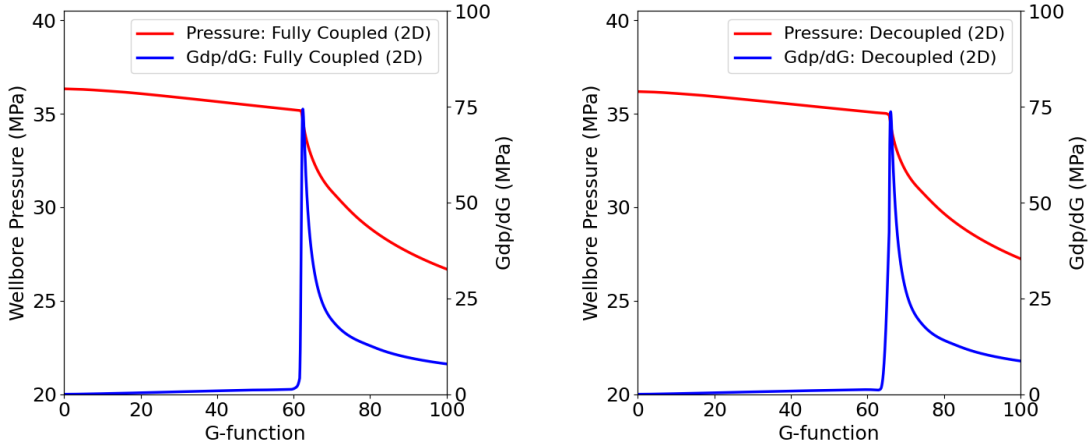

Figure 4.9: G-function plots for fully coupled model and decoupled model in C2

In the left plot, the tangent line method indicates that the closure occurs at a G-time of 62.2 and a pressure of 34.95 MPa. In the right plot, the tangent line method shows that the closure occurs at a G-time of 66.0 and a pressure of 34.60 MPa.

Figure 4.10 shows the G-function plot for the decoupled model in simulation C2 with a permeability of 4×10^{-19} m^2 in the *x* direction. The fracture closes at a G-time of 65.4, which is close to the closure time observed from the right plot in Figure 4.9. The corresponding leaf-off coefficient is 1.14×10^{-6} m$/\sqrt{\text{s}}$, which is close to the two leak-off coefficients obtained from Figure 4.9. One conclusion is drawn from Figure 4.6 and 4.10 is that the leak-off coefficient is even underestimated for the decoupled model when poroelastic effects cannot be ignored.

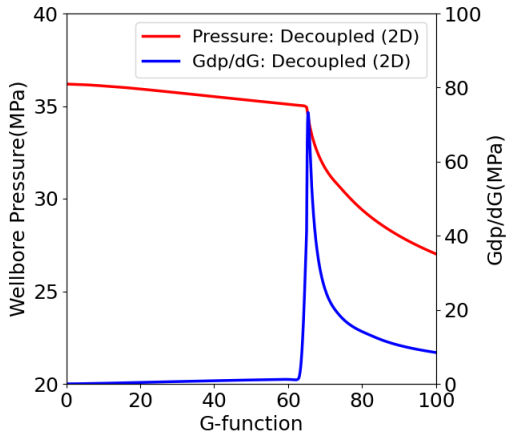

Figure 4.10: G-function plot for decoupled model in case C2 with a permeability of 4×10^{-19} m^2 in the *x* direction

4.2.3 BCA for case 3

The effect of higher permeability is investigated in simulation C3. Figure 4.11 shows the G-function plots for fully coupled model and decoupled model in C3. A change of permeability does not affect the weight of the two terms in the left side of the storage equation. Similar to simulation C1, the leak-off coefficient (6.88×10^{-6} m$/\sqrt{\text{s}}$) in the coupled model is higher than that (4.18×10^{-6} m$/\sqrt{\text{s}}$) in the decoupled model. The

corresponding analytical solutions are 4.02×10^{-6} m/$\sqrt{s}$ for both the coupled model and decoupled model.

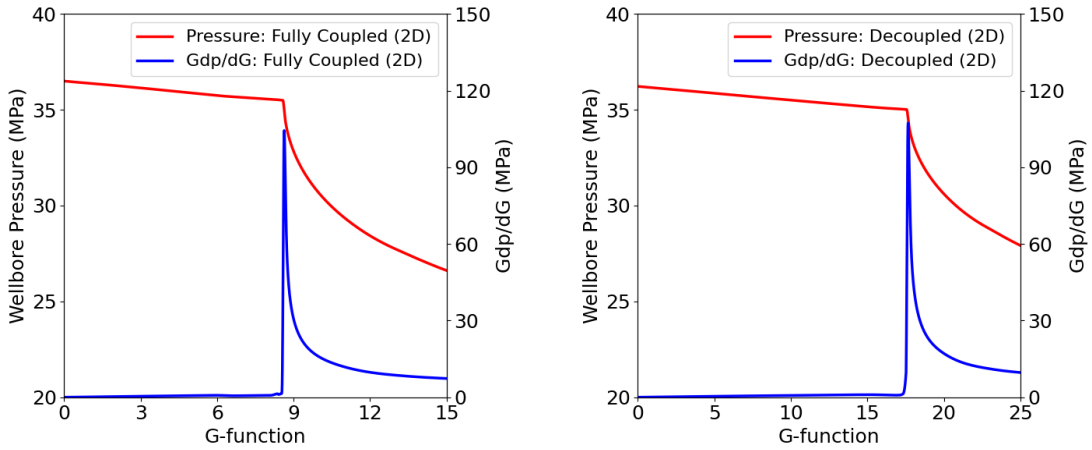

Figure 4.11: G-function plots for fully coupled model and decoupled model in C3

The accuracy of the leak-off coefficient obtained from BCA is investigated through large injection time. Figure 4.12 shows the fracture volume comparison between the fully coupled model (poroelasticity) and the Carter's leak-off model for simulation C3. The injection time increases from 100 seconds to 100 minutes. The black line represents the total injection volume versus time. The parameters used for the fully coupled model are the same as those for simulation C3. In Carter's leak-off model, the leak-off coefficient (6.88×10^{-6} m/$\sqrt{s}$) that obtained from the BCA is used for simulation.

The fluid efficiency calculated using equation (2.26) is 75.0% for the fully coupled model and 78.5% for the Cater's leak-off model, which is consistent with each other in general. In the left plot of Figure 4.11, the fracture closure occurs at a G-time of 8.62 which results in a fluid efficiency of 81.2% using equation (2.27).

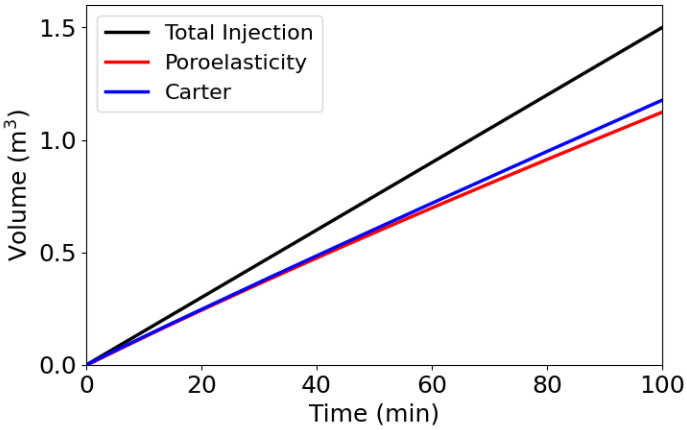

Figure 4.12: Fracture volume comparison with large injection time for C3

Figure 4.13 shows the fracture opening, wellbore pressure, and fracture length comparison between the fully coupled model and the Carter's leak-off model. The black line represents the analytical solutions of fracture opening, wellbore pressure, and fracture length for the toughness-dominated case without leak-off.

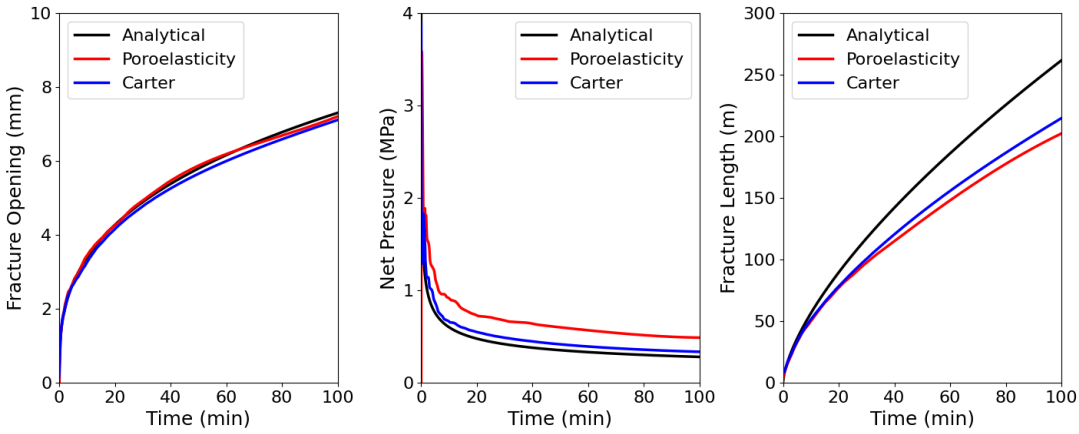

Figure 4.13: Fracture opening, wellbore pressure, and fracture length comparison with large injection time for C3

4.2.4 BCA for case 4

In simulation C4, the permeability is set to 4×10^{-17} m^2 and the porosity is set to 0.1. A larger porosity makes the second term dominate the first term, which means that it is reasonable to ignore the poroelastic effects. As expected, the leak-off coefficient in the left plot is 1.24×10^{-5} m$/\sqrt{s}$ and the analytical value is 1.27×10^{-5} m$/\sqrt{s}$. The leak-off coefficient in the right plot is 1.19×10^{-5} m$/\sqrt{s}$ and the analytical value is also 1.27×10^{-5} m$/\sqrt{s}$.

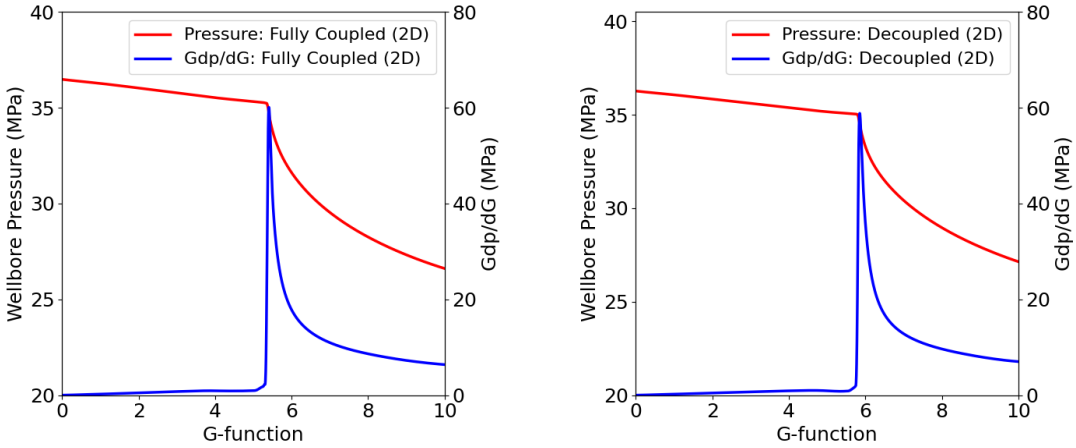

Figure 4.14: G-function plots for fully coupled model and decoupled model in C4

Figure 4.15 shows the fracture volume comparison between the fully coupled model (poroelasticity) and the Carter's leak-off model for simulation C4. The fluid efficiency for the fully coupled model and Cater's leak-off model are 64.3% and 66.5% respectively, which is consistent with each other again. The fluid efficiency calculated from the G-time at closure is 72.8%.

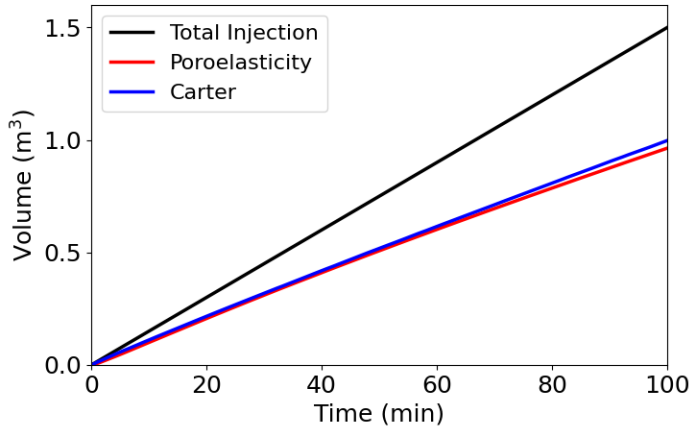

Figure 4.15: Fracture volume comparison with large injection time for C4

Figure 4.16 shows the fracture opening, wellbore pressure, and fracture length comparison between the fully coupled model and the Carter's leak-off model for simulation C4. Similar to C3, the fully coupled model leads to a higher net pressure due to the poroelastic effects.

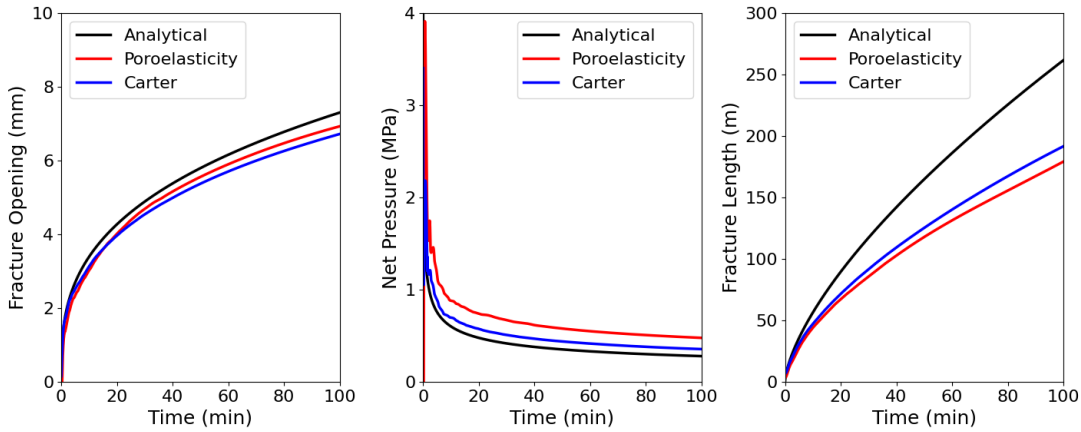

Figure 4.16: Fracture opening, wellbore pressure, and fracture length comparison with large injection time for C4

4.2.5 BCA for case 5

In simulation C5, the drained bulk modulus is set to 20 GPa and the solid bulk modulus is set to 70 GPa so that the Biot coefficient increases from 0.449 to 0.714. For the coupled model, the leak-off coefficient calculated using slope is 8.21×10^{-7} m/$\sqrt{\text{s}}$, which is 91.8 percent higher than the one for the decoupled model (4.28×10^{-7} m/$\sqrt{\text{s}}$). Simulation C5 demonstrates that an increase in Biot coefficient will further underestimate the leak-off coefficient.

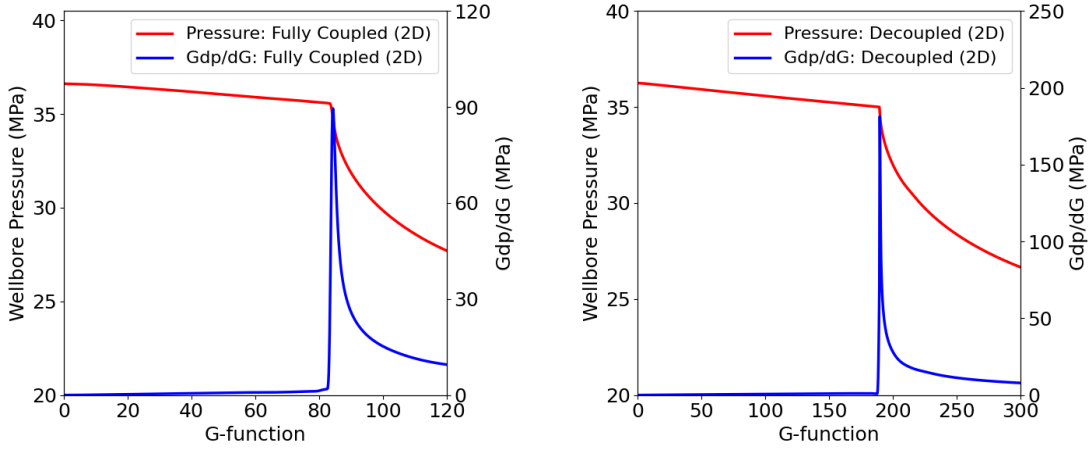

Figure 4.17: G-function plots for fully coupled model and decoupled model in C5

4.2.6 BCA for case 6

The effect of higher pore pressure is studied in simulation C6. Carter's leak-off coefficient was derived based on the assumption that the fluid net pressure ($p_f - \sigma_{\text{in-situ}}$) is much smaller than the far-field effective stress ($\sigma_{\text{in-situ}} - p_i$). Compared to previous simulations, the fluid net pressure at shut-in (1.34 MPa) accounts for a much larger fraction of far-field

effective stress (5 MPa). With a leak-off coefficient of 2.94×10^{-7} m/$\sqrt{s}$ in the left plot and a leak-off coefficient of 1.49×10^{-7} m/$\sqrt{s}$ in the right plot, simulation C6 demonstrates that poroelastic effects cannot be ignored for formation with a high pore pressure.

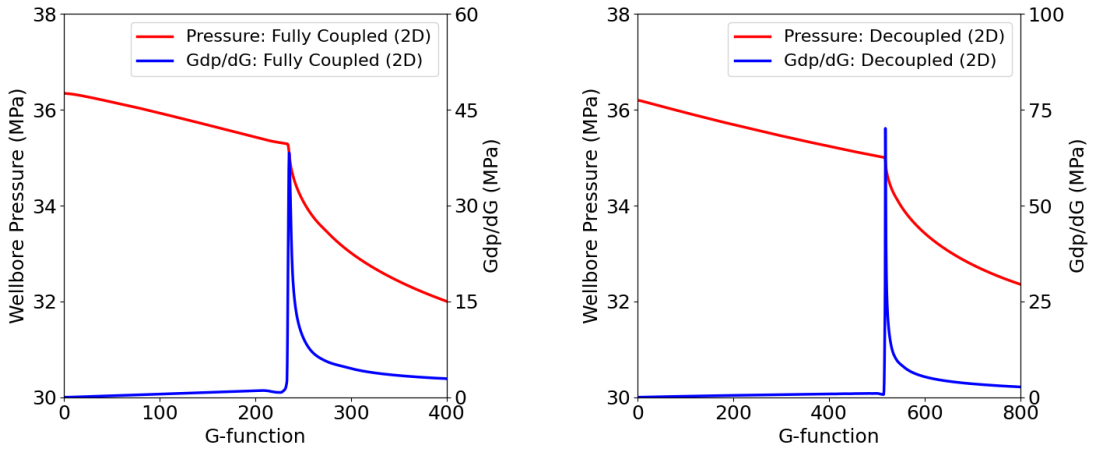

Figure 4.18: G-function plots for fully coupled model and decoupled model in C6

4.3 Poroelastic effects on ACA in the KGD Model

This section presents the poroelastic effects on ACA in the KGD Model. In the decoupled model, the permeability in the *x* direction maintains its corresponding value in each case since the radial flow analysis was developed based on the two-dimensional diffusion equation. It should be noted that an initial estimate of pore pressure is required for both the linear and radial flow analyses. In addition, the slope of the pressure derivative will not be affected by the estimated value of pore pressure (Barree et al., 2009).

4.3.1 ACA for case 1

The left plot in Figure 4.19 shows the log-log plot of pressure difference and derivative versus the square of linear flow time function in simulation C1. Two characteristics can be observed to identify the linear flow period. One is the 1/2 slope of the derivative curve. The other one is that the pressure difference is twice the magnitude of the pressure derivative. The linear flow starts at a square of linear flow time of 0.8, which is about 43.11 hours after shut-in.

The right plot in Figure 4.19 shows the log-log plot of pressure versus linear flow time function. An extrapolation of the pressure curve gives a pressure estimation of 20.0 MPa, which is exactly the input value for the pore pressure. Equation (2.32) yields a permeability of 1.45×10^{-18} m^2, which is 3.6 times higher than the input value. The discrepancy is mainly due to the difference between the leak-off coefficients calculated from the G-function method and equation (2.28).

Figure 4.20 shows the linear flow identification and analysis for the decoupled model in simulation C1. The permeability is determined to be 6.38×10^{-19} m^2 using equation (2.32). The difference between the estimated permeability and the input value is mainly due to the pressure dissipation in the *x* direction. By extrapolating the pressure trend, a good estimate of pore pressure (19.86 MPa) can still be obtained even though the characteristics of linear flow in the decoupled model are not as apparent as those in the coupled model.

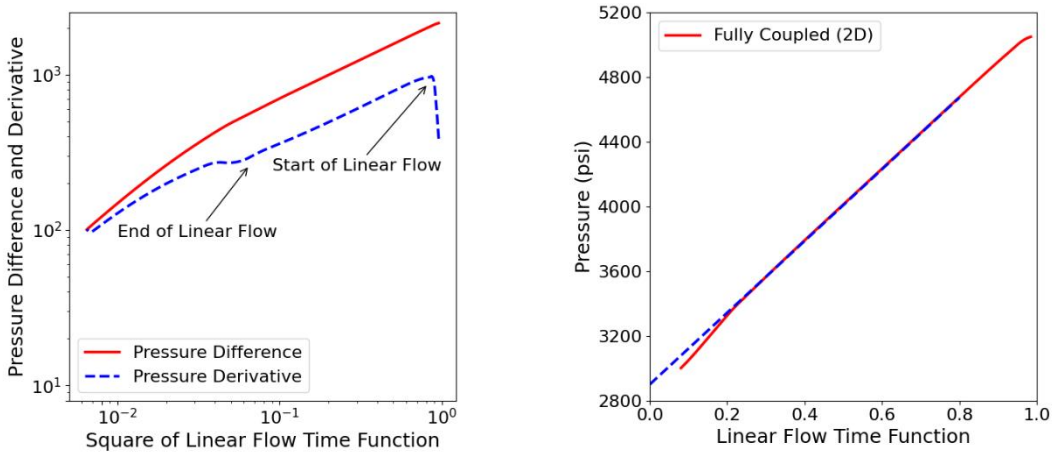

Figure 4.19: Linear flow identification and analysis for fully coupled model in C1

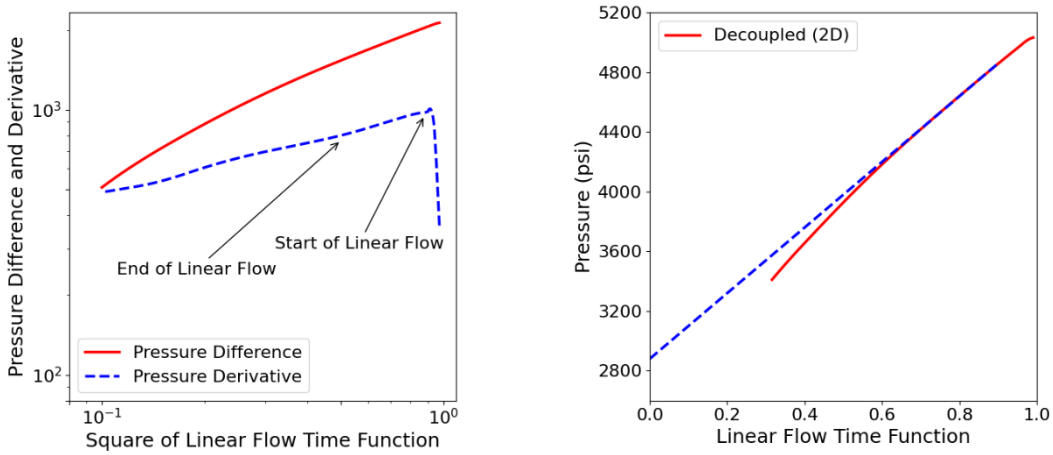

Figure 4.20: Linear flow identification and analysis for decoupled model in C1

Figure 4.21 shows the pressure distribution at the start and end of linear flow for the coupled model in simulation C1. The pressure contour in the left plot clearly shows that the fracturing fluid is dissipated into the formation in a direction that is normal to the fracture surface, which means that the fluid flow is parallel to each other during the linear flow period.

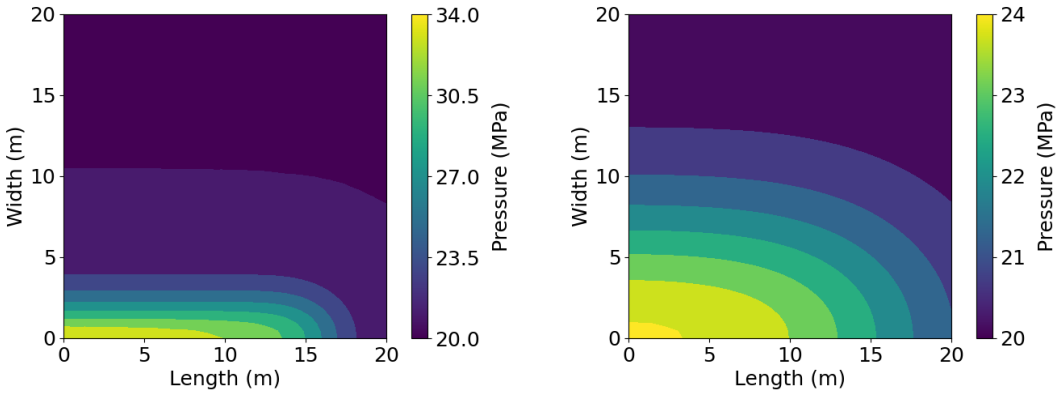

Figure 4.21: Pressure distribution at the start and end of linear flow for fully coupled model in C1

The left plot in Figure 4.22 shows the log-log plot of pressure difference and derivative versus the radial flow time function. There are also two characteristics that can be used to identify the radial flow period. One is the unit slope of the pressure derivative. The other is the approximate overlying of pressure difference and pressure derivative curves. The radial flow starts at a radial flow time of 0.003, which is about 146.44 days. The right plot shows the log-log plot of pressure versus radial flow time function. For the coupled model, the fracture closure time t_c is 2,516.5 minutes, and the slope m_R in the plot is 25,476.8 psi, then a permeability of 3.74×10^{-19} m^2 can be determined using equation (2.38). Similarly, for the decoupled model, the time to fracture closure is 6,841.7 minutes and the slope in the plot is 8,888.4 psi so that the estimated permeability from the radial flow analysis is 3.95×10^{-19} m^2. Compared to the decoupled model, the poroelastic effects result in a shorter closure time but a larger slope. However, the multiplication of closure time and slope in the coupled model is close to that in the decoupled model, which leads

to a consistent estimate of permeability in both models. In addition, an extrapolation of the pressure curve gives a pressure estimation of 20.0 MPa in both models.

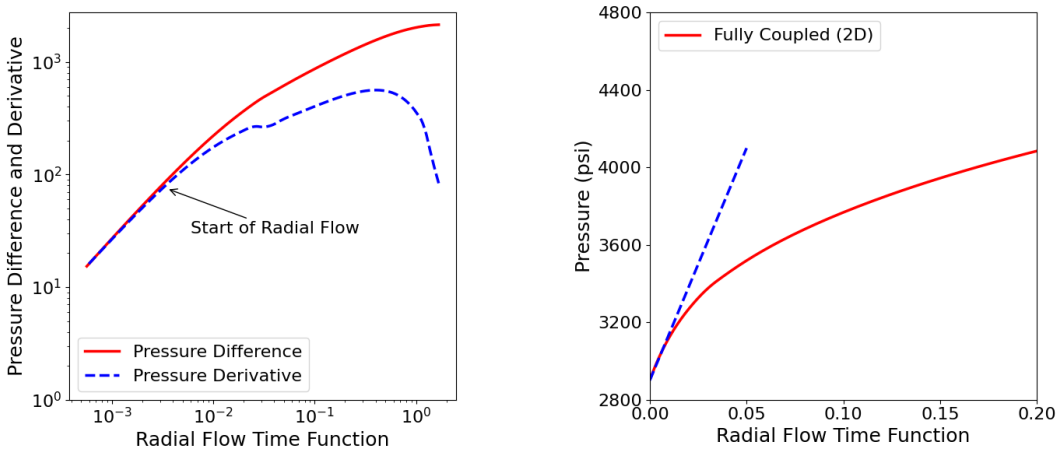

Figure 4.22: Radial flow identification and analysis for fully coupled model in C1

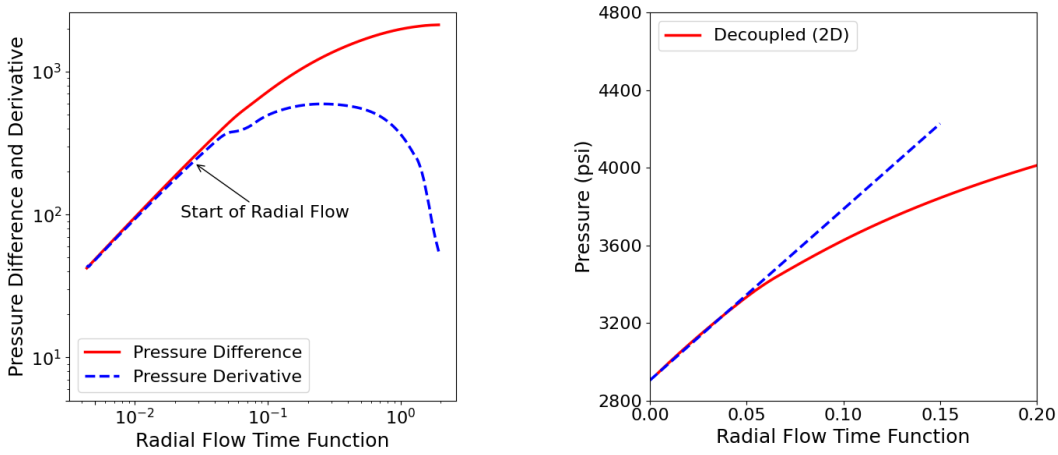

Figure 4.23: Radial flow identification and analysis for decoupled model in C1

Figure 4.24 shows the pressure distribution at the start of radial flow for the fully coupled model in simulation C1. The flow converging to the injection point indicates that the flow regime is radial flow. The pressure at the injection point is about 20.53 MPa, which is close to the initial pore pressure.

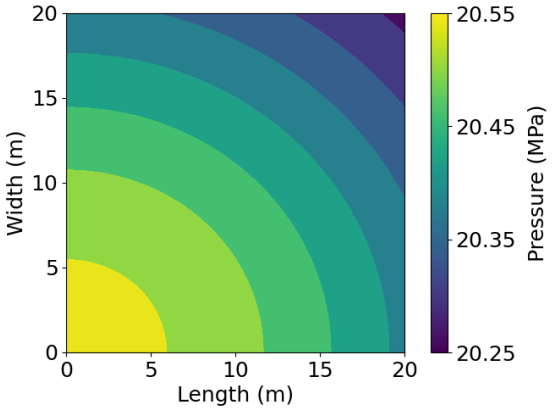

Figure 4.24: Pressure distribution at the start of radial flow for coupled model in C1

4.3.2 ACA for case 2

Poroelastic effects are not significant in simulation C2 due to the high porosity. Both the after-closure linear flow identification and analysis plots are almost identical for the two models. The linear flow starts at a square of linear flow time of 0.7 in both models. A permeability of $3.88 \times 10^{-19}\ \mathrm{m}^2$ and $3.90 \times 10^{-19}\ \mathrm{m}^2$ is inferred for the coupled and decoupled model, respectively. A pressure estimation of 20.13 MPa and 20.17 MPa is determined for the two models by extrapolating the pressure trend. Simulation C2 shows that linear flow analysis can obtain an accurate estimate of permeability and pore pressure when poroelastic effects are ignorable.

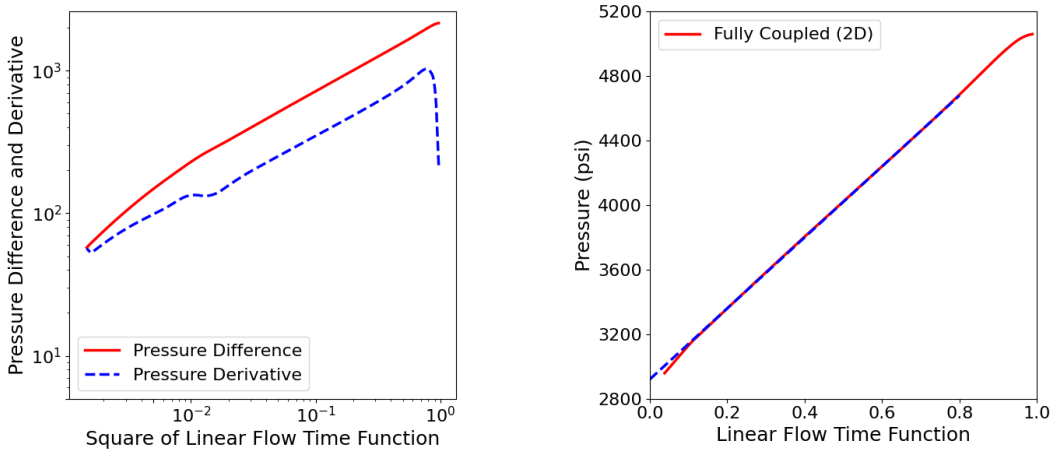

Figure 4.25: Linear flow identification and analysis for fully coupled model in C2

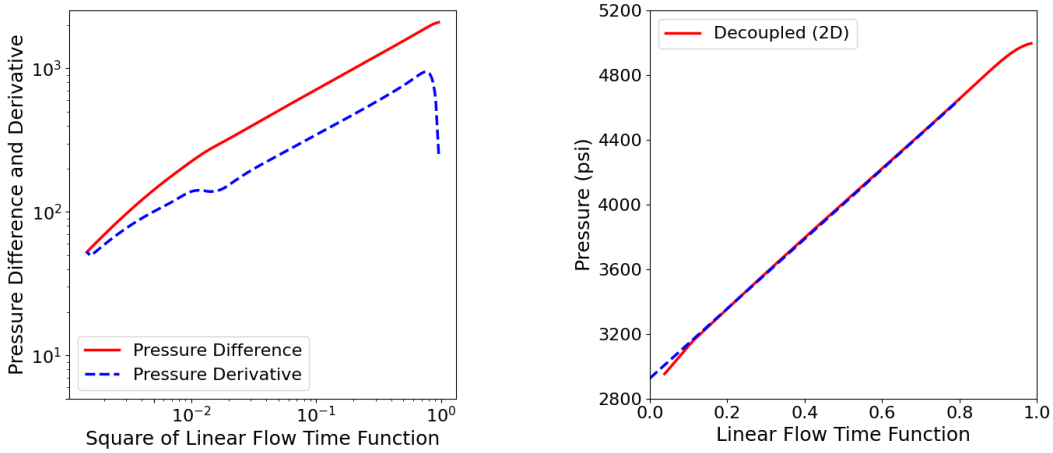

Figure 4.26: Linear flow identification and analysis for decoupled model in C2

Both the after-closure radial flow identification and analysis plots are also close for the two models. The closure time and slope for the coupled model are 1,050.2 minutes and 66,067.2 psi, respectively. For the decoupled model, closure time and slope are 1,157.9 minutes and 58,868.0 psi, respectively. The corresponding permeability estimates are 3.46×10^{-19} m^2 and 3.53×10^{-19} m^2. The initial pore pressure estimates from the radial flow analysis are 20.03 MPa and 20.02 MPa, respectively.

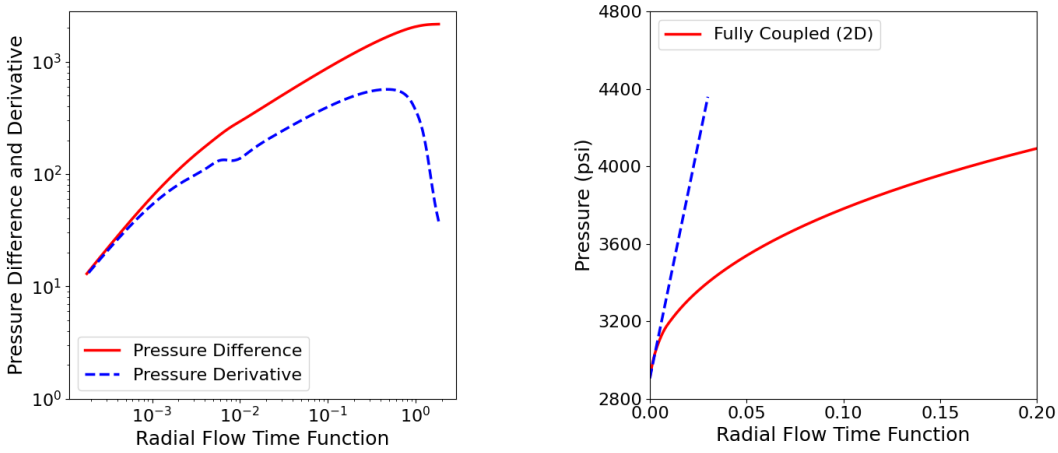

Figure 4.27: Radial flow identification and analysis for fully coupled model in C2

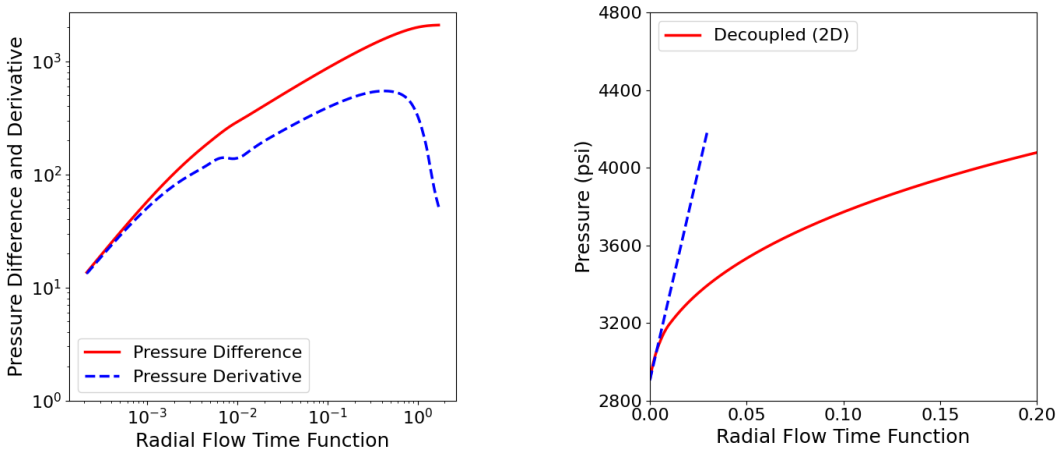

Figure 4.28: Radial flow identification and analysis for decoupled model in C2

4.3.3 ACA for case 3

In Figure 4.29, due to the poroelastic effects, the linear flow analysis in simulation C3 yields a permeability of 1.38×10^{-16} m^2 while the input value is 4×10^{-17} m^2. Pore pressure can still be inferred accurately based on the extrapolation of the pressure curve.

In Figure 4.30, the permeability estimate from the linear flow analysis is 6.34×10^{-17} m^2 and the pore pressure from the linear flow analysis is 19.86 MPa.

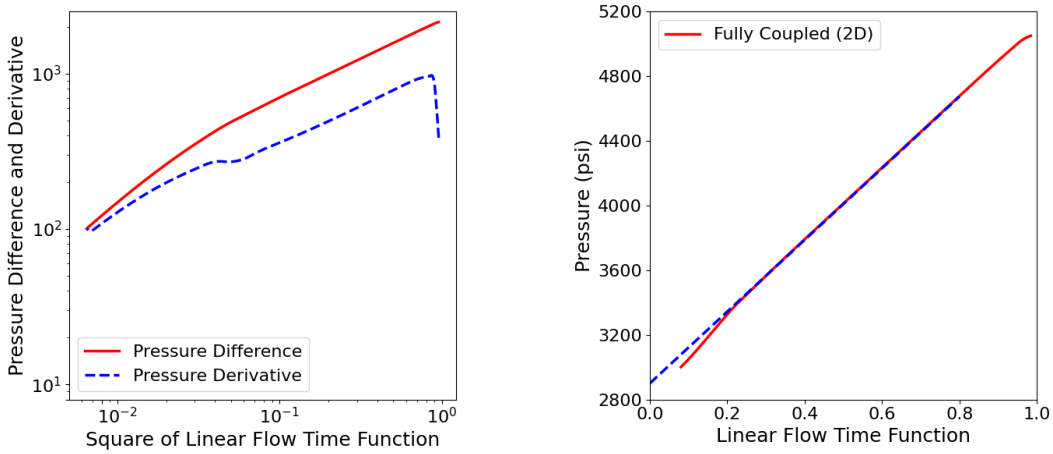

Figure 4.29: Linear flow identification and analysis for fully coupled model in C3

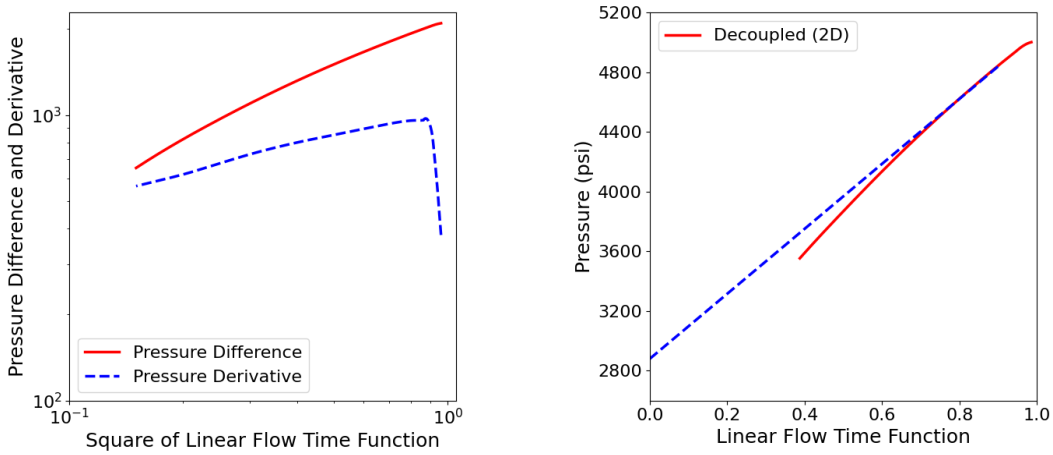

Figure 4.30: Linear flow identification and analysis for decoupled model in C3

With a closure time of 28.2 minutes and a slope of 22,673.0 psi, permeability is determined to be 3.76×10^{-17} m^2 for the coupled the model. For the decoupled model, the closure time is 79.1 minutes and the slope is 7,610.0 psi so that the permeability is 3.99×10^{-17} m^2.

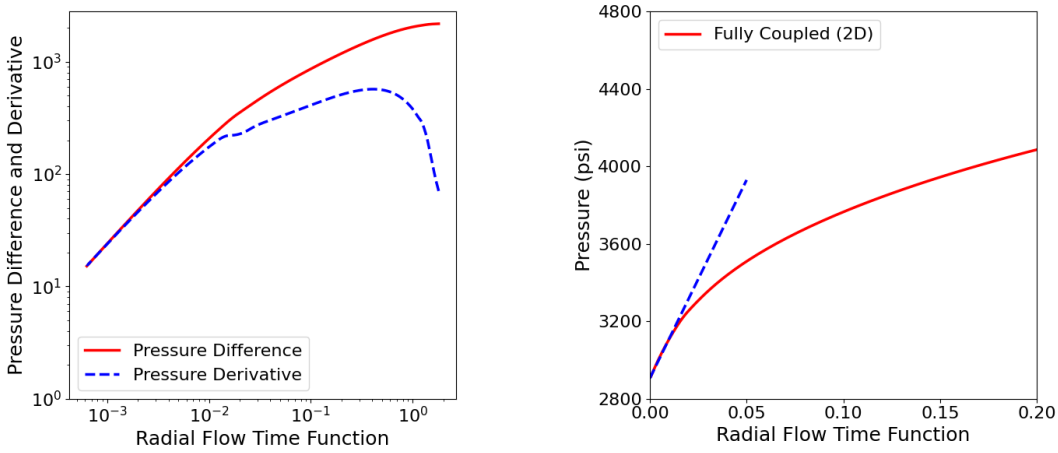

Figure 4.31: Radial flow identification and analysis for fully coupled model in C3

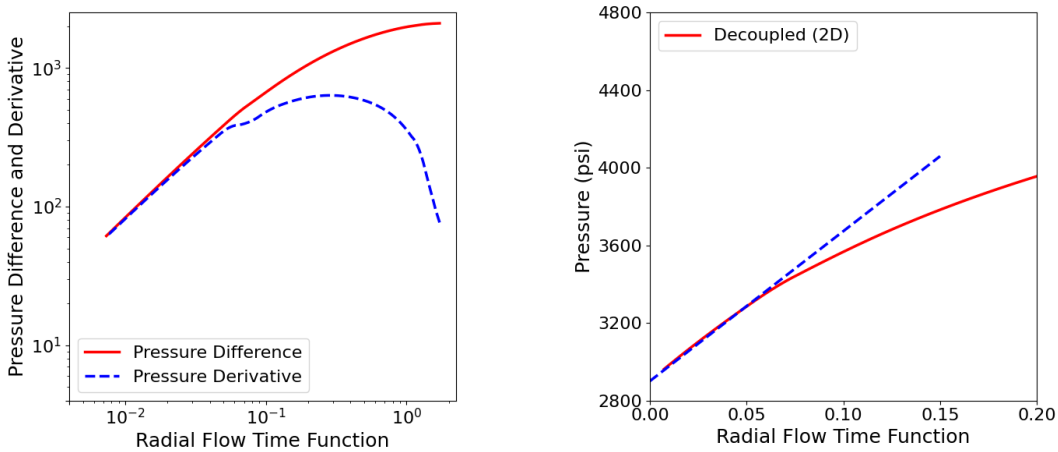

Figure 4.32: Radial flow identification and analysis for decoupled model in C3

4.3.4 ACA for case 4

Because of the larger porosity, poroelastic effects are not apparent in simulation C4 even though the permeability in C4 is larger than that in the base model for two orders of magnitude. The permeability estimates from the linear flow analysis for the two models are 4.50×10^{-17} m^2.and 4.46×10^{-17} m^2, respectively.

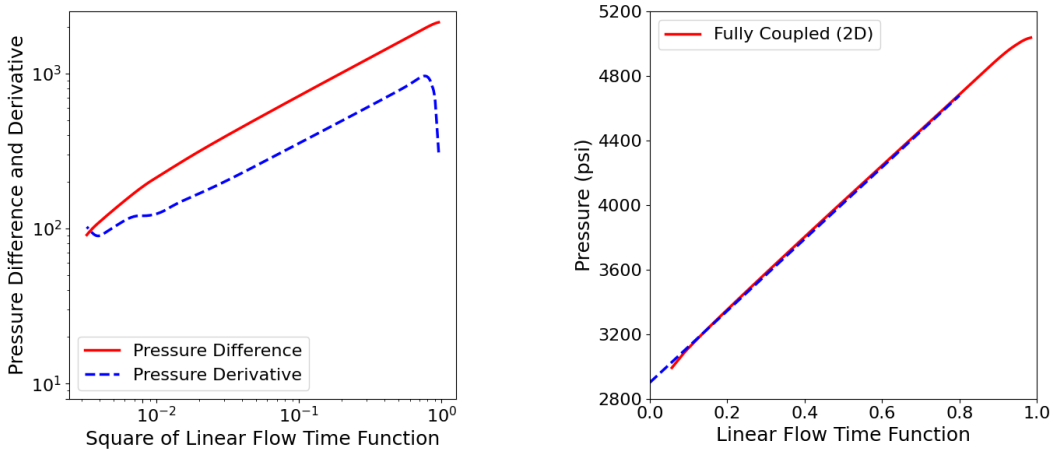

Figure 4.33: Linear flow identification and analysis for fully coupled model in C4

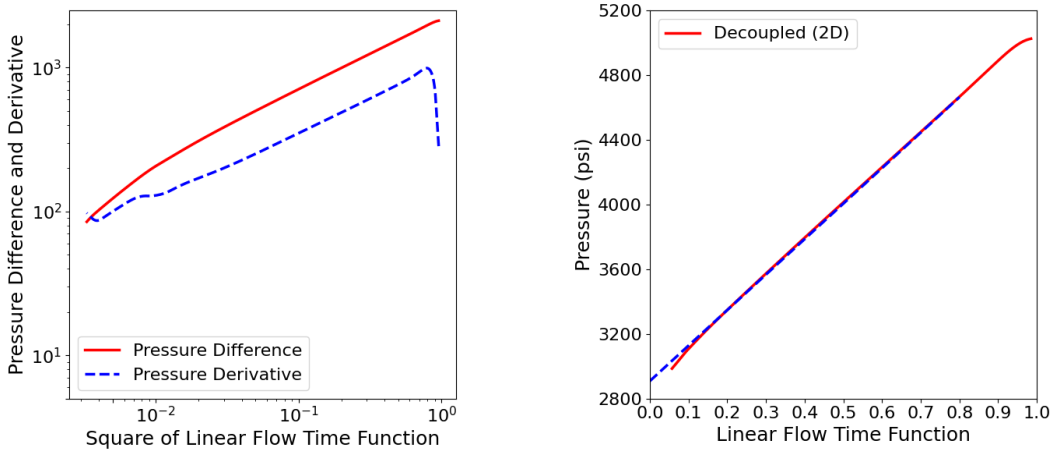

Figure 4.34: Linear flow identification and analysis for decoupled model in C4

Compared with previous cases, the larger porosity and permeability in simulation C4 lead to shorter closure times, which are 13.8 minutes and 15.2 minutes respectively. Radial flow analysis yields a permeability of 3.43×10^{-17} m^2 for the coupled model and a permeability of 3.51×10^{-17} m^2 for the decoupled model.

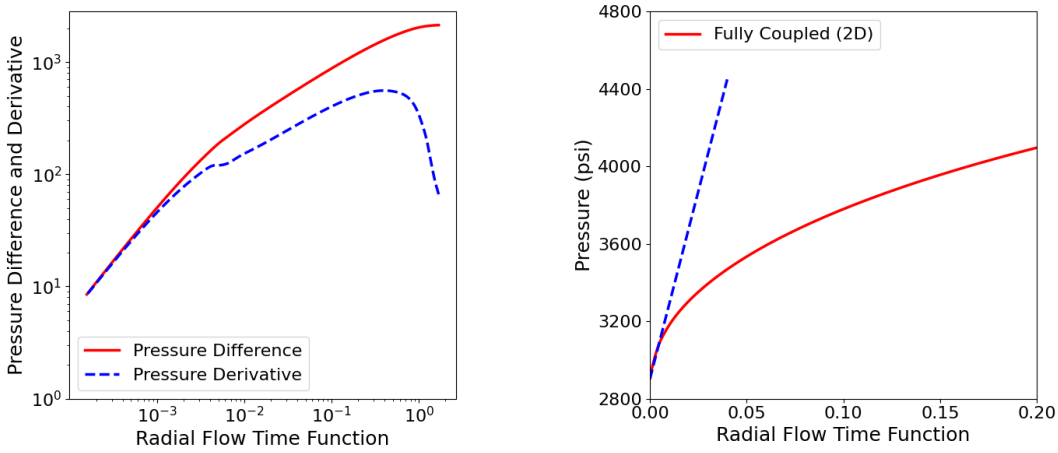

Figure 4.35: Radial flow identification and analysis for fully coupled model in C4

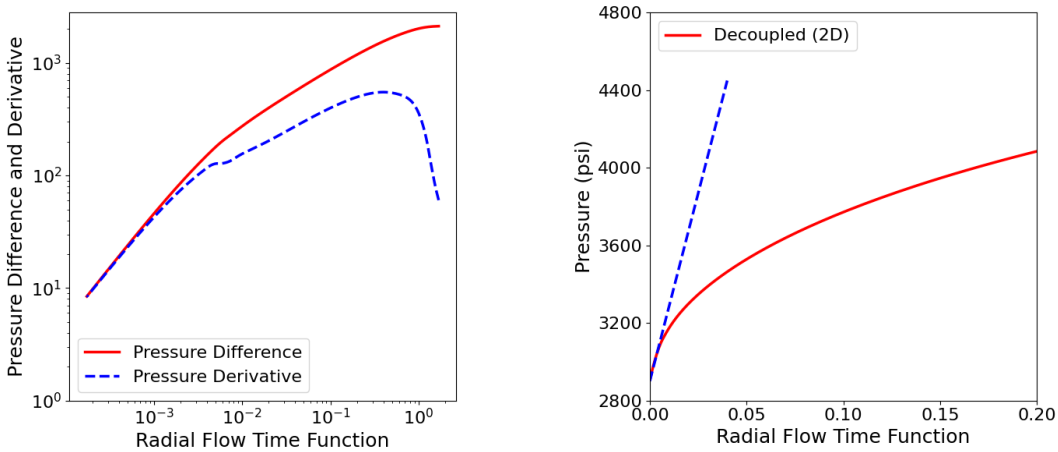

Figure 4.36: Radial flow identification and analysis for decoupled model in C4

4.3.5 ACA for case 5

Poroelastic effects enlarge with the increase of the Biot coefficient. With a leak-off coefficient of 8.21×10^{-7} m/$\sqrt{s}$ inferred from the G-function method, the permeability is determined to be 1.89×10^{-18} m^2 from the linear flow analysis, which is 4.7 times higher

than the input value. In figure 4.38, a permeability of 6.32×10^{-19} m^2 can be obtained from the linear flow analysis.

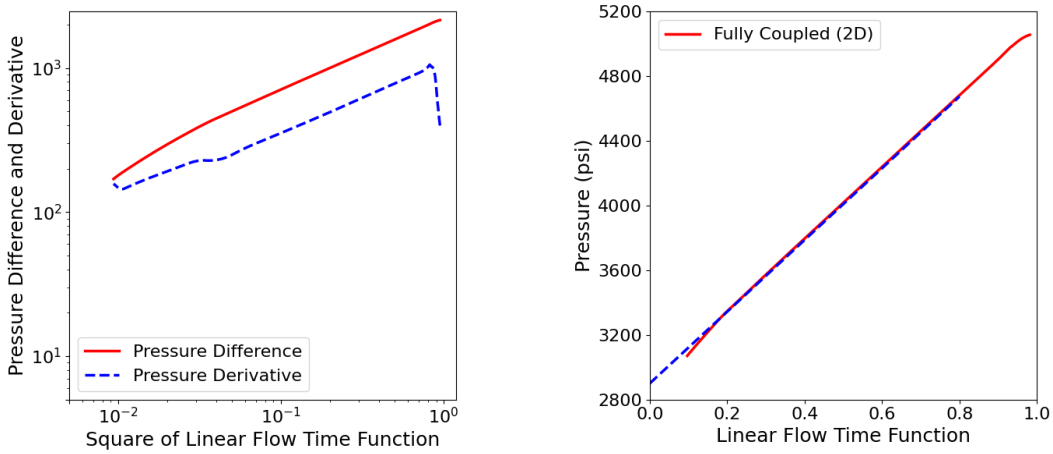

Figure 4.37: Linear flow identification and analysis for fully coupled model in C5

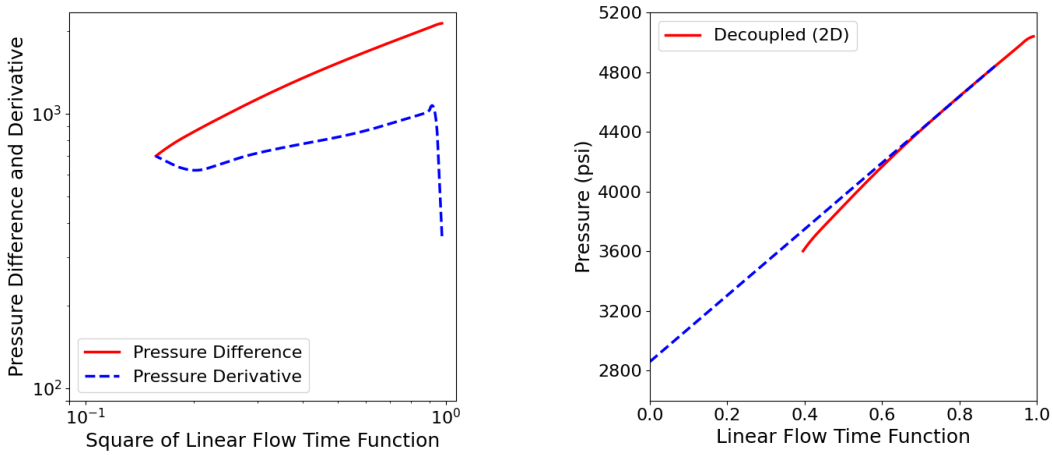

Figure 4.38: Linear flow identification and analysis for decoupled model in C5

For the coupled model, given the closure time of 1901.0 minutes and the slope of 34,931.1 psi, the radial flow analysis gives a permeability estimate of 3.62×10^{-19} m^2. For the decoupled model, the radial flow analysis yields a permeability of 3.76×10^{-19} m^2 with a closure time of 7428.2 minutes and a slope of 8,607.0 psi.

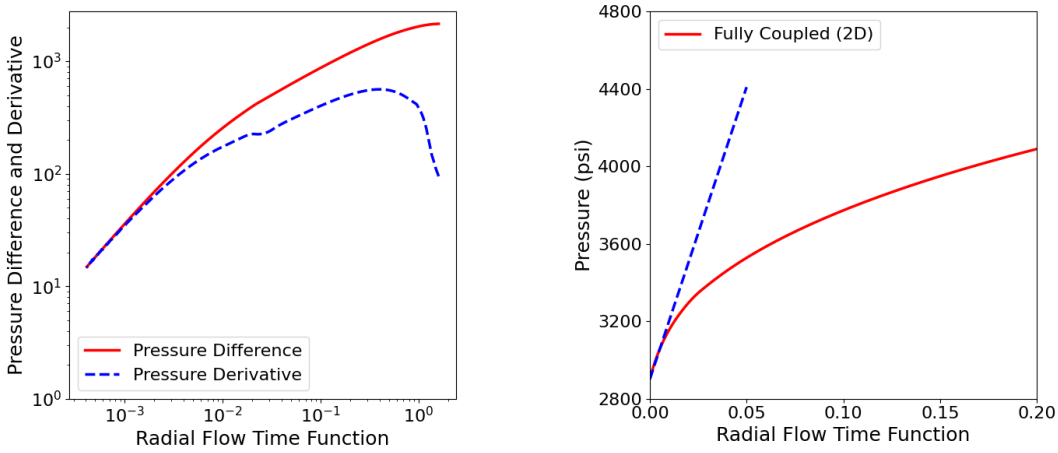

Figure 4.39: Radial flow identification and analysis for fully coupled model in C5

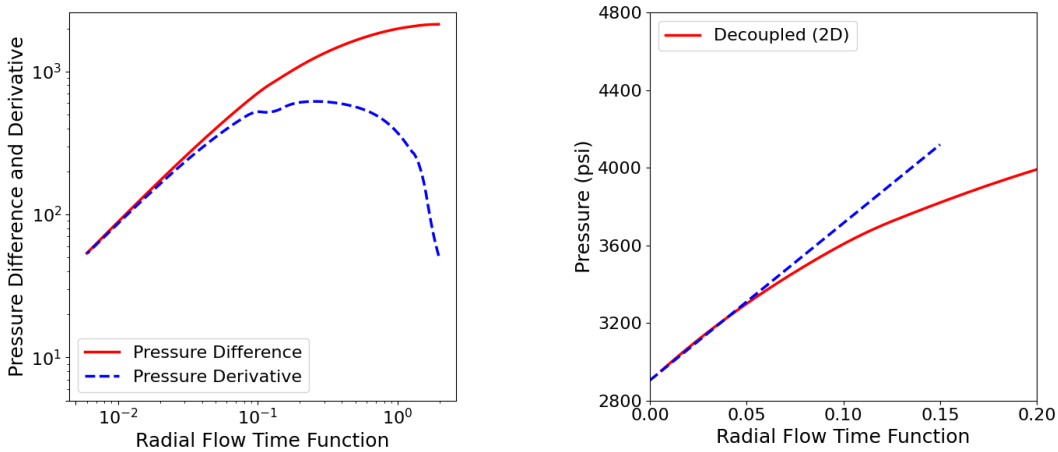

Figure 4.40: Radial flow identification and analysis for decoupled model in C5

4.3.6 ACA for case 6

In Figure 4.41, the permeability is estimated to be 2.14×10^{-18} m^2 and the pore pressure is estimated to be 30.0 MPa. As shown in Figure 4.42, the linear flow regime was not observed in simulation C6 for the decoupled model.

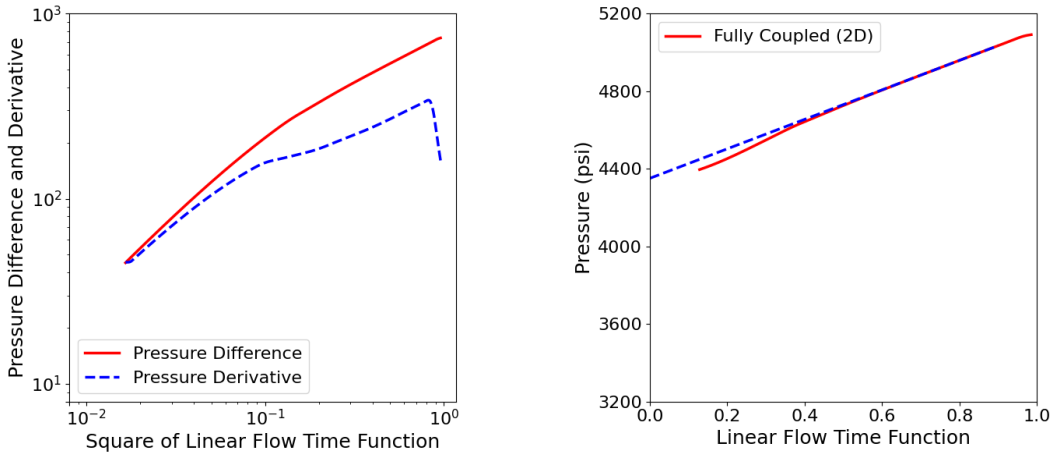

Figure 4.41: Linear flow identification and analysis for fully coupled model in C6

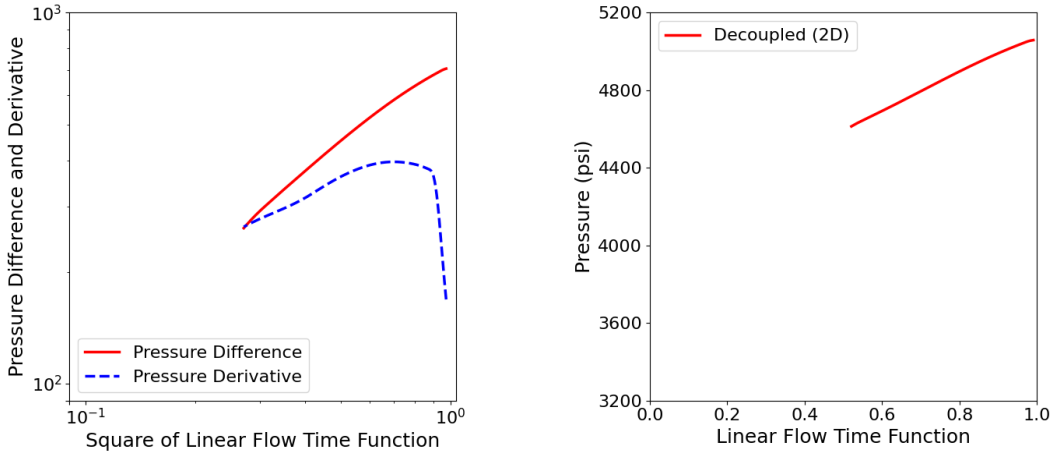

Figure 4.42: Linear flow identification and analysis for decoupled model in C6

A higher initial pore pressure will delay the closure time. The closure time for the coupled model is 14,420.8 minutes and the closure time for the decoupled model is 39,589.4 minutes. The corresponding slopes are 4,342.7 psi and 1,535.4 psi, respectively. The permeability estimates determined from the radial flow analysis are 3.84×10^{-19} m^2 and 3.95×10^{-19} m^2, respectively.

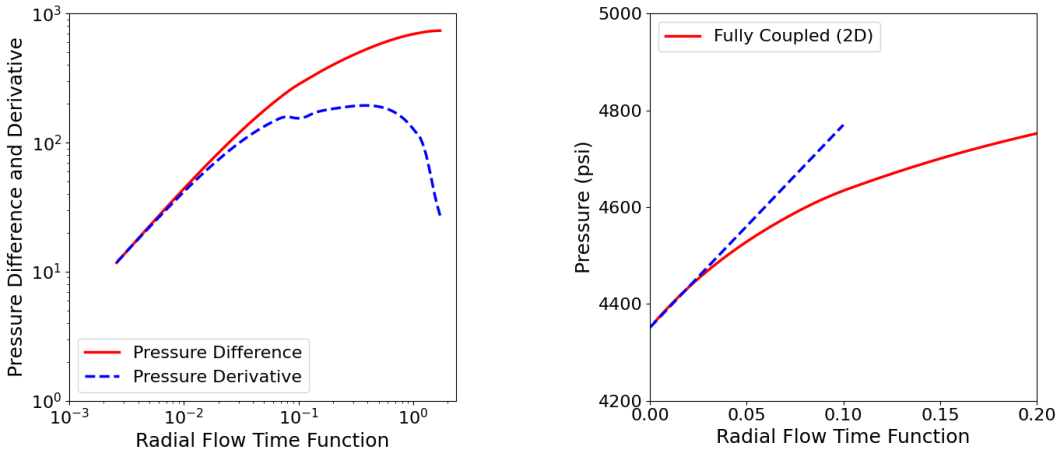

Figure 4.43: Radial flow identification and analysis for fully coupled model in C6

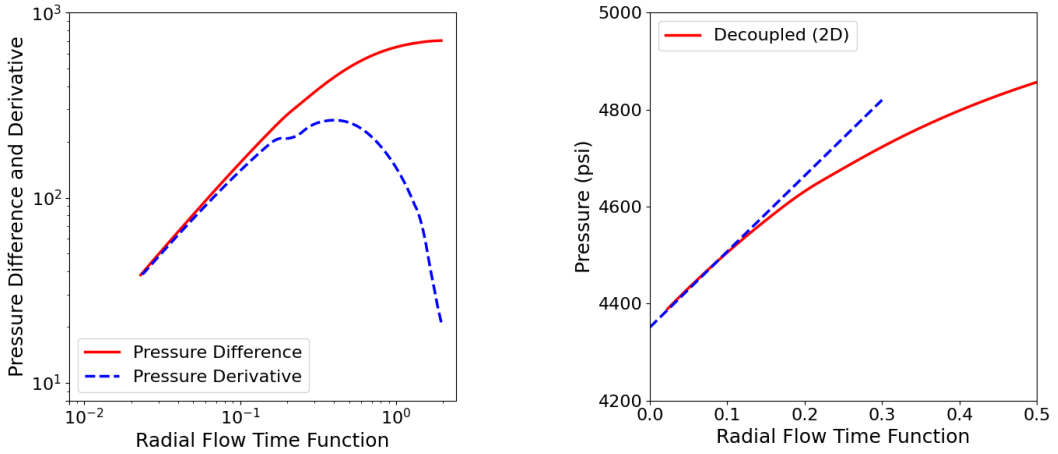

Figure 4.44: Radial flow identification and analysis for decoupled model in C6

Chapter 5

Poroelastic effects on DFIT analysis in the penny-shaped model

5.1 Poroelastic effects on BCA in the penny-shaped model

The poroelastic effects on BCA in the penny-shaped model are presented in this section. The conclusions obtained for the KGD model from the before-closure analysis also work for the penny-shaped model. Case C1 and C2 are performed to demonstrate this point. For the rest four cases, the conclusions drawn from each of them are analogous to those obtained from its corresponding case in the KGD model. The well is injected for 120 seconds with a constant rate of 3×10^{-3} m^3/s.

5.1.1 BCA for case 1

Figure 5.1 shows the G-function plots of simulation C1 for the penny-shaped model. In the left plot, the slope of the line is -0.0343 MPa/G and the shut-in pressure is 37.82 MPa. The leak-off coefficient calculated using the equation in Table 2.2 is 6.64×10^{-7} $\mathrm{m}/\sqrt{\mathrm{s}}$ and the analytical solution is 4.34×10^{-7} $\mathrm{m}/\sqrt{\mathrm{s}}$. The fracture radius is about 10.0 m at

shut-in. In the right plot, the slope of the line is -0.0218 MPa/G and the shut-in pressure is 37.19 MPa. The leak-off coefficient calculated using the equation in table 2.2 is 4.65×10^{-7} m/$\sqrt{s}$ and the analytical solution is 4.19×10^{-7} m/$\sqrt{s}$. In the decoupled model, the facture has a radius of 11.0 m at shut-in.

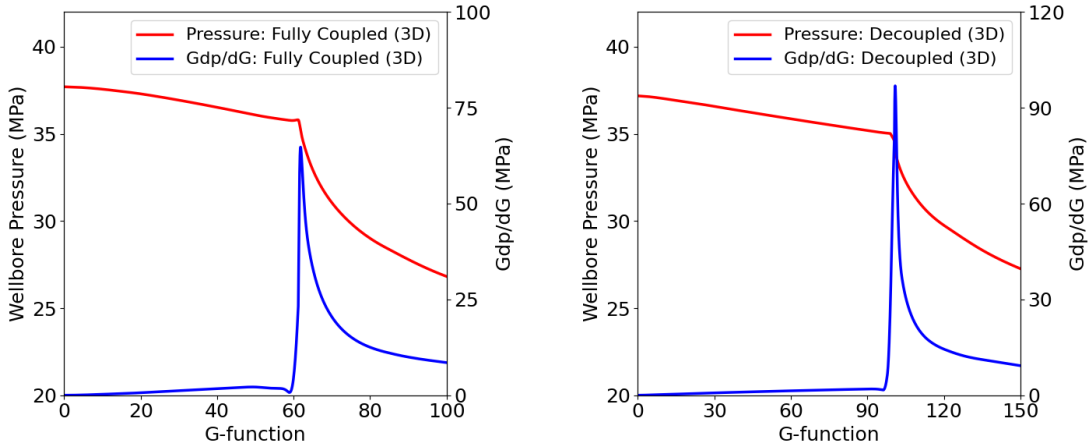

Figure 5.1: G-function plots for fully coupled model and decoupled model in C1

Figure 5.2 shows the fracture openings and pressure profiles at different times after shut-in. Figure 5.2a shows that the fracture is still fully open at the G-time of 35, Figure 5.2b shows that the fracture is partially closed at the G-time of 55, and Figure 5.2c shows that the fracture is fully closed at the G-time of 75. At the G-time of 75, the pressure at the wellbore is about 29.56 MPa, which is below the in-situ stress. The pressure will keep decreasing until it reaches the initial pore pressure, which is equal to 20 MPa in the simulation.

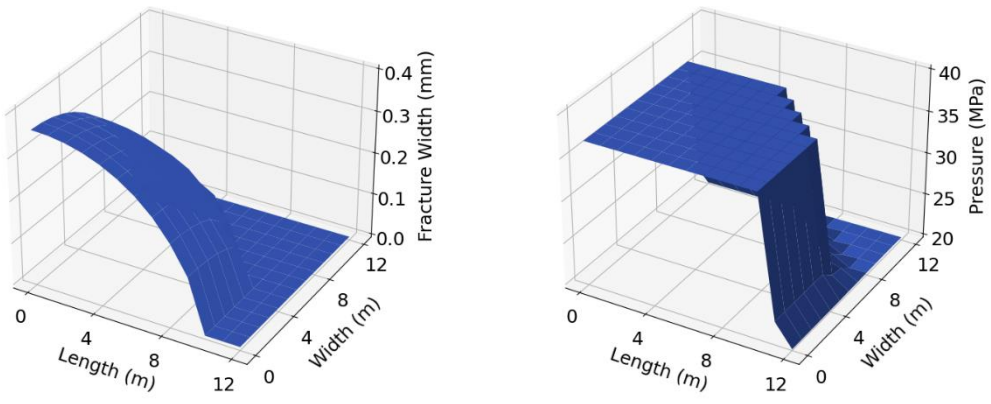

(a)

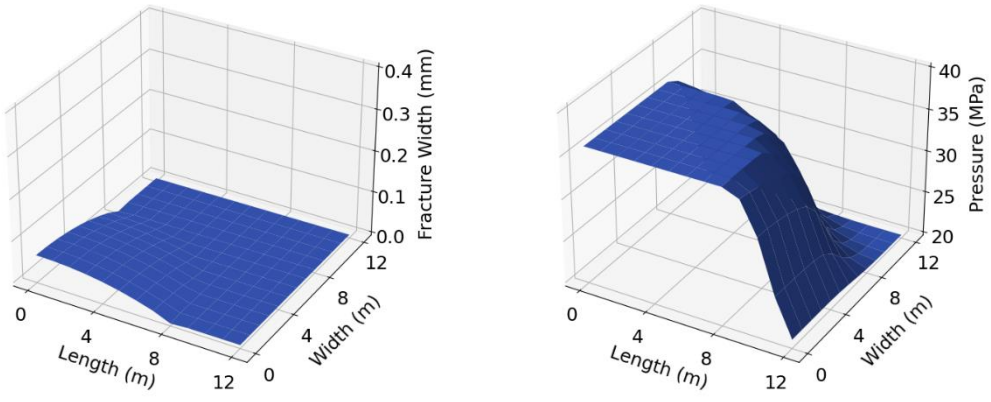

(b)

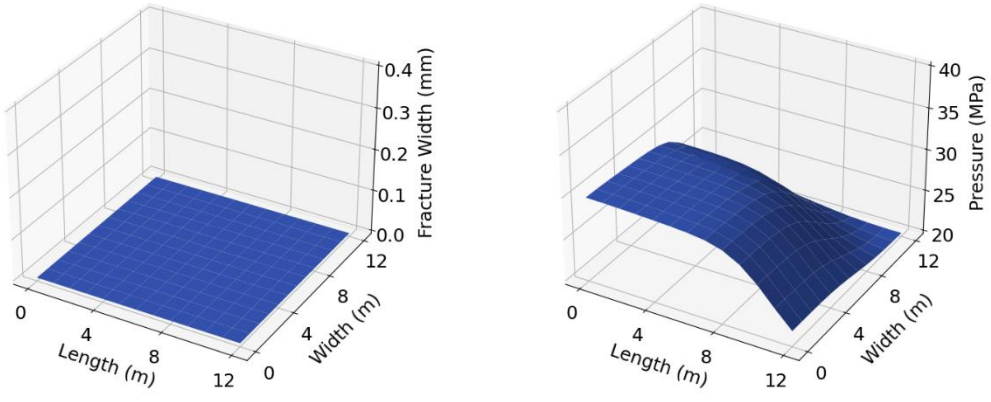

(c)

Figure 5.2: Fracture openings and pressure profiles: (a) G-time = 35; (b) G-time = 55; (c) G-time = 75

Figure 5.3 shows the G-function plot for decoupled model in simulation C1 with a permeability of 4×10^{-19} m^2 in both *x* and *y* direction. As shown in Figure 5.3, the fracture closes at a G-time of 88.3 using the tangent line method. The leak-off coefficient is determined to be 5.28×10^{-7} m$/\sqrt{\text{s}}$ using the equation in Table 2.2. Similar to simulation C1 in the KGD model, the leak-off coefficient is even underestimated in the decoupled model because of the pressure diffusion in both *x* direction and *y* direction.

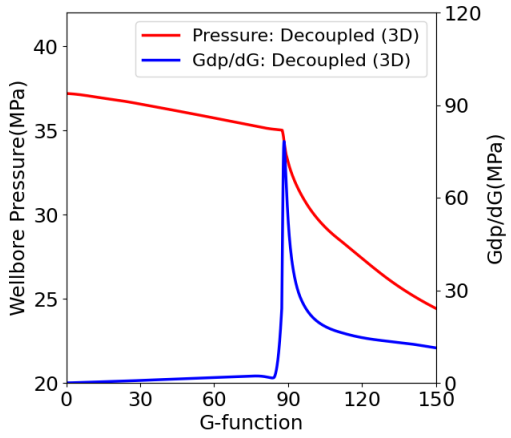

Figure 5.3: G-function plot for decoupled model in case C1 with a permeability of 4×10^{-19} m^2 in both *x* and *y* direction

5.1.2 BCA for case 2

Figure 5.4 shows the G-function plots of simulation C2 in the penny-shaped model. Similar to simulation C2 in the KGD model, poroelastic effects are ignorable in this case. For the coupled model, the leak-off coefficient calculated using slope is 9.05×10^{-7} m$/\sqrt{\text{s}}$, which is close to the one for the decoupled model (8.97×10^{-7} m$/\sqrt{\text{s}}$).

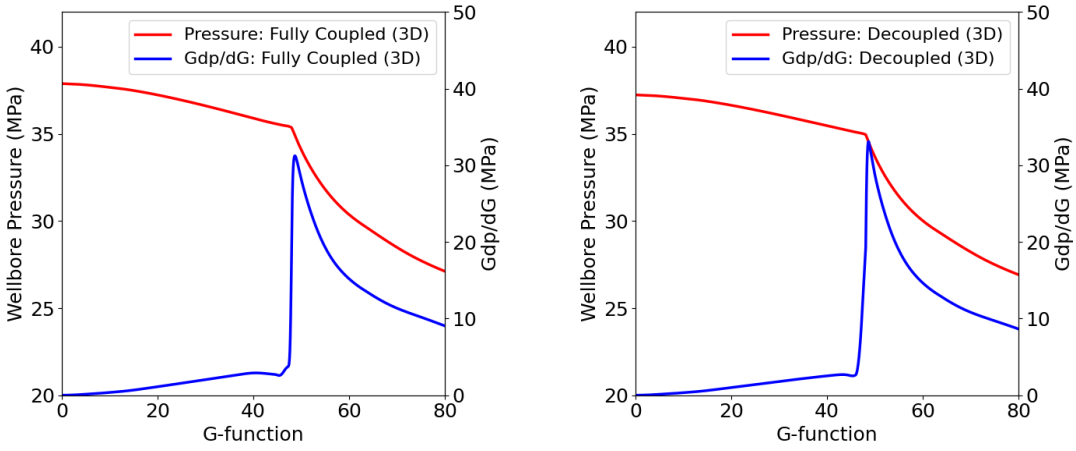

Figure 5.4: G-function plots for fully coupled model and decoupled model in C2

Figure 5.5 shows the G-function plot for decoupled model in simulation C1 with a permeability of 4×10^{-19} m^2 in both *x* and *y* direction. The leak-off coefficient calculated using the slope is 9.16×10^{-7} m$/\sqrt{\text{s}}$. Again, setting permeability to 4×10^{-19} m^2 in both *x* and *y* direction does not have significant effects on estimation of leak-off coefficient when poroelastic effects are ignorable.

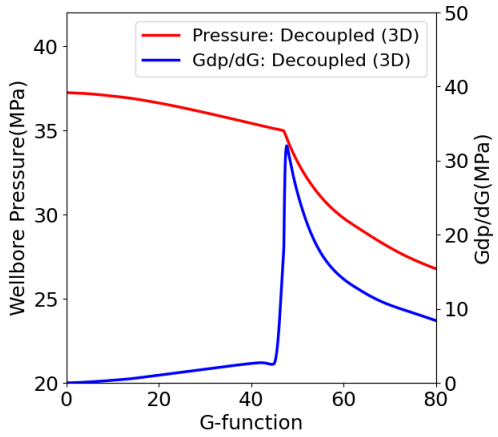

Figure 5.5: G-function plot for decoupled model in case C2 with a permeability of 4×10^{-19} m^2 in both *x* and *y* direction

5.2 Conclusions

By using the fully coupled hydraulic fracturing simulator, the poroelastic effects on DFIT analysis are studied based on the theory of poroelasticity. Conclusions drawn from the analysis are listed below.

1. The poroelastic effects on DFIT analysis cannot be ignored when porosity is relatively small and Biot coefficient is relatively large. During the before-closure analysis, the leak-off coefficient can be twice as large as the one without the consideration of poroelastic effects.

2. Permeability estimated from the linear flow regime can be significantly overestimated, which is mainly due to the underestimated leak-off coefficient obtained from the before-closure analysis. The radial flow analysis can obtain a reliable permeability estimate.

3. Both the linear and radial flow analyses can provide accurate estimates of pore pressure.

4. This study demonstrates that the conclusions obtained for the KGD model from the before-closure analysis are also applicable for the penny-shaped model.

Bibliography

Abe H., Mura T., Keer L., 1976. Growth-rate of a penny-shaped crack in hydraulic fracturing of rocks. *J Geophys Res*. 81(29):5335–40.

Anderson, T. L., 2005. *Fracture Mechanics, Fundamentals and Applications*, 3rd edition, CRC Press.

Bao, J. Q., Fathi E., Ameri S., 2014. A coupled finite element method for the numerical simulation of hydraulic fracturing with a condensation technique. *Engineering Fracture Mechanics*, Volume 131, November 2014, Pages 269-281.

Barree, R. D., Mukherjee H., 1996. Determination of pressure dependent leakoff and its effect on fracture geometry. Paper SPE 36424 presented at the *71st Annual Technical Conference and Exhibition*, Denver, 6-9 October.

Barree, R. D., Barree, V.L., Craig, D., 2009. Holistic fracture diagnostics: consistent interpretation of prefrac injection tests using multiple analysis methods. *SPE Production & Operations*, 24(03), pp.396-406.

Batchelor, G. K., 1967. *An Introduction to Fluid Dynamics*. Cambridge University Press, Cambridge, UK.

Biot M. A., 1941. General theory of three-dimensional consolidation. *Journal of Applied Physics*.

Boshen Li, 2023. Hydraulic Fracturing in Transversely Isotropic Elastic Solids, Ph.D. dissertation.

Bunger, A. P., Detournay, E., Garagash, D. I., 2005. Toughness-dominated hydraulic fracture with leak-off. *Int. J. Fract*., 134(2), 175-190.

Carrier, B., and Granet, S., 2012. Numerical modeling of hydraulic fracture problem in permeable medium using cohesive zone model. *Eng. Fract. Mech*. 79, 312–328.

Carslaw, H., Jaeger, J. C., 1956. *Conduction of Heat in Solids*, 2nd Edition, Oxford University Press, Oxford, U.K.

Cheng, A. H.-D., Detournay, E., 1988. A direct boundary element method for plane strain poroelasticity. *Int. J. Numer. Analy. Meth. Geomech*., 12:551–572.

Cheng, A. H.-D., 2016. *Poroelasticity*, Springer.

Chukwudozie, Chukwudi, 2016. Application of the Variational Fracture Model to Hydraulic Fracturing in Poroelastic Media. LSU Doctoral Dissertations.

Dake, L.P., 1978. *Fundamentals of Reservoir Engineering*, 1st edition, Elsevier.

Detournay, E., 2004. Propagation regimes of fluid-driven fractures in impermeable rocks. *Int. J. Geomech*., 10.1061/(ASCE)1532-3641(2004)4: 1(35), 35–45.

Garagash, D. I., Detournay, E., 2005. Plane-Strain Propagation of a Fluid-Driven Fracture: Small Toughness Solution. *Journal of Applied Mechanics*.

Economides M. J., Nolte K. G., 2000. *Reservoir Stimulation*, 3rd Edition. Chichester, England; New York, John Wiley.

Geertsma J., De Klerk F., 1969. A rapid method of predicting width and extent of hydraulically induced fractures. *J Petrol Technol.* 21(12):1571–81.

Gu, H., Elbel, J. L., Nolte, K. G., Cheng, A. H-D., Abousleiman, Y., 1993. Formation permeability determination using impulse-fracture injection. SPE 25425. Paper presented at the *Production Operations Symposium*, Oklahoma City, OK.

Howard, G., Fast, C. R., 1957. Optimum Fluid Characteristics for Fracture Extension. *Drilling and Production Practice* 24: 261–270. API57-261. New York: American Petroleum Institute.

Mayerhofer, M. J., Economides, M. J., 1993. Permeability estimation from fracture calibration treatments. SPE 26039. Paper presented at the *SPE Western Regional Meeting*, Anchorage, AK.

Mayerhofer, M. J., Ehlig-Economides, C. A., Economides, M. J., 1995. Pressure Transient Analysis of Fracture Calibration Tests. *Journal of Petroleum Technology*. Vol(47)03:229-234.

McClure, M. W., Jung, H., Cramer, D. D., Sharma, M. M., 2016. The Fracture-Compliance Method for Picking Closure Pressure From Diagnostic Fracture-Injection Tests. *SPE Journal* 21 (04).

McClure, M., Bammidi, V., Cipolla, C., Cramer, D., Martin, L., Savitski, A., Sobernheim, D., Voller, K., 2019. A collaborative study on DFIT interpretation: integrating modeling, field data, and analytical techniques. In: Paper Presented at the *SPE/AAPG/SEG Unconventional Resources Technology Conference*, Denver, Colorado, USA.

Monhammadnejad T., Andrade J. E., 2016. Numerical modeling of hydraulic fracture propagation, closure and reopening using XFEM with application to in-situ stress estimation. *Int. J. Numer. Anal. Meth. Geomech*. 40:2033–2060.

Nejati, M., 2015. Finite element modeling of frictional contact and stress intensity factors in three-dimensional fractured media using unstructured tetrahedral meshes. Ph.D. dissertation, Imperial College London.

Nolte, K. G., 1979. Determination of Fracture Parameters from Fracturing Pressure Decline. Paper 8341 presented at the *SPE Annual Technical Conference and Exhibition*, Las Vegas, Nevada, 23-26 September.

Nolte, K. G., 1986. A General Analysis of Fracturing Pressure Decline with Application to Three Models. *SPE Formation Evaluation*. Vol (1) 06:571-583.

Nolte, K. G., Maniere, J. L., Owens, K. A., 1997. After-closure analysis of fracture calibration tests. SPE 386676. Paper presented at the *1997 Annual Technology Conference and Exhibition of the Society of Petroleum Engineers*, San Antonio, TX.

Nolte, K. G., 1997. Background for after-closure analysis of fracture calibration Tests. Unsolicited companion paper to SPE 38676.

Perkins, T. K., Kern, L. R., 1961. Widths of hydraulic fractures. *J. Pet. Technol*. 13 (9), 937–949.

Reddy, J. N., 2019. *An Introduction to the Finite Element Method*, 4th Edition, McGraw-Hill Education.

Rice, J. R., 1968. A path independent integral and the approximate analysis of strain concentration by notches and cracks. *Journal of Applied Mechanics*, 35:379–386.

Salimzadeh S., Khalili, N., 2015. Fully Coupled XFEM Model for Flow and Deformation in Fractured Porous Media with Explicit Fracture Flow. *Int. J. Geomech*, 04015091.

Salimzadeh S., Paluszny, A., Zimmerman R. W., 2016. Three-dimensional poroelastic effects during hydraulic fracturing in permeable rocks. *Int J Solids Struct*, 108:153-163.

Savitski, A.A., Detournay, E., 2002. Propagation of a penny-shaped fluid-driven fracture in an impermeable rock: asymptotic solutions. *International journal of solids and structures*, 39(2002) 6311-6337.

Sneddon, I. N., Elliott, H. A., 1946. The opening of a Griffith crack under internal pressure. *Quarterly of Appl. Math*. 4, no. 262.

Sun, C. T., Jin, Z., 2012. *Fracture Mechanics*, Department of Mechanical Engineering, University of Maine, Zhihe, Academic Press.

Talley, G. R., Swindell, T. M., Waters, G. A., Nolte, K. G., 1999. Field Application of After-Closure Analysis of Fracture Calibration Tests. Paper SPE 52220 presented at the

SPE Mid-Continent Operations Symposium, Oklahoma City, Oklahoma, USA, 28-31 March.

Valko, P. P., Economides M. J., 1999. Fluid-leakoff delineation in high-permeability fracturing. *SPE Production & Facilities* 14 (2).

Verruijt, A., 2016. *Theory and problems of poroelasticity*, http://geo.verruijt.net/. e-book.

Wang, H. F., 2000. *Theory of Linear Poroelasticity with Applications to Geomechanics and Hydrogeology*, Princeton University Press.

Wang, H.Y., Sharma, M. M., 2017. New variable compliance method for estimating in-situ stress and leak-off from DFIT data. SPE 187348. Paper presented at the *SPE Annual Technical Conference and Exhibition*, San Antonio, TX.

Yarushina V. M., Bercovici D., and Oristaglio M. L., 2013. Rock deformation models and fluid leak-off in hydraulic fracturing. *Geophysical Journal International*, Volume 194, Issue 3.

Zanganeh, B., Clarkson, C. R., Hawkes, R. V., 2017. Reinterpretation of Fracture Closure Dynamics During Diagnostic Fracture Injection Tests. Paper SPE 185649 presented at the *SPE Western Regional Meeting*, Bakersfield, California, 23-27 April.

Appendix A

Derivation of the pressure decline equation

The derivation of the pressure decline equation is presented in this section (Economides, 2000). With the assumption of power law fracture growth, the fracture area $\bar{a}$ at a time τ can be related to total fracture area A at the current time t

$$\frac{\tau}{t} = \left(\frac{\bar{a}}{A}\right)^{1/\bar{\alpha}} \tag{A.1}$$

where $\bar{\alpha}$ is the area exponent. In contrast to equation (2.15), the rate of fluid loss per unit area can be expressed in a more general form

$$u_L = \frac{2C_L}{(t-\tau)^{1-\varphi}} \tag{A.2}$$

where φ is the fluid loss exponent. Equation (A.1) can take both Newtonian filtrate and non-Newtonian filtrate into consideration. The leak-off volume per unit area can be obtained through the time integration of equation (A.2)

$$v_L = \int_0^t u_L dt = \frac{2C_L}{\varphi}(t-\tau)^{\varphi} \tag{A.3}$$

Substituting equation (A.1) into equation (A.2), then the rate of fluid loss over an elemental leak-off area $d\bar{a}$ takes the form

$$q_L(d\bar{a}, t) = \frac{2r_p C_L}{t_e^{1-\varphi}} \frac{d\bar{a}}{\left(t_{\bar{\alpha}D} - \bar{\xi}^{1/\bar{\alpha}}\right)^{1-\varphi}} \tag{A.4}$$

where

$$t_{\bar{\alpha}D} = \frac{t}{t_e} \tag{A.5a}$$

$$\bar{\xi} = \frac{\bar{a}}{A_f} \tag{A.5b}$$

where A_f is the fracture surface area at the end of pumping. Integrating over the fracture area can obtain the total rate of fluid loss

$$q_L(A_f, t) = \frac{2r_p C_L A_f}{t_e^{1-\varphi}} f(t_{\bar{\alpha}D}, \bar{\alpha}, \varphi) \tag{A.6}$$

where

$$f(t_{\bar{\alpha}D}, \bar{\alpha}, \varphi) = \int_0^1 \frac{d\bar{\xi}}{\left(t_{\bar{\alpha}D} - \bar{\xi}^{1/\bar{\alpha}}\right)^{1-\varphi}} \tag{A.7}$$

Substituting equation (A.5a) and (A.5b) into equation (A.3) and integrating over the fracture area can obtain the fluid leak-off volume $V_{L,C}$

$$V_{L,C} = 2r_p C_L t_e^{\varphi} A_f g(t_{\bar{\alpha}D}, \bar{\alpha}, \varphi) \tag{A.8}$$

where

$$g(t_{\bar{\alpha}D}, \bar{\alpha}, \varphi) = \frac{1}{\varphi} \int_0^1 \left(t_{\bar{\alpha}D} - \bar{\xi}^{1/\bar{\alpha}}\right)^{\varphi} d\bar{\xi} \tag{A.9}$$

Using the dimensionless time Δt_D, equation (A.7) and (A.9) can be written as

$$f(\Delta t_D, \bar{\alpha}, \varphi) = \int_0^1 \frac{d\bar{\xi}}{\left(1 + \Delta t_D - \bar{\xi}^{1/\bar{\alpha}}\right)^{1-\varphi}} \tag{A.10}$$

$$g(\Delta t_D, \bar{\alpha}, \varphi) = \frac{1}{\varphi} \int_0^1 \left(1 + \Delta t_D - \bar{\xi}^{1/\bar{\alpha}}\right)^{\varphi} d\bar{\xi} \tag{A.11}$$

By substituting the bounding values of $\bar{\alpha}$ (1/2, 1) into equation (A.10) and (A.11) and integrating the resulting expressions. Equation (A.11) will be as same as equation (2.25) and equation (A.10) can be written as (Nolte, 1979)

$$f(\Delta t_D) = \begin{cases} \sin^{-1}(1+\Delta t_D)^{-1/2} & \bar{\alpha} = 1/2 \\ 2\left[(1+\Delta t_D)^{1/2} - \Delta t_D^{1/2}\right] & \bar{\alpha} = 1 \end{cases} \quad (A.12)$$

Based on the material balance, it follows that

$$-\frac{dV_f(\Delta t)}{d\Delta t} = -A_f \frac{d\overline{w}}{d\Delta t} = q_L \quad (A.13)$$

where $\overline{w}$ is the average fracture width. From the liner elastic theory, the net pressure is proportional to $\overline{w}$ in the form of

$$p_{net} = S_f \overline{w} \quad (A.14)$$

Combing equation (A.6) and (A.13) with the differentiation of (A.14) results in

$$-A_f \frac{dp_{net}}{d\Delta t} = \frac{2r_p C_L S_f A_f}{\sqrt{t_e}} f(\Delta t_D) \quad (A.15)$$

Integrating equation (A.15) from $\Delta t_D = 0$ to Δt_D can obtain

$$p_f(\Delta t_D) = ISIP - \frac{\pi r_p C_L S_f \sqrt{t_e}}{2} G(\Delta t_D) \quad (A.16)$$

Appendix B

Finite element formulation for the penny-shaped model

The finite element formulation for the penny-shaped model is presented in this section. From equation (3.12), the finite element model of the equilibrium equation in the *x* direction can be written as

$$(K_{11})^e_{ab}u^e_{1b} + (K_{12})^e_{ab}u^e_{2b} + (K_{13})^e_{ab}u^e_{3b} - (C_{m1})^e_{ab}p^e_b - \left(C_{f1}\right)^e_{ab}p^e_b = (T_1)^e_{ab} \qquad \text{(B. 1)}$$

The coefficient matrices in equation (B. 1) are given by

$$(K_{11})^e_{ab} = \int_\Omega \left[\frac{2G(1-v)}{1-2v}\frac{\partial N^e_a}{\partial x_1}\frac{\partial N^e_b}{\partial x_1} + G\frac{\partial N^e_a}{\partial x_2}\frac{\partial N^e_b}{\partial x_2} + G\frac{\partial N^e_a}{\partial x_3}\frac{\partial N^e_b}{\partial x_3}\right] d\Omega \qquad \text{(B. 2a)}$$

$$(K_{12})^e_{ab} = \int_\Omega \left[\frac{2Gv}{1-2v}\frac{\partial N^e_a}{\partial x_1}\frac{\partial N^e_b}{\partial x_2} + G\frac{\partial N^e_a}{\partial x_2}\frac{\partial N^e_b}{\partial x_1}\right] d\Omega \qquad \text{(B. 2b)}$$

$$(K_{13})^e_{ab} = \int_\Omega \left[\frac{2Gv}{1-2v}\frac{\partial N^e_a}{\partial x_1}\frac{\partial N^e_b}{\partial x_3} + G\frac{\partial N^e_a}{\partial x_3}\frac{\partial N^e_b}{\partial x_1}\right] d\Omega \qquad \text{(B. 2c)}$$

$$(C_{m1})^e_{ab} = \int_\Omega \alpha\frac{\partial N^e_a}{\partial x_1}N^e_b\, d\Omega \qquad \text{(B. 2d)}$$

$$\left(C_{f1}\right)^e_{ab} = \int_{\Gamma_c} N^e_a N^e_b n_1 d\Gamma \qquad \text{(B. 2e)}$$

$$(T_1)^e_{ab} = \int_{\Gamma_t} N^e_a t_1 d\Gamma \qquad \text{(B. 2f)}$$

Similarly, the finite element model of the equilibrium equation in the *y* direction can be written as

$$(K_{21})^e_{ab}u^e_{1b} + (K_{22})^e_{ab}u^e_{2b} + (K_{23})^e_{ab}u^e_{3b} - (C_{m2})^e_{ab}p^e_b - \left(C_{f2}\right)^e_{ab}p^e_b = (T_2)^e_{ab} \quad \text{(B. 3)}$$

The coefficient matrices in equation (B. 3) are given by

$$(K_{21})^e_{ab} = \int_\Omega \left[\frac{2Gv}{1-2v}\frac{\partial N^e_a}{\partial x_2}\frac{\partial N^e_b}{\partial x_1} + G\frac{\partial N^e_a}{\partial x_1}\frac{\partial N^e_b}{\partial x_2}\right] d\Omega \quad \text{(B. 4a)}$$

$$(K_{22})^e_{ab} = \int_\Omega \left[G\frac{\partial N^e_a}{\partial x_1}\frac{\partial N^e_b}{\partial x_1} + \frac{2G(1-v)}{1-2v}\frac{\partial N^e_a}{\partial x_2}\frac{\partial N^e_b}{\partial x_2} + G\frac{\partial N^e_a}{\partial x_3}\frac{\partial N^e_b}{\partial x_3}\right] d\Omega \quad \text{(B. 4b)}$$

$$(K_{23})^e_{ab} = \int_\Omega \left[\frac{2Gv}{1-2v}\frac{\partial N^e_a}{\partial x_2}\frac{\partial N^e_b}{\partial x_3} + G\frac{\partial N^e_a}{\partial x_3}\frac{\partial N^e_b}{\partial x_2}\right] d\Omega \quad \text{(B. 4c)}$$

$$(C_{m2})^e_{ab} = \int_\Omega \alpha\frac{\partial N^e_a}{\partial x_2}N^e_b\, d\Omega \quad \text{(B. 4d)}$$

$$\left(C_{f2}\right)^e_{ab} = \int_{\Gamma_c} N^e_a N^e_b n_2 d\Gamma \quad \text{(B. 4e)}$$

$$(T_2)^e_{ab} = \int_{\Gamma_t} N^e_a t_2 d\Gamma \quad \text{(B. 4f)}$$

The finite element model of the equilibrium equation in the *z* direction can be written as

$$(K_{31})^e_{ab}u^e_{1b} + (K_{32})^e_{ab}u^e_{2b} + (K_{33})^e_{ab}u^e_{3b} - (C_{m3})^e_{ab}p^e_b - \left(C_{f3}\right)^e_{ab}p^e_b = (T_3)^e_{ab} \quad \text{(B. 5)}$$

The coefficient matrices in equation (B. 5) are given by

$$(K_{31})^e_{ab} = \int_\Omega \left[\frac{2Gv}{1-2v}\frac{\partial N^e_a}{\partial x_3}\frac{\partial N^e_b}{\partial x_1} + G\frac{\partial N^e_a}{\partial x_1}\frac{\partial N^e_b}{\partial x_3}\right] d\Omega \quad \text{(B. 6a)}$$

$$(K_{32})^e_{ab} = \int_\Omega \left[\frac{2Gv}{1-2v}\frac{\partial N^e_a}{\partial x_3}\frac{\partial N^e_b}{\partial x_2} + G\frac{\partial N^e_a}{\partial x_2}\frac{\partial N^e_b}{\partial x_3}\right] d\Omega \quad \text{(B. 6b)}$$

$$(K_{33})^e_{ab} = \int_\Omega \left[G\frac{\partial N^e_a}{\partial x_1}\frac{\partial N^e_b}{\partial x_1} + G\frac{\partial N^e_a}{\partial x_2}\frac{\partial N^e_b}{\partial x_2} + \frac{2G(1-v)}{1-2v}\frac{\partial N^e_a}{\partial x_3}\frac{\partial N^e_b}{\partial x_3}\right] d\Omega \quad \text{(B. 6c)}$$

$$(C_{m3})^e_{ab} = \int_\Omega \alpha \frac{\partial N^e_a}{\partial x_3} N^e_b \, d\Omega \tag{B.6d}$$

$$\left(C_{f3}\right)^e_{ab} = \int_{\Gamma_c} N^e_a N^e_b n_3 d\Gamma \tag{B.6e}$$

$$(T_3)^e_{ab} = \int_{\Gamma_t} N^e_a t_3 d\Gamma \tag{B.6f}$$

From equation (3.19), the finite element model of the storage equation can be written as

$$(C^T_{m1})^e_{ab} \frac{\partial}{\partial t}(u^e_{1b}) + (C^T_{m2})^e_{ab} \frac{\partial}{\partial t}(u^e_{2b}) + (C^T_{m3})^e_{ab} \frac{\partial}{\partial t}(u^e_{2b}) + (M_m)^e_{ab} \frac{\partial}{\partial t}(p^e_b)$$

$$+(H_m)^e_{ab} p^e_b - (L)^e_{ab} p^e_b = 0 \tag{B.7}$$

where

$$(C^T_{m1})^e_{ab} = \alpha \int_\Omega N^e_a \frac{\partial N^e_b}{\partial x_1} d\Omega \tag{B.8a}$$

$$(C^T_{m2})^e_{ab} = \alpha \int_\Omega N^e_a \frac{\partial N^e_b}{\partial x_2} d\Omega \tag{B.8b}$$

$$(C^T_{m3})^e_{ab} = \alpha \int_\Omega N^e_a \frac{\partial N^e_b}{\partial x_3} d\Omega \tag{B.8c}$$

$$(M_m)^e_{ab} = S \int_\Omega N^e_a \, N^e_b \; d\Omega \tag{B.8d}$$

$$(H_m)^e_{ab} = \frac{k}{\mu} \int_\Omega \left[\frac{\partial N^e_a}{\partial x_1} \frac{\partial N^e_b}{\partial x_1} + \frac{\partial N^e_a}{\partial x_2} \frac{\partial N^e_b}{\partial x_2} + \frac{\partial N^e_a}{\partial x_3} \frac{\partial N^e_b}{\partial x_3} \right] d\Omega \tag{B.8e}$$

$$(L)^e_{ab} = \frac{k}{\mu} \int_\Gamma \left[N^e_a \frac{\partial N^e_b}{\partial x_1} n_1 + N^e_a \frac{\partial N^e_b}{\partial x_2} n_2 + N^e_a \frac{\partial N^e_b}{\partial x_3} n_3 \right] d\Gamma \tag{B.8f}$$

For the fracture flow equation, the finite element model can be written as

$$\left(C_{f1}^{T}\right)_{ab}^{e}\frac{\partial}{\partial t}(u_{1b}^{e})+\left(C_{f2}^{T}\right)_{ab}^{e}\frac{\partial}{\partial t}(u_{2b}^{e})+\left(C_{f3}^{T}\right)_{ab}^{e}\frac{\partial}{\partial t}(u_{3b}^{e})+\left(H_{f}\right)_{ab}^{e}p_{b}^{e}-(L)_{ab}^{e}p_{b}^{e}=Q^{e} \tag{B.9}$$

where

$$\left(C_{f1}^{T}\right)_{ab}^{e}=\int_{\Gamma}N_{a}^{e}\,N_{b}^{e}n_{1}d\Gamma \tag{B.10a}$$

$$\left(C_{f2}^{T}\right)_{ab}^{e}=\int_{\Gamma}N_{a}^{e}\,N_{b}^{e}n_{2}d\Gamma \tag{B.10b}$$

$$\left(C_{f3}^{T}\right)_{ab}^{e}=\int_{\Gamma}N_{a}^{e}\,N_{b}^{e}n_{3}d\Gamma \tag{B.10c}$$

$$\left(H_{f}\right)_{ab}^{e}=\frac{w^{3}}{12\mu}\int_{\Gamma}\left[\frac{\partial N_{a}^{e}}{\partial x_{1}}\frac{\partial N_{b}^{e}}{\partial x_{1}}+\frac{\partial N_{a}^{e}}{\partial x_{2}}\frac{\partial N_{b}^{e}}{\partial x_{2}}\right]d\Gamma \tag{B.10d}$$

$$(L)_{ab}^{e}=\frac{k}{\mu}\int_{\Gamma}\left[N_{a}^{e}\frac{\partial N_{b}^{e}}{\partial x_{1}}n_{1}+N_{a}^{e}\frac{\partial N_{b}^{e}}{\partial x_{2}}n_{2}+N_{a}^{e}\frac{\partial N_{b}^{e}}{\partial x_{3}}n_{3}\right]d\Gamma \tag{B.10e}$$

Equation (B.1), (B.3), (B.5), (B.7), and (B.9) can be written in the matrix form below, both the superscript and the subscript are omitted for simplicity.

$$\begin{bmatrix}[0] & [0] & [0] & [0]\\ [0] & [0] & [0] & [0]\\ [0] & [0] & [0] & [0]\\ C_{m1}^{T}+C_{f1}^{T} & C_{m2}^{T}+C_{f2}^{T} & C_{m3}^{T}+C_{f3}^{T} & M_{m}\end{bmatrix}\frac{\partial}{\partial t}\begin{bmatrix}u_{1}\\ u_{2}\\ u_{3}\\ p\end{bmatrix}$$

$$+\begin{bmatrix}K_{11} & K_{12} & K_{13} & -C_{m1}-C_{f1}\\ K_{21} & K_{22} & K_{23} & -C_{m2}-C_{f2}\\ K_{31} & K_{32} & K_{33} & -C_{m3}^{T}-C_{f3}^{T}\\ [0] & [0] & [0] & H_{m}+H_{f}-L\end{bmatrix}\begin{bmatrix}u_{1}\\ u_{2}\\ u_{3}\\ p\end{bmatrix}=\begin{bmatrix}T_{1}\\ T_{2}\\ T_{3}\\ Q\end{bmatrix} \tag{B.11}$$

By using the finite difference method for the time discretization, the global matrix for the three-dimensional model can be written as

$$\begin{bmatrix} K_{11} & K_{12} & K_{13} & -C_{m1} - C_{f1} \\ K_{21} & K_{22} & K_{23} & -C_{m2} - C_{f2} \\ K_{31} & K_{32} & K_{33} & -C_{m3}^T - C_{f3}^T \\ C_{m1}^T + C_{f1}^T & C_{m2}^T + C_{f2}^T & C_{m3}^T + C_{f3}^T & M_m + \left(H_m + H_f - L\right)\Delta t \end{bmatrix} \begin{bmatrix} u_1^s \\ u_2^s \\ u_3^s \\ p^s \end{bmatrix}$$

$$= \begin{bmatrix} [0] & [0] & [0] & [0] \\ [0] & [0] & [0] & [0] \\ [0] & [0] & [0] & [0] \\ C_{m1}^T + C_{f1}^T & C_{m2}^T + C_{f2}^T & C_{m3}^T + C_{f3}^T & M_m \end{bmatrix} \begin{bmatrix} u_1^{s-1} \\ u_2^{s-1} \\ u_3^{s-1} \\ p^{s-1} \end{bmatrix} + \begin{bmatrix} T_1 \\ T_2 \\ T_3 \\ Q\Delta t_s \end{bmatrix} \quad \text{(B. 12)}$$